PHYSICAL PROPERTIES AND MULTI-SCALE SEISMIC ANISOTROPY IN THE CRUST SURROUNDING THE SAN ANDREAS FAULT NEAR PARKFIELD, CA.

A DISSERTATION
SUBMITTED TO THE DEPARTMENT OF GEOPHYSICS
AND THE COMMITTEE ON GRADUATE STUDIES
OF STANFORD UNIVERSITY
IN PARTIAL FULFILLMENT OF THE REQUIREMENTS
FOR THE DEGREE OF
DOCTOR OF PHILOSOPHY

Naomi L. Boness

December 2005

© Copyright by Naomi L. Boness 2006
All Rights Reserved

I certify that I have read this dissertation and that in my opinion it is fully adequate, in scope and quality, as a dissertation for the degree of Doctor of Philosophy.

_____
Mark D. Zoback (Principal Adviser)

I certify that I have read this dissertation and that in my opinion it is fully adequate, in scope and quality, as a dissertation for the degree of Doctor of Philosophy.

_____
Norman H. Sleep

I certify that I have read this dissertation and that in my opinion it is fully adequate, in scope and quality, as a dissertation for the degree of Doctor of Philosophy.

_____
Gregory C. Beroza

I certify that I have read this dissertation and that in my opinion it is fully adequate, in scope and quality, as a dissertation for the degree of Doctor of Philosophy.

_____
Stephen H. Hickman

Approved for the University Committee on Graduate Studies.

Abstract

In this thesis I present my contribution to understanding the physical nature of the crust in and near the San Andreas Fault by studying the physical processes controlling shear velocity anisotropy at a variety of scales. The region surrounding the San Andreas Fault Observatory at Depth (SAFOD) near Parkfield, CA is an ideal location to study the effect of crustal structure and the state of stress on seismic velocity anisotropy because the direction of maximum horizontal compression, S_{Hmax}, is at a high angle to the predominantly northwest-southeast structural trend, making it relatively easy to distinguish the effects of both mechanisms. I utilize a variety of data sets including a suite of geophysical logs from the SAFOD boreholes, earthquake data recorded on the SAFOD pilot hole array and regional seismic data from the Northern California Seismic Network (NCSN) and the Southern California Seismic Network (SCSN).

To investigate shear velocity anisotropy at the scale of the brittle crust (~15km), I study crustal earthquakes occurring beneath high quality three-component seismic stations throughout western California. Seismic stations located away from major faults exhibit fast shear polarizations aligned with S_{Hmax}. In contrast, seismic stations located along major faults show that the structural fabric of the fault zone controls velocity anisotropy. With knowledge of the seismic wavelengths, I deduce there is a zone ~200-500 m wide of anomalous physical properties.

At a more local scale (~3 km), dipole sonic logs in the SAFOD boreholes located 1.8 km to the southwest of the SAF, indicate stress-induced shear velocity anisotropy in granitic rocks and unbedded sandstones. In bedded shales, structurally-controlled anisotropy is dominant. To substantiate this interpretation, I developed a theoretical

model of structural anisotropy that may be applied to an arbitrarily oriented borehole in a transversely isotropic formation.

At the finest scale investigated in this thesis (< 1 km) petrophysical data acquired in SAFOD indicates the deformation is concentrated in a clay-rich fault core about 20 m wide with unique physical properties, embedded within a ~250 m wide damage zone. Stress-induced anisotropy indicates that S_{Hmax} rotates from being approximately fault-normal to approximately north-south within the fault core as predicted by the model of Rice [1992] for a weak fault in a strong crust.

At all scales, the orientation of the regional maximum horizontal compressive stress is inferred to be at a high angle to the active fault trace. I conclude that the evidence presented in this thesis supports the hypothesis that the San Andreas Fault is a zone of unique physical properties, slipping at low levels of resolved shear stress.

Acknowledgements

First and foremost, I would like to acknowledge my Ph.D. advisor, Prof. Mark Zoback, for being such a wonderful mentor. Thank you so much, Mark, for giving me so many opportunities and providing such a great working environment. I thank you for sharing your extensive knowledge and scientific insights with me and our many thought-provoking discussions. Your enthusiasm and continual support has made the last five years so much fun!

I am also grateful to the members of my committee, Prof. Norman Sleep, Prof. Gregory Beroza and Dr. Stephen Hickman for their continued interest in my work and the many comments and suggestions that helped focus my research.

SAFOD has been such a big part of my life during my time at Stanford and my acknowledgements would not be complete without thanking all the people who I have had the pleasure of working with on this project. I would like to say a joint thank you to the principle investigators, Mark Zoback, Steve Hickman and Bill Ellsworth, for giving me the opportunity to participate in SAFOD at such a high level, which has not only been an incredible science endeavor but also a life experience. At the drill site I was fortunate enough to interact with a number of extremely knowledgeable people who taught me so much about drilling. My thanks to Louie Capuano, Jim Hansen, Lothar Wohlgemuth, Jerry Hamblin, Randy Abshire, Thomas Wiersberg, all the drilling crews and the many other scientists I had the pleasure of working with on the SAFOD project. I am also so grateful to the many students who came down to the drill site and dedicated their time and energy to help me collect data and wash cuttings.

I feel really proud to have been a member of the Stress and Crustal Mechanics research group at Stanford and had the opportunity to work with so many talented people, many of whom have become friends over the years. I would especially like to acknowledge the following people for their support, friendship and camaraderie: Lourdes Colmenares, Ellen Mallman, Stephanie Prejean, Paul Hagin, Alvin Chan, John Townend, Hannah Miller, Amie Lucier, Amy Day-Lewis, Laura Chiaramonte and Pijush Paul. Our research group is lucky to be associated with Prof. George Thompson, who I thank for taking such an active interest in my work and always having time to discuss science and give me advice on my career path.

My friends and colleagues at Stanford have made this such a wonderful place to be and there are three people in particular who deserve a special mention. During my first week at Stanford I was fortunate enough to meet Carrie, Justin and Kamini who have been such wonderful friends over the last five years. Carrie, I cannot imagine having a more thoughtful, supportive and fun friend. Thank you for always being there and for sharing with me all the adventures that we dreamed up over coffee. Justin, I thank you for sharing ideas, suffering through innumerable practice talks and reminding me that sometimes you just need to relax with a mojito. Kamini, thank you for our coffee breaks, for running away from the office with me and for being such an inspiring role model.

Although I have thoroughly enjoyed my time at Stanford, it would be sacrilege not to escape from the office sometimes and enjoy the great outdoors in California. I would like to thank my Dive Crew, especially Scott and Cynthia, for being my buddies and exploring the deep blue with me.

Last, but by no means least, I would like to acknowledge my family. Mum, Dad and Anthony, I am so incredibly thankful for your endless love, encouragement, and support from across the pond. This thesis is dedicated to you for always believing in me.

Contents

List of Figures

Chapter 1

Introduction

1.1 Overview and motivation

Determination of the structure and intrinsic physical properties of fault zones is essential to understanding the earthquake process. The physical processes that control earthquake nucleation and rupture remain enigmatic and many fault zone models are unconstrained due to a lack of in situ data. The Parkfield region in central California has been the focus of intense investigation by the geophysical community because of its seven historical magnitude six earthquakes, including the most recent earthquake that occurred in September 2004. However, despite being the most instrumented fault zone in the world and the subject of numerous studies, the physical nature of the San Andreas Fault (SAF) zone is poorly defined. Data from the San Andreas Fault Observatory at Depth (SAFOD), a deep drilling project located in Parkfield, provides a pioneering opportunity to measure the physical properties at seismogenic depths within the SAF zone and adjacent crust.

In this thesis I investigate the physical properties and state of stress of the SAF zone and surrounding crust using data acquired in the SAFOD boreholes and on regional seismic networks. I focus much of my thesis on understanding the relationships between seismic velocity anisotropy, geologic structures and stress at a variety of scales and frequencies.

The following questions regarding the SAF zone and surrounding crust at Parkfield define the motivations for this research:

1) What role does tectonic stress, fault fabric, variations in physical properties and composition play in controlling seismic anisotropy in the crust?
2) What is the nature of seismic anisotropy at a variety of scales?
3) Can we use seismic anisotropy to map variations in stress in and around the fault zone?
4) How are fault zone physical properties such as seismic velocity, resistivity, density and porosity intrinsically different from those of the adjacent country rock?
5) What is the extent and internal structure of the fault zone?
6) What are the causes of the anomalous physical properties within the fault zone?

1.1.1 Tectonic setting of Parkfield, CA

Parkfield is located in central California where the dominant structural feature in this region is the right lateral, strike-slip SAF. The Parkfield segment of the SAF is generally described as the transition zone between the 300 km-long locked portion of the fault to the southeast, which ruptured during the Fort Tejon earthquake of 1857, and the 170 km-long creeping section to the northwest (Figure 1.1). Due to right lateral slip of 320 ±20 km [Hill and Dibblee, 1953; Crowell, 1981], the SAF is a lithologic boundary between two distinctly different rock types: the highly deformed Franciscan Complex to the northeast and the relatively undeformed Salinian Block to the southwest.

The Franciscan assemblage is a highly heterogeneous, deformed mélange of weakly metamorphosed Jurassic and Cretaceous rocks. It is interpreted from seismic and potential field studies to be a tectonic wedge that has been thrust eastwards, accumulating slivers of rocks from the Great Valley sequence and fragments of the underlying ophiolite as it migrated [Wentworth et al., 1984, 1987; Walter, 1990; Wentworth and Zoback, 1990; Griscom and Jachens, 1990]. Folded and faulted Cretaceous and Cenozoic marine sedimentary strata overlie the Franciscan unconformably.

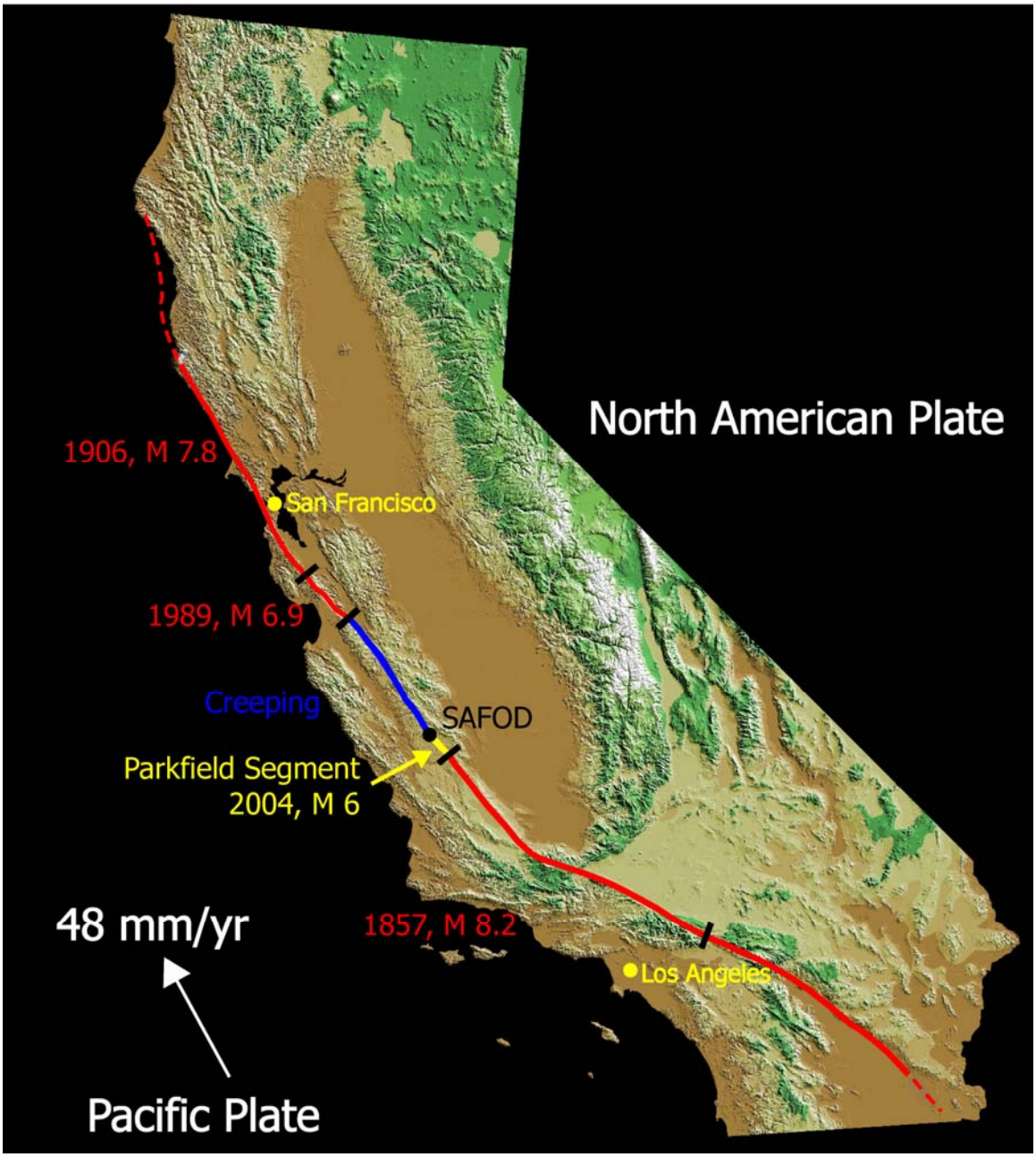

Figure 1.1: Map of California showing the tectonic setting of Parkfield, CA, at the transition between the locked and creeping segments of the San Andreas Fault and the location of SAFOD at the northern end of the Parkfield segment.

In contrast the adjacent Salinian block is characterized by fractured Cretaceous granitic rocks and local metamorphic rocks dipping gently to the west, overlain by Cenozoic marine and non-marine sediments and local volcanic rocks translated northwest from the southern Sierra Nevada.

Shallow microearthquakes (M_L = 2) in the Parkfield area are abundant between depths of approximately 3 and 12 km. Nadeau et al. [1994; 1995] and Nadeau and McEvilly [1997] observed that the microearthquakes occur in spatially tight clusters and events of the same magnitude are known to occur repeatedly at the same location.

The direction of the maximum horizontal compressive stress, S_{Hmax}, along the SAF in California has been determined from numerous observations to be approximately N30°E, at an angle of between 60° and 90° to the N40°W trending SAF [Zoback et al., 1987; Mount and Suppe, 1987; 1988; Oppenheimer et al., 1988; Jones, 1988; Townend and Zoback, 2004]. However, in the creeping section of the SAF, focal mechanism inversions very close to the fault (1-3 km) indicate a localized rotation of S_{Hmax} to an angle of about ~45° to the fault [Provost and Houston, 2001]. In the Parkfield region, measurements of S_{Hmax} (Figure 1.2) determined from focal mechanism inversions [Townend and Zoback, 2004] are consistent with stress orientations inferred from borehole breakouts in the SAFOD pilot hole [Hickman and Zoback, 2004], which indicate a clockwise rotation of S_{Hmax} to an angle of 70° to the fault at a depth of 2.2 km.

The orientation of S_{Hmax} and the absence of a heat flow anomaly [e.g., Lachenbruch and Sass, 1973; 1980] indicate that the SAF is weak in both a relative and absolute sense [Zoback et al, 1987; Hickman, 1991]. However, according to Coulomb criteria for hydrostatic pore-pressures these conditions require the coefficient of friction to be less than 0.2 for frictional failure [Lachenbruch and McGarr, 1990], which appears to be unlikely based on laboratory experiments [Byerlee, 1978]. Models to explain the weakness of the SAF are abundant in the literature [e.g., Sibson, 1973; 1992; Sleep and Blanpied, 1992; Byerlee, 1990; 1993; Sleep, 1995; Rice, 1992; Miller, 1996; Brune et al., 1993; Melosh, 1996] but the significance of many of the models can not be evaluated due to the uncertainty about the physical properties of the fault zone and the absence of direct measurements of the state of stress, porosity, permeability, etc.

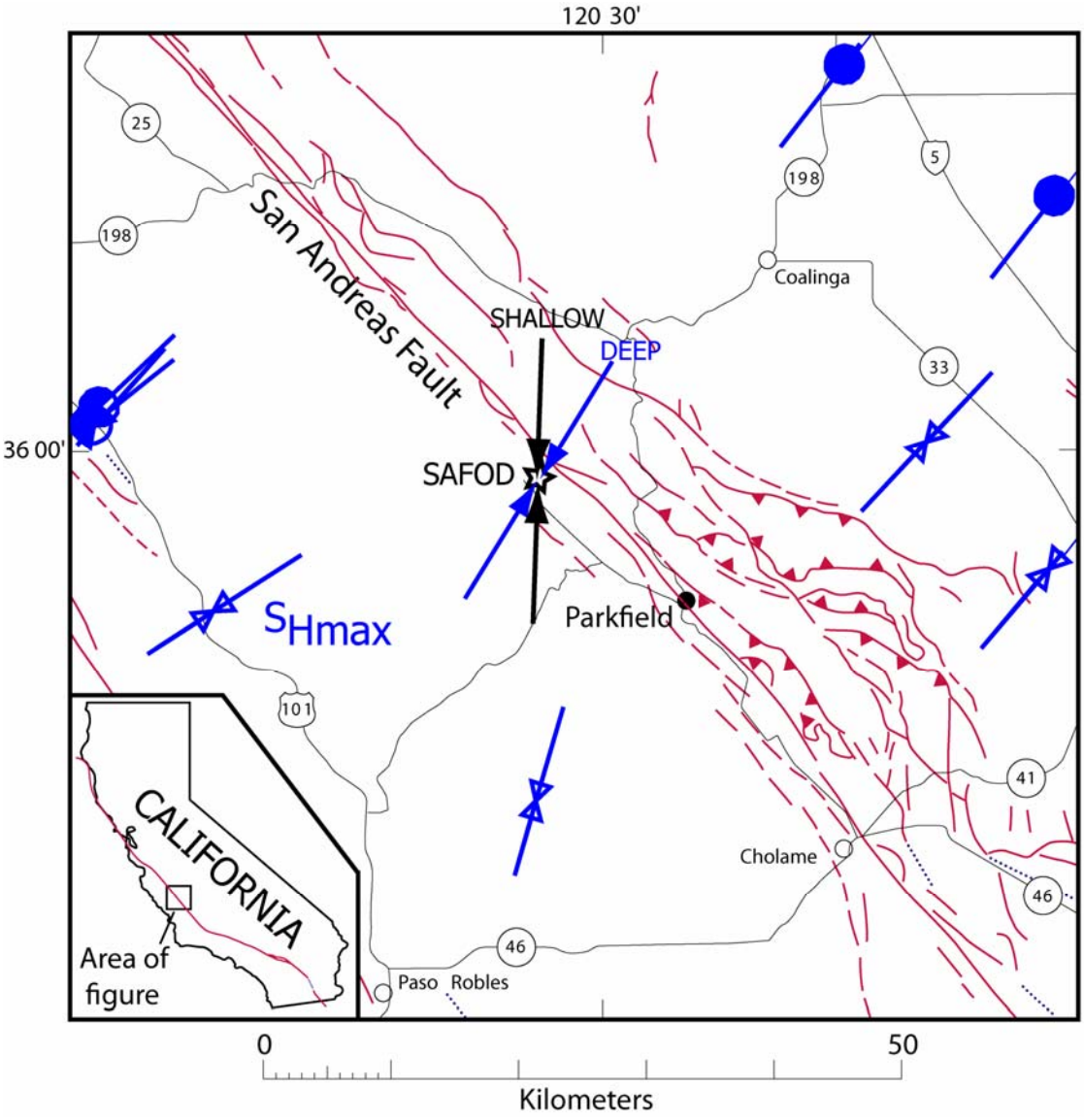

Figure 1.2: Map of the Parkfield region showing the NW-SE trending San Andreas Fault and the sub-parallel strike-slip and reverse faults in the area. The direction of maximum horizontal compression from earthquake focal mechanism inversions (circles) and wellbore breakouts (bowties) is shown by the blue lines and at a high angle to the major faults. The shallow and deep stress measurements are from the SAFOD pilot hole, and indicate a stress rotation with depth.

Corresponding to the marked differences of the rock types on either side of the SAF at Parkfield, there is a marked lateral variation in the physical properties of the crust across the fault zone. Extensive surface experiments have revealed that the seismic wave velocities and densities of the Franciscan Complex, Salinian block, and fault zone itself, are significantly different, presumably due to varying crustal properties [e.g., Wesson, 1971; Pavoni, 1973; Ellsworth, 1975; Aki and Lee, 1976; Walter and Mooney, 1982; Michelini and McEvilly, 1991; Eberhart-Phillips and Michael, 1993; Thurber et al., 1996; 1997].

However, the variation in physical properties of the crust in the immediate vicinity of the SAF is larger than one might easily explain using rock composition alone. Experiments utilizing explosion sources [Healy and Peake, 1975; Feng and McEvilly, 1983; Li et al., 1997], seismic P-wave tomography studies [Hole, 1992; Lin and Roeker, 1997; Thurber et al., 1997], and observations of fault zone guided waves [e.g., Li et al., 1990; Ben-Zion and Malin, 1990; 1991; Leary and Ben-Zion, 1992; Jongmans and Malin, 1995; Li et al, 1997], indicate that the central SAF is comprised of a low velocity fault zone, and is not a simple delineation between two rock types but has its own intrinsic physical properties.

The nature and extent of the fault zone is unknown, with different data sets illuminating different features. Studies of exhumed faults within the SAF system [Chester and Logan, 1986; Chester et al., 1993; Chester et al, 2005] provide only general constraints on physical properties for use in models of crustal faulting. Field observations indicate that a fault zone core of sheared cataclasite and ultracataclasite is a few meters wide, surrounded by a substantial damage zone of highly fractured country rock on the order of a few hundred meters wide (Figure 1.3). However, this is dependent on two assumptions: First, that the structure of the exhumed faults is indicative of processes and conditions at depth when the faults were active and thus it is reasonable to assume these properties are representative of the current situation at seismogenic depths. Second, that the exhumed faults are analogues for other faults within the SAF system and share characteristic physical properties associated with similar faulting mechanims.

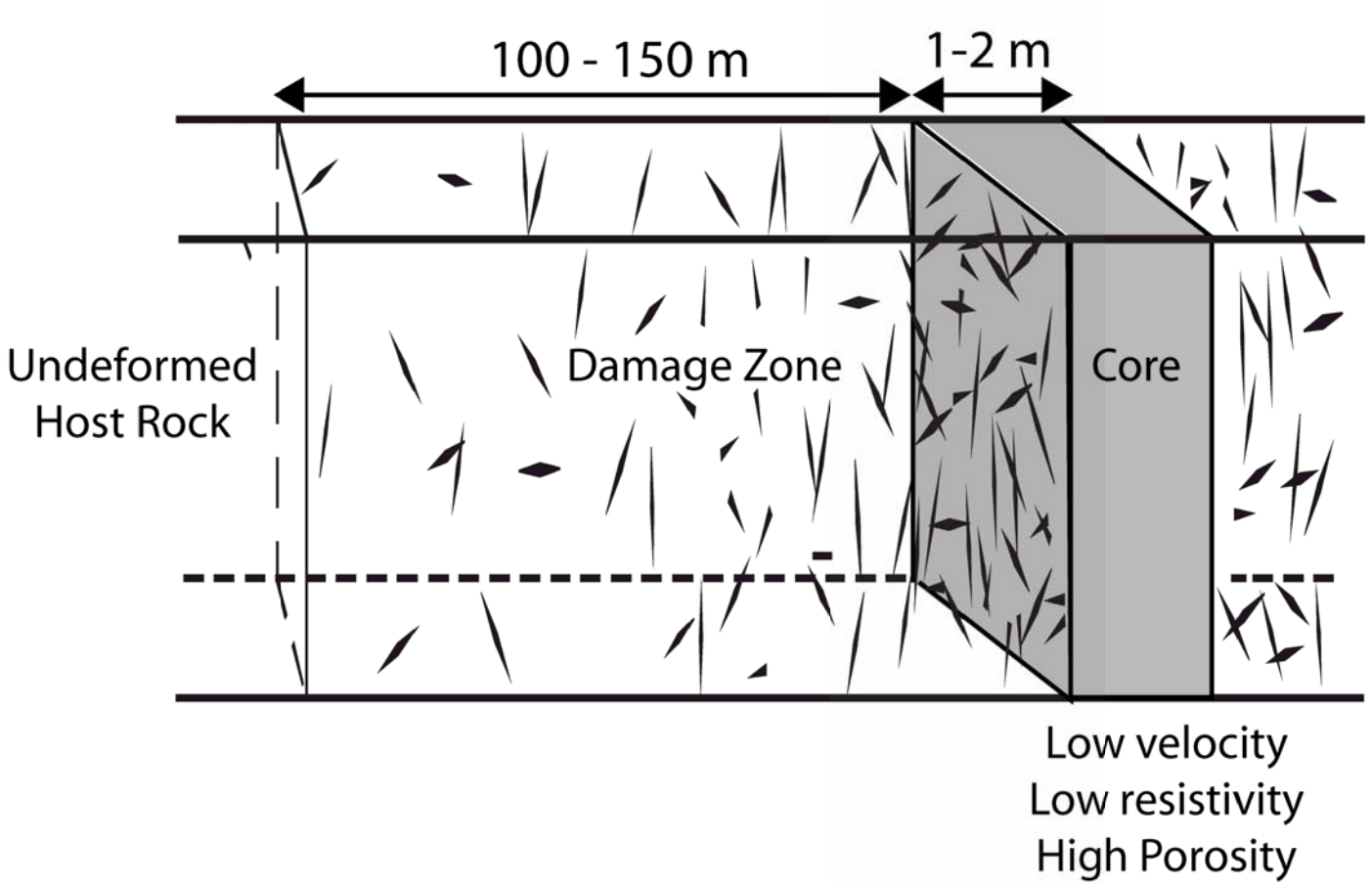

Figure 1.3: Cartoon illustrating the structure of the exhumed Punchbowl Fault, within the SAF system, as determined from field observations [Modified from Chester et al., 2005]. The fault core is a few meters wide surrounded by a 200 m wide damage zone consisting of highly fractured rocks.

Velocity models [Rymer et al., 1999] and potential field data [Griscom and Jachens, 1990; Jachens, 2002] indicate a "step" in the basement on the southwest side of the fault, reflecting the markedly different rock types on either side of the fault. This may be a result of the regional data having wavelengths greater than the width of the fault zone. In addition, earthquake relocation studies indicate that the densest clusters of earthquakes are correlated with a sharp contrast in P-wave velocities [Michael and Eberhart-Phillips, 1991].

Electrical resistivity anomalies determined from surface magnetotelluric data [Unsworth et al., 1997; 1999; 2000; Unsworth and Bedrosian, 2004; Eberhart-Phillips et al., 1990; 1995] and geophysical logs [Boness and Zoback, 2005] in the vicinity of Parkfield indicate low resistivity associated with sedimentary rocks on the southwest side if the SAF and perhaps the fault zone itself (Figure 1.4). Since the presence of fluids, serpentinite, or clays significantly lowers the resistivity of the host rock, decreased resistivity within the fault zone is clearly of great importance for understanding the earthquake process. Unsworth et al. [1997] also observe that microseismicity mapped by Nadeau et al. [1995] coincides with the western edge of the low resistivity zone. Seismic reflection studies have revealed a notable absence of coherent reflectors and studies of fault zone guided waves suggest the fault zone consists of heavily fractured material [McBride and Brown, 1986]. The Parkfield segment of the SAF also has a high V_p/V_s ratio of 1.9 [Michelini and McEvilly, 1991], revealing a much greater reduction in S-wave velocity than in P-wave velocity. The lateral extent of the fault zone remains a controversial topic with estimates ranging from 100 m [Li et al., 1990; Li and Leary, 1990] to a few kilometers [Healy and Peake, 1975; Feng and McEvilly, 1983; Li et al., 1997; Eberhart-Phillips and Michael, 1993]. This problem remains partly because of the lack of in situ data.

1.1.2 The San Andreas Fault Observatory at Depth

The San Andreas Fault Observatory at Depth (SAFOD) is a deep drilling project located approximately 10 km northwest of the town of Parkfield at the northern end of the rupture associated with the magnitude 6 Parkfield earthquakes (Figure 1.1). The drill site is 1.8 km southwest of the surface trace of the SAF in the Salinian block. The fractured granite correlates with high resistivity (determined from the inversion of surface magnetotelluric data by Unsworth and Bedrosian [2004] and shown with the background color in Figure 1.4). In contrast the SAF zone is highly conductive. SAFOD consists of two boreholes: A vertical pilot hole was drilled in 2002 to a depth of 2200 m at a distance of 1.8 km southwest from the surface trace of the SAF and a main borehole (immediately adjacent to the pilot hole) that was drilled in two phases during the summers of 2004 and 2005. The main hole is vertical to a depth of ~1500 m before deviating from vertical at an angle of 54° - 60° to the northeast toward the SAF to a total vertical depth of 3.2 km. The target for the main hole was a cluster of repeating magnitude 2 microearthquakes (approximate locations shown in Figure 1.4), which was successfully reached during phase 2.

The fundamental scientific objective of SAFOD is to make physical and chemical measurements in an active plate boundary fault at seismogenic depths. The data collected in the SAFOD boreholes range from a wide variety of geophysical measurements to geological cuttings and core and rock, water and gas geochemical data. In this thesis, I aim to integrate a number of different data sets to illuminate the physical nature of the SAF zone more effectively.

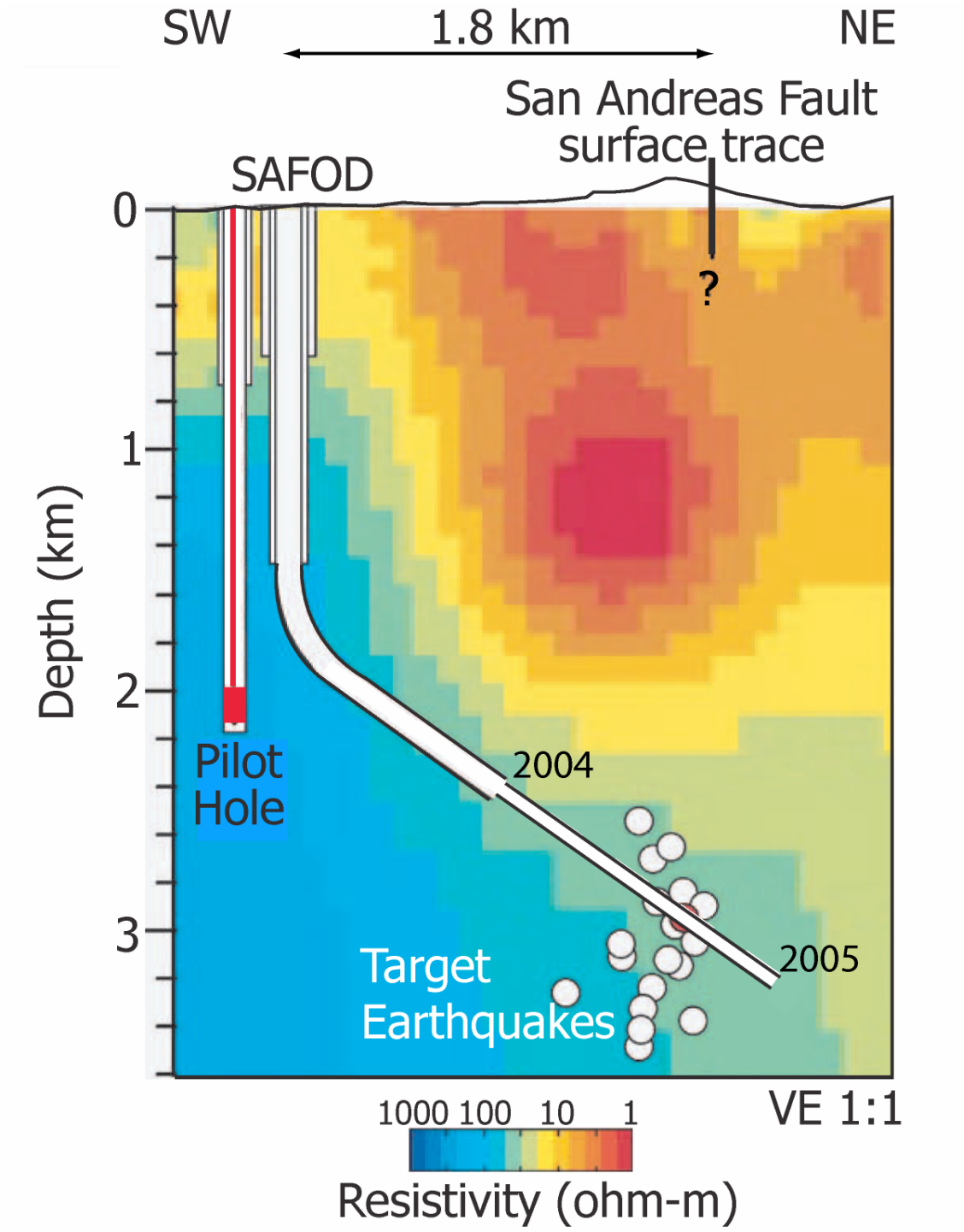

Figure 1.4: Cross-section perpendicular to the strike of the San Andreas Fault, showing the SAFOD pilot hole and main borehole. The SAF zone is associated with low resistivity derived from a surface magnetotelluric survey [Unsworth, 2000; Unsworth and Bedrosian, 2004].

1.1.3 Introduction to shear velocity anisotropy

The study of seismic anisotropy provides a powerful tool for characterizing fault zones and the adjacent crust. Shear wave velocity anisotropy is commonly referred to as shear wave splitting since the result of a shear wave traveling from an isotropic medium into an anisotropic medium is the separation of the isotropic S-wave into two quasi-shear waves. The quasi shear waves are characterized by their orthogonal polarization directions (fast and slow directions) and a delay between their arrival times at a given station (Figure 1.5). Anisotropic behavior is presumed to result from one of five known mechanisms [see reviews by Crampin et al., 1984; Crampin, 1987; Crampin and Lovell, 1991]: (1) The direct effect of stress anisotropy; (2) Microcracks opening in response to stress; (3) Rock texture associated with crystal or mineral alignment, (4) Lithologic fabrics (e.g., aligned grains); and (5) Structural properties (e.g., sedimentary layering, large-scale faults). In the crystalline upper crust the presence of anisotropy can be attributed to two broad mechanisms: Stress-related anisotropy and structural anisotropy. Fault zone anisotropy has been observed in the Loma Prieta aftershock region [Zhang and Schwartz, 1994] and the San Jacinto fault zone [Aster et al, 1990]. It appears from these studies that the effect of fault gouge is to impart a texture which creates a seismically fast direction parallel to the fault and a seismically slow direction orthogonal to the fault.

In many tectonic settings it is difficult to differentiate between stress-induced and structurally controlled shear anisotropy because S_{Hmax} is sub-parallel to major structural features. However, as noted by Zinke and Zoback [2000], the major structural features associated with the SAF are at a very high angle to the stress field. Hence, one of the reasons Parkfield is particularly suited for this study is because S_{Hmax} is at a very high angle to the trend of the major structural features (Figure 1.2), which increases our ability to distinguish between stress induced and structural anisotropy.

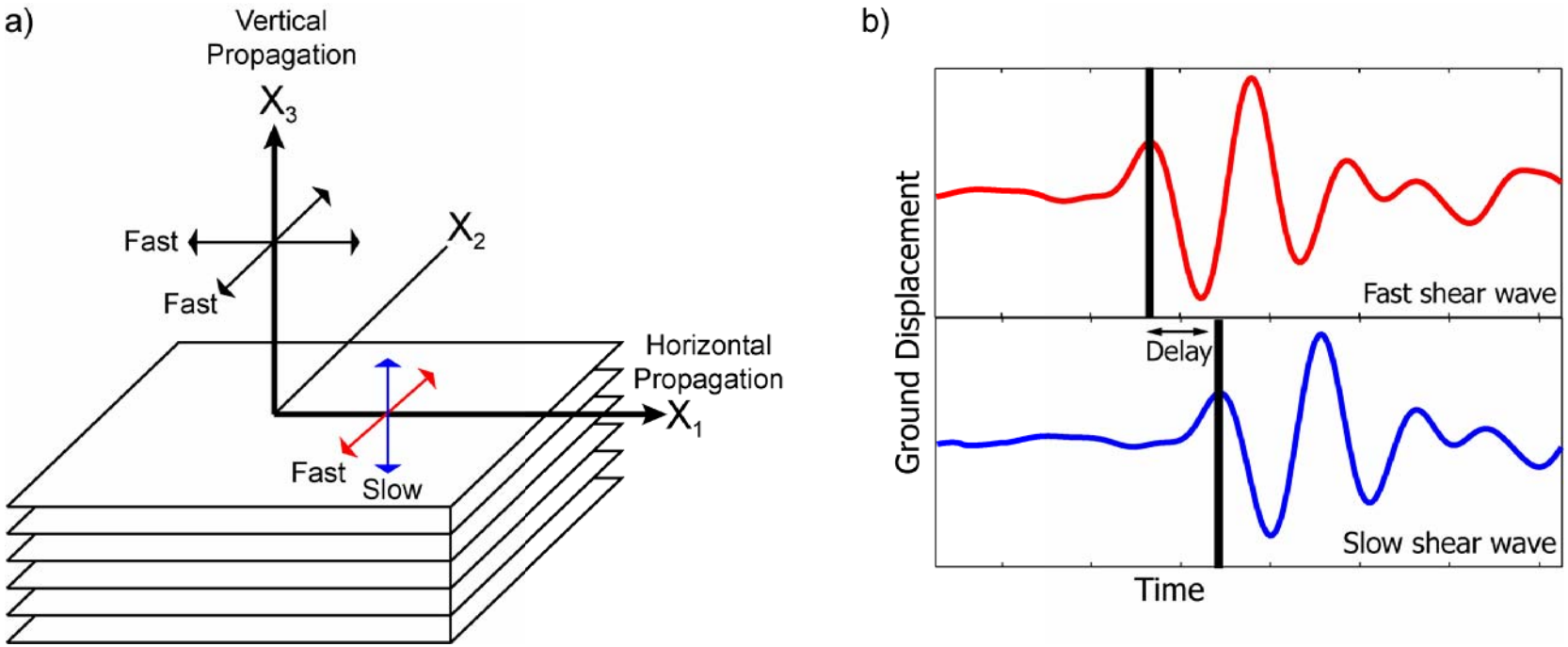

Figure 1.5: a) Schematic diagram illustrating shear velocity anisotropy for vertical and horizontal propagation within a horizontal transversely isotropic medium and b) ground displacements recorded on three-component seismometers (in the case of horizontal propagation) rotated into the fast and slow directions. Shear velocity anisotropy is characterized by the orthogonal polarizations of the fast and slow shear waves and the associated delay time between the fast and slow arrivals.

Seismic anisotropy near the SAF at Parkfield has previously been detected by Nadeau [1993] and Karageorgi et al. [1997], who found fast polarization directions consistent with the strike of the fault. More regional studies of anisotropy in the Parkfield region were conducted by Liu et al. [1993; 1997], who emphasized apparent temporal variations in seismic anisotropy as possible earthquake precursors. The results from that study exhibit significant scattering, which is partly due to topographic effects (despite using shallow borehole seismic data) and partly due to the use of poor quality data and a subjective visual analysis method.

Regional studies of seismic anisotropy yield important information on a large scale but near-surface effects nearly always obscure the true source of the anisotropic behavior. Direct measurements of anisotropy within boreholes use seismic waves that sample a much smaller portion of the crust and eliminate the ambiguity associated with more complicated ray paths. Downhole measurements of anisotropy may provide important information regarding the intrinsic properties of faults relative to surrounding country rock.

In situ seismic anisotropy was investigated at the Continental Deep Drilling Site (KTB) by the DEKORP group (Deutsches KOntinentales Reflexionseismisches Programm) using vertical seismic profiling and multiple azimuth shear wave detection [Durbaum et al., 1990]. In the metamorphic sequences, a large amount of shear wave anisotropy was observed and found to be controlled by the strike and dip of the metamorphic layers [Rabbel and Mooney, 1996]. In the granitic sections of the borehole the anisotropy was a third of that observed in the metamorphic rocks and fast polarization directions were found to be consistent with the strike of fractures [Rabbel and Mooney, 1996] in the direction of S_{Hmax}. In 1996 a borehole was drilled into the Nojima fault on Awaji Island, Japan, and the in situ physical properties and anisotropy of the fault zone were investigated [Pezard et al., 2000; Zamora et al., 2000; Tanaka et al., 2001]. It was found that the fast direction of shear waves within the hole and the direction of S_{Hmax} agreed but were almost orthogonal to the trace of the fault [Zamora et al., 2000]. In addition, acoustic velocity measurements on core and downhole measurements of anisotropy were consistent in azimuth but the magnitude of the anisotropy observed in the laboratory was dependent on the amount of fracturing within the rock samples

[Pezard et al., 2000]. Pezard et al. [2000] presented evidence that within this transpressional context the physical properties (seismic velocity, porosity, density and permeability) were intimately related to the alteration and fracturing intensity of the fault zone rocks.

It is apparent that the analysis of in situ seismic anisotropy offers the possibility to determine both composition and physical properties of the crust with significantly more refinement than conventional deep seismic refraction or reflection profiles. Most evident from all these studies is that the seismic anisotropy is correlated with both the state of stress and geologic structures.

1.2 Thesis Outline

In chapter 2, **Physical properties and seismic velocity anisotropy in the SAFOD pilot hole at Parkfield, CA**, I use data from the SAFOD pilot hole to characterize the physical properties of the Salinian granite country rocks 1.8 km from the surface trace of the San Andreas Fault near Parkfield, CA. I present an analysis of shear velocity anisotropy using data acquired with a dipole sonic log and show evidence of stress-induced anisotropy due to the closure of randomly oriented fractures in the granite due to anisotropic stresses.

Data from the SAFOD borehole provides a unique opportunity to integrate a variety of data sets to study the mechanisms controlling shear velocity anisotropy. Chapter 3, **Fine-scale controls on shear velocity anisotropy in the San Andreas Fault Observatory at Depth**, is a fine-scale analysis of dipole sonic data from phase 1 of drilling to understand the relationships between anisotropy, stress and structure. I develop a theoretical model to predict the anisotropy that will be observed in an arbitrarily oriented borehole for a given formation geometry and show that both stress-induced and structural anisotropy are present at depth in SAFOD. Structural anisotropy is prevalent in the finely laminated shales at depth but stress-induced anisotropy in the sandstone units indicates increasing fault-normal compression at a distance of only 100-300 m from the San Andreas Fault.

Improving fault zone models requires better constraints on the physical properties within the fault zone relative to the adjacent undeformed host rock. In Chapter 4, **Physical properties and seismic velocity anisotropy across the San Andreas Fault**, I document the anomalous physical properties of the San Andreas Fault and examine the internal structure and extent of the fault zone. The actively deforming region of the San Andreas Fault is characterized by high porosity, low resistivity and very low sonic velocity, in addition to being highly brecciated, and there is evidence of a 20 m wide fault core imbedded within a 200-300 m clay-rich fractured damage zone. Observations of shear velocity anisotropy in a transect across the fault zone are used to infer the orientation of S_{Hmax}, which is at a high angle to the strike of the fault except within the fault core where there is a visible rotation to ~40° to the fault consistent with the Rice Model of a weak San Andreas Fault in a strong crust.

In Chapter 5, **Mapping stress and structurally-controlled shear velocity anisotropy in California**, I apply the concepts of stress-induced and structural anisotropy to a regional study of shear velocity anisotropy. Using data from seismic stations in California, I demonstrate that with careful data analysis, stations located along major faults exhibit structural anisotropy and stations located in the adjacent crust exhibit stress-induced anisotropy. The observation of structural anisotropy at these seismic frequencies indicates that the intrinsic physical properties of the fault are different to those of the adjacent crust and the fault extends laterally 200-500 m. Being able to differentiate between structural and stress-induced anisotropy allows us to use anisotropy to map stress close to active faults where other techniques have limitations. I find evidence of fault-normal compression close to the fault supporting the hypothesis of a weak fault slipping at low levels of resolved shear stress.

References

Aki, K., and Lee, W. H. K., 1976, Determination of three-dimensional velocity anomalies under a seismic array using P-arrival times from local earthquakes: 1. A homogeneous initial model: *J. Geophys. Res*., **81**, 4381-4399.

Aster, R. C., Shearer, P. M., and Bergner, J., 1990, Quantitative measurements of shear wave polarizations at the Anza seismic network, Southern California; implications for shear wave splitting and earthquake prediction: *J. Geophys. Res.*, **95**, 12449-12473.

Ben-Zion, Y., and Malin, P. E., 1990, Fault zone head waves in the San Andreas fault zone near Parkfield, California: *Eos Trans. AGU*, **71**, 1474.

Ben-Zion, Y., and Malin, P. E., 1991, San Andreas fault zone head waves near Parkfield, California: *Science*, **251**, 1592-1594.

Boness, N. L., and Zoback, M. D., 2005, Fine-scale controls on shear velocity anisotropy in the San Andreas Fault Observatory at Depth: *Geophysics*, submitted.

Brune, J. N., Brown, S., and Johnson, P. A., 1993, Rupture mechanism and interface separation in foam rubber models of earthquakes: a possible solution to the heat flow paradox and the paradox of large overthrusts: *Tectonophysics*, **218**, 59-67.

Byerlee, J., 1978, Friction of rocks: *Pure Appl. Geophys*., **116**, 615-626.

Byerlee, J., 1990, Friction, overpressure and fault normal compression: *Geophys. Res. Lett*., **17**, 2109-2112.

Byerlee, J., 1993, Model for episodic flow of high-pressure water in fault zones before earthquakes: *Geology*, **21**, 303-306.

Chester, F. M., Evans, J. P., and Biegel, R. L., 1993, Internal structure and weakening of the San Andreas fault: *J. Geophys. Res*., **98**, 771-786.

Chester, F. M., and Logan, J. M., 1986, Implications for mechanical properties of brittle faults from observations of the Punchbowl fault, California: *Pure Appl. Geophys*., **124**, 79-106.

Chester, J., Chester, F. M., and Kronenberg, A. K., 2005, Fracture energy of the Punchbowl fault, San Andreas system: *Nature*, **437**, 133-136.

Crampin, S., 1987, Geological and industrial implications of extensive-dilatancy anisotropy: *Nature*, **328**, 491-496.

Crampin, S., Chesnokov, E. M., and Hipkin, R. G., 1984, Seismic anisotropy - the state of the art II: *Geophys. J. R. astr. Soc*. , **76**, 1-16.

Crampin, S., and Lovell, J. H., 1991, A decade of shear-wave splitting in the Earth's crust: what does it mean? what use can we make of it? and what should we do next?: *Geophys. J. Int*., **107**, 387-407.

Crowell, J. C., 1981, An outline of the tectonic history of southeastern California, Ruby volume 1, in Ernst, W. G., ed., *The geotectonic development of California*: Prentice-Hall, Englewood Cliffs, N. J., 584-600.

Durbaum, H.-J., Reichert, C., and Bram, K., 1990, Integrated seismics oberpfalz, 1989: *KTB report*, **90**-6b.

Eberhart-Phillips, D., and Michael, A. J., 1993, Three-dimensional velocity structure, seismicity, and fault structure in the Parkfield region, central California: *J. Geophys. Res*., **98**, 15737-15758.

Eberhart-Phillips, D. M., Labson, V. F., Stanley, W. D., Michael, A. J., and Rodrigues, B. D., 1990, Preliminary velocity and resistivity models of the Loma Prieta earthquake region: *Geophys. Res. Lett*., **17**, 1235-1238.

Eberhart-Phillips, D. M., Stanley, W. D., Rodrigues, B. D., and Lutter, W. J., 1995, Surface seismic and electrical methods to detect fluids related to faulting: *J. Geophys. Res*., **100**, 12919-12936.

Ellsworth, W. L., 1975, Bear Valley, California earthquake sequence of February-March, 1972: *Bull. Seismol. Soc. Am.*, **65**, 483-506.

Feng, R., and McEvilly, T. V., 1983, Interpretation of seismic reflection profiling data for the structure of the San Andreas fault zone: *Bull. Seismol. Soc. Am*., **73**, 1701-1720.

Griscom, A., and Jachens, R. C., 1990, Tectonic implications of gravity and magnetic models along east-west seismic profiles across the Great Valley near Coalinga, in Rymer, M. J., and Ellsworth, W. L., eds., *The Coalinga, California earthquake of May 2, 1983*: U. S. Geol. Survey Prof. Pap., **1487**, Reston, VA, 69-78.

Healy, J., and Peake, L., 1975, Seismic velocity structure along a section of the San Andreas fault near Bear Valley, California: Bull*. Seismol. Soc. Am.*, **65**, 1177-1197.

Hickman, S. H., 1991, Stress in the lithosphere and the strength of active faults: *Rev. Geophys*., **29**, 759-775.

Hickman, S. H., and Zoback, M. D., 2004, Stress orientations and magnitudes in the SAFOD pilot hole: *Geophys. Res. Lett.*, **31**, L1S12.

Hill, M. L., and Dibblee, Jr., T. W., 1953, San Andreas, Garlock, and Big Pine faults, California: A study of the character, history, and tectonic significance of their displacements: *Bull. Geol. Soc. Am*., 64, 443-458.

Hole, J. A., Catchings, R. D., St. Clair, K. C., Rymer, M. J., Okaya, D. A., and Carney, B. J., 2001, Steep-dip seismic imaging of the shallow San Andreas fault near Parkfield: *Science*, **294**, 1513-1515.

Jachens, R. C., 2002, Three-dimensional model based on geophysics of the San Andreas Fault Observatory at Depth (SAFOD), near Parkfield, Calif.: http://wrgis.wr.usgs.gov/docs/gump/meghan/parkfield/parkfield.html.

Jones, L. M., 1988, Focal mechanisms and the state of stress on the San Andreas Fault in Southern California: *J. Geophys. Res*., **93**, 8869-8891.

Jongmans, D., and Malin, P. E., 1995, Microearthquake S-wave observations from 0 to 1 km in the Varian well at Parkfield, California: *Bull. Seismol. Soc. Am.*, **85**, 1805-1820.

Karegeorgi, E., McEvilly, T. V., and Clymer, R., 1997, Seismological studies at Parkfield IV; variations in controlled-source waveform parameters and their correlation with seismicity, 1987 to 1995: *Bull. Seismol. Soc. Am*., **87**, 39-49.

Lachenbruch, A. H., and McGarr, A. F., 1990, Stress and heat flow: *U. S. Geological Survey Professional Paper*, **1515**, 261-277.

Lachenbruch, A. H., and Sass, J. H., 1973, Thermo-mechanical aspects of the San Andreas Fault system, in *Proceedings of Tectonic problems of the San Andreas Fault system*: Stanford University Publications, Geological Sciences, **13**, 192-205.

Lachenbruch, A. H., and Sass, J. H., 1980, Heat flow and energetics of the San Andreas fault zone: *J. Geophys. Res*., **85**, 6185-6222.

Leary, P., and Ben-Zion, Y., 1992, A 200-m wide fault zone low velocity layer on the San Andreas fault at Parkfield: results from analytic waveform fits to trapped wave groups: *Seis. Res. Lett*., **63**, 62.

Li, Y-G., and Leary, P., 1990, Fault zone trapped seismic waves: *Bull. Seismol. Soc. Am*., **80**, 1245-1274.

Li, Y-G., Ellsworth, W. L., Thurber, C. F., Malin, P. E., and Aki, K., 1997, Fault-zone guided waves from explosions in the San Andreas fault and Parkfield and Cienega Valley, California: *Bull. Seismol. Soc. Am*., **87**, 210-221.

Li, Y-G., Leary, P. C., Aki, K., and Malin, P. E., 1990, Seismic trapped modes in the Oroville and San Andreas fault zones: *Science*, **249**, 763-765.

Lin, C. H., and Roecker, S. W., 1997, Three-dimension P-wave velocity structure of the Bear-Valley region of central California: *Pure Appl. Geophys*., **149**, 667-688.

Liu, Y., Booth, D. C., Crampin, S., Evans, R., and Leary, P., 1993, Shear-wave polarizations and possible temporal variations in shear-wave splitting at Parkfield: *Canadian J. Expl. Geophys*., **29**, 380-390.

Liu, Y., Crampin, S., and Main, I., 1997, Shear-wave anisotropy: spatial and temporal variations in time delays at Parkfield, Central California: *Geophys. J. Int*., **130**, 771-785.

McBride, J. H., and Brown, L. D., 1986, Reanalysis of the COCORP deep seismic reflection profile across the San Andreas Fault, Parkfield, California: *Bull. Seismol. Soc. Am*., **76**, 1668-1686.

Melosh, H. J., 1996, Dynamical weakening of faults by acoustic fluidization: *Nature*, **379**, 601-606.

Michael, A. J., and Eberhart-Phillips, D., 1991, Relations among fault behavior, subsurface geology, and three-dimensional velocity models: *Science*, **253**, 651-654.

Michelini, A., and McEvilly, T. V., 1991, Seismological studies at Parkfield. I. Simultaneous inversion for velocity structure and hypocenters using cubic B-splines parameterization: *Bull. Seismol. Soc. Am*., **81**, 524-552.

Miller, S. A., 1996, Fluid-mediated influence of adjacent thrusting on seismic cycle at Parkfield: *Nature*, **382**, 799-802.

Mount, V. S., and Suppe, J., 1987, State of stress near the San Andreas Fault; implications for wrench tectonics: *Geology*, **15**, 1143-1146.

Mount, V. S., and Suppe, J., 1988, Present-day stress directions in California determined through borehole breakout analysis: *AAPG Bull*., **72**, 390.

Nadeau, R. M., 1993, A search for evidence of large scale fault aligned seismic anisotropy at the Parkfield HRSN; implications for anisotropic permeability structures, fault zone weakness, and temporal stability studies: *Seis. Res. Lett*., **64**, 54.

Nadeau, R. M., Antolik, M., Johnson, P., Foxall, W., and McEvilly, T. V., 1994, Seismological studies at Parkfield III: Microearthquake clusters in the study of fault-zone dynamics: *Bull. Seismol. Soc. Am*., **84**, 247-263.

Nadeau, R. M., Foxall, W., and McEvilly, T. V., 1995, Clustering and periodic recurrence of microearthquakes on the San Andreas fault at Parkfield, California: *Science*, **267**, 503-507.

Nadeau, R. M., and McEvilly, T. V., 1997, Seismological studies at Parkfield V: Characteristic microearthquake sequences as fault-zone drilling targets: *Bull. Seismol. Soc. Am*., **87**, 1463-1472.

Oppenheimer, D. H., Reasenberg, P. A., and Simpson, R. W., 1988, Fault plane solutions for the 1984 Morgan Hill, California, earthquake sequence; evidence for the state of stress on the Calaveras Fault: *J. Geophys. Res*., **93**, 9007-9026.

Pavoni, N., 1973, A structural model for the San Andreas fault along the northeast side of the Gabilan Range, in *Proceedings of Tectonic Problems of the San Andreas Fault System*: Stanford University Publications, Geological Sciences, **13**, 259-267.

Pezard, P. A., Ito, H., Hermitte, D., and Revil, A., 2000, Electrical properties and alteration of granodiorites from the GSJ Hirabayashi hole, Japan, in Ito, H., Fujimoto, K., Tanaka, H., and Lockner, D., eds, *International workshop of the Nojima fault core and borehole data analysis:* U. S. Geol. Survey Open-File Report, **000-129**, Tsukuba, Japan, 255-262.

Provost, A.-S., and H. Houston, 2001, Orientation of the stress field surrounding the creeping section of the San Andreas fault: Evidence for a narrow mechanically-weak fault zone: *J. Geophys. Res*., **106**, 11,373-11,386.

Rabbel, W., and Mooney, W. D., 1996, Seismic anisotropy of the crystalline crust: what does it tell us?: *Terra Nova*, **8**, 16-21.

Rice, J. R., 1992, Fault stress states, pore pressure distributions, and the weakness of the San Andreas Fault, in Evans, B., and Wong, T., eds, *Fault mechanics and transport properties of rocks*: Academic Press, San Diego, 475-503.

Rymer, M.J., Catchings, R.D., Goldman, M.R., Fuis, G.S., Huggins, R., Lippus, C., and Hole, J.A., 1999, Structural Complexity in the San Andreas fault zone as revealed by high-resolution seismic reflection and refraction profiling near Parkfield, California: *Eos Trans. AGU*, **80**, F706.

Sibson, R. H., 1973, Interactions between temperature and pore-fluid pressure during earthquake faulting and a mechanism for partial or total stress relief: *Nature*, **243**, 66-68.

Sibson, R. H., 1992, Implications of fault-valve behavior for rupture nucleation and recurrence: *Tectonophysics*, **211**, 283-293.

Sleep, N. H., 1995, Ductile creep, compaction, and rate and state dependent friction within major fault zones: *J. Geophys. Res*., **100**, 13065-13080.

Sleep, N. H., and Blanpied, M. L., 1992, Creep, compaction and the weak rheology of major faults: *Nature*, **359**, 687-692.

Tanaka, H., Fujimoto, K., Ohtani, T., and Ito, H., 2001, Structural and chemical characterization of shear zones in the freshly activated Nojima fault, Awaji Island, southwest Japan: *J. Geophys. Res*., **106**, 8789-8810.

Thurber, C., Roecker, S., Ellsworth, W. L., Chen, Y., Lutter, W., and Sessions, R., 1997, Three-dimensional seismic image of the San Andreas fault in the northern Gabilan range, central California: Evidence for fluids in the fault zone: *Geophys. Res. Lett*., **24**, 1591-1594.

Thurber, C., Roecker, S., Lutter, W., and Ellsworth, W. L., 1996, Imaging the San Andreas fault with explosions and earthquake sources: *Eos Trans. AGU*, **77**, 45, 57 and 58.

Townend, J., and Zoback, M. D., 2004, Regional tectonic stress near the San Andreas fault in central and southern California: *Geophys. Res. Lett*., **31**, L15S11.

Unsworth, M. J., and Bedrosian, P. A., 2004, Electrical resistivity structure at the SAFOD site from magnetotelluric exploration: *Geophys. Res. Lett*., **31**, L12S05.

Unsworth, M. J., Bedrosian, P., Eisel, M., Egbert, G. D., and Siripunvaraporn, W., 2000, Along strike variations in the electrical structure of the San Andreas Fault at Parkfield, California: *Geophys. Res. Lett*., **27**, 3021-3024.

Unsworth, M. J., Egbert, G. D., and Booker, J. R., 1999, High-resolution electromagnetic imaging of the San Andreas Fault in Central California: *J. Geophys. Res*., **104**, 1131-1150.

Unsworth, M. J., Malin, P. E., Egbert, G. D., and Booker, J. R., 1997, Internal structure of the San Andreas Fault at Parkfield, California: *Geology*, **25**, 359-362.

Walter, A. W., 1990, Upper-crustal velocity structure near Coalinga, as determined from seismic-refraction data, in Rymer, M. J., and Ellsworth, W. L., *The Coalinga, California earthquake of May 2, 1983*: U. S. Geol. Survey Prof. Pap.,**1487**, Reston, VA, 23-40.

Walter, A. W., and Mooney, W. D., 1982, Crustal structure of the Diablo and Gabilan ranges, central California: a reinterpretation of existing data: *Bull. Seismol. Soc. Am*., **72**, 1567-1590.

Wentworth, C. M., Blake, Jr. M. C., Jones, D. L., Walter, A. W., and Zoback, M. D., 1984, Tectonic wedging associated with emplacement of the Franciscan assemblage, California Coast Ranges, in Blake, Jr., M. C., ed., *Franciscan geology of North California*: Society of Economic Paleontologists and Mineralogists, **43**, Pacific Section, Bakersfield, CA, 163-173.

Wentworth, C. M., and Zoback, M. D., 1990, Structure of the Coalinga region and thrust origin of the earthquake, in Rymer, M. J., and Ellsworth, W. L., *The Coalinga, California earthquake of May 2, 1983*: U. S. Geol. Survey Prof. Pap., **1487**, Reston, VA, 41-68.

Wentworth, C. M., Zoback, M. D., Griscom, A., Jachens, R. O., and Mooney, W. D., 1987, A transect across the Mesozoic accretionary margin of Central California: Geophys*. J. R. astr. Soc*., **89**, 105-110.

Wesson, R. L., 1971, Travel-time inversion for laterally inhomogeneous crustal velocity models: *Bull. Seismol. Soc. Am*., **61**, 729-746.

Zamora, M., Pezard, P. A., and Ito, H., 2000, Anisotropy of elastic and anelastic properties of granites from the GSJ Hirabayashi hole, Japan, in Ito, H., Fujimoto, K., Tanaka, H., and Lockner, D., eds., *International workshop of the Nojima fault core and borehole data analysis*: U. S. Geol. Survey Open-File Report, **000-129**, Tsukuba, Japan, 227-231.

Zhang, Z., and Schwartz, S. Y., 1994, Seismic anisotropy in the shallow crust of the Loma Prieta segment of the San Andreas fault system: *J. Geophys. Res*., **95**, 9561-9661.

Zinke, J. C., and Zoback, M. D., 2000, Structure-related and stress-induced shear-wave velocity anisotropy: Observations from microearthquakes near the Calaveras Fault in Central California: *Bull. Seismol. Soc. Am.*, **90**, 1305-1312.

Zoback, M. D., Zoback, M. L., Mount, V. S., Suppe, J., Eaton, J. P., Healy, J. H., Oppenheimer, D., Reasenberg, P., Jones, L., Raleigh, C. B., Wong, I. G., Scotti, O., and Wentworth C., 1987, New evidence on the state of stress of the San Andreas fault system: *Science*, **238**, 1105-1111.

Chapter 2

Stress-induced seismic velocity anisotropy and physical properties in the SAFOD pilot hole.

Abstract

A comprehensive suite of geophysical logs was collected in the SAFOD pilot hole from a depth of 775 m to 2150 m in highly fractured Salinian granite. The pilot hole intersected numerous macroscopic fractures and faults with extremely varied orientations. Despite the highly variable orientation of the fractures and faults, the fast polarization direction of the shear waves is very consistent with the direction of maximum horizontal compression determined from wellbore breakouts and drilling induced tensile fractures. At least three major shear zones were intersected by the borehole that are characterized by anomalously low velocity and resistivity, anomalously high shear velocity anisotropy and an absence of stress-induced wellbore breakouts (which suggests anomalously low differential stress). We argue that the physical mechanism responsible for the seismic velocity anisotropy observed in the pilot hole is the preferential closure of fractures in response to an anisotropic stress state.

The material in this chapter has appeared in Boness, N. L., and Zoback, M. D., 2004, Stress-induced seismic velocity anisotropy and physical properties in the SAFOD Pilot Hole in Parkfield, CA.: *Geophys. Res. Lett*., **31**, L15S17, doi:10.1029/2003GL019020.

2.1 Introduction

In the summer of 2002 the pilot hole for the San Andreas Fault Observatory at Depth (SAFOD) was drilled to a depth of 2.15 km through 768 m of tertiary sediments and into Salinian granite. Data from the pilot hole provides a unique opportunity to measure the physical properties of the shallow crust adjacent to the San Andreas Fault. In this paper we present shear wave velocity anisotropy observations and correlate them with measurements of P- and S-wave velocity, resistivity, density and porosity, the distribution of faults and fractures intersecting the borehole and the state of stress inferred from borehole measurements.

2.2 Faults, fractures and physical properties

The right lateral, strike-slip San Andreas Fault is the dominant structural feature in the Parkfield region. Secondary, strike-slip and shallow thrust faults with a sub-parallel northwest-southeast trend also occur throughout the area. Based on studies of P-wave velocity determined from a seismic reflection/refraction profile [Catchings et al., 2002] and interpretation of potential field data [R. Jachens, personal communication, 2003] it was anticipated that the pilot hole would encounter fractured granite beneath ~750 m of Tertiary and Quaternary sedimentary rocks; the fractured Salinian granite was encountered at 768 m. A comprehensive suite of geophysical logs was collected in the fractured granite from a depth of 775 m to 2150 m. P-and S-wave sonic velocity, electrical resistivity, gamma ray, and density were recorded over the entire depth range at a 15 cm sampling interval. Figure 2.1 shows these data after applying a 3 m running average to the logs. Electrical and ultrasonic image logs were also acquired in the borehole to facilitate an analysis of the fractures and faults intersected by the borehole as well as stress-induced wellbore failures such as breakouts and drilling-induced tensile cracks.

As expected, the pilot hole velocity logs show an overall increase in P- and S-wave velocity with depth (Figure 2.1). The compressional wave velocity, V_p, ranges from approximately 5 km/s at a depth of 775 m to 5.65 km/s at a depth of 2150 m. Similarly, the shear wave velocity, V_s, ranges from 2.8 km/s to 3.25 km/s.

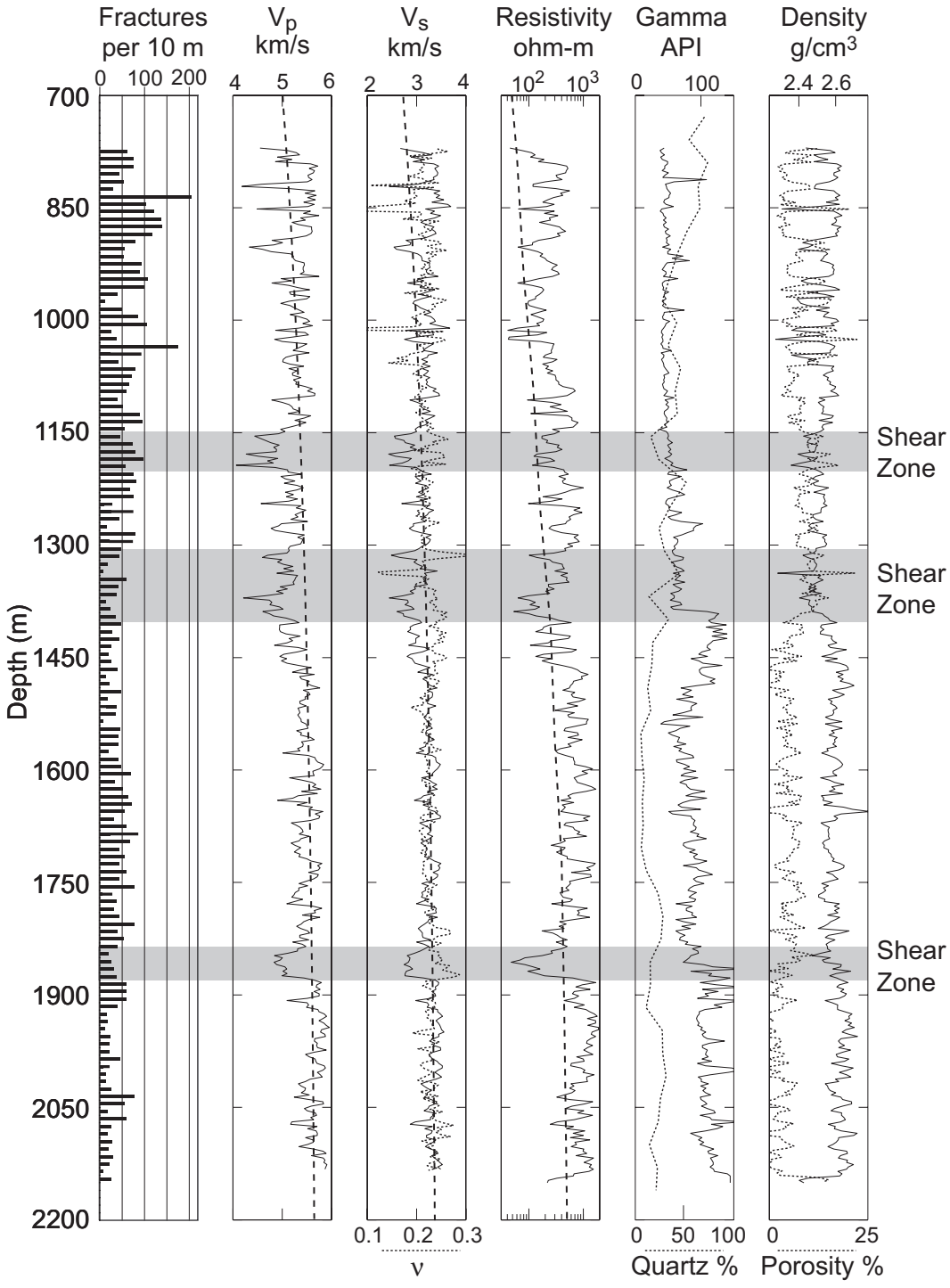

Figure 2.1: Distribution of macrofractures intersected by the pilot hole as determined from the FMI log and physical property logs acquired in the pilot hole averaged over 3 m depth intervals. Dashed lines on the seismic velocities indicate gross trends with depth and the dashed line on the resistivity is the model determined by Unsworth et al. [2000]. Intervals of the borehole with significantly anomalous physical properties, interpreted to be major shear zones, are highlighted.

Both the P- and S-wave data reveal the presence of anomalously low velocity zones. These include intervals at 1150–1200 m, 1310–1420 m and 1835–1880 m that correlate with regions of intense fracturing (see below). We also note that the V_p/V_s ratio has an average value of 1.7 (equivalent to a Poisson's ratio, υ, of 0.24) but in the three intervals of lower velocity this ratio increases. This increase is especially prominent within the low velocity zones at 1310–1420 m and 1835–1880 m, where V_p/V_s reaches its maximum value of approximately 1.9 ($\upsilon = 0.3$).

Overall, densities in the pilot hole increase with depth from approximately 2.5 g/cm^3 to 2.7 g/cm^3, which is expected for rock with granitic composition. Porosity values, determined from the density log, are between 2 and 15 % for most of the log, indicating highly fractured granite. Within the interval 1150–1200 m there is a decrease in density and a corresponding increase in porosity. At a depth of 1400 m there is a 5 % decrease in porosity and a simultaneous density increase of 0.2 g/cm^3. Porosity decreases by a further 2 % at a depth of 1850 m and density increases to a value of 2.7 g/cm^3, which remains virtually constant to the bottom of the well.

Resistivity increases with depth in the pilot hole from about 30 ohm-m at 800 m depth to 1000 ohm-m at the bottom of the borehole (Figure 2.1), an order of magnitude lower than those associated with laboratory measurements of intact crystalline rock [Pezard and Luthi, 1988; Zablocki, 1964]. Unsworth et al. [2000] determined the resistivity structure along a profile through the drill site by modeling surface magnetotelluric data. We find reasonable agreement between the log data and this model (both shown in Figure 2.1), although Unsworth et al.'s [2000] model seems to slightly underestimate the resistivity at depth. Two of the intervals noted above (1310–1420 m and 1835–1880 m) have resistivities that are significantly lower than the overall trend with depth. The resistivity of fractured crystalline rock is very sensitive to the presence of interstitial fluids [Brace et al., 1965; Brace and Orange, 1968; Brace, 1971] and alteration minerals [e.g., Palacky, 1987]. As the porosity shows no significant increase in these zones we assume the low resistivity is a result of the mineralogy.

Variations in gamma ray radiation are often associated with changes in lithology, particularly the presence of clay minerals and an increase in feldspar. The gamma ray log

from the pilot hole shows an overall increase in the amount of radiation with depth from about 25 to 75 API units. We observe two significant increases in the gamma radiation (over 50 API units) at depths of approximately 1400 m and 1850 m. These variations are associated with significant decreases in the amount of quartz, increases in the amount of feldspar, clay minerals and oxides as determined from mineralogical point counts of cuttings collected in the pilot hole during the drilling phase [M. Rymer, personal communication, 2003]. The intervals at 1310–1420 m and 1835–1880 m are also associated with significant increases in the thermal conductivity [Williams et al., 2004] and large increases in the magnetic susceptibilities [McPhee et al., 2004]. An increase in gas emissions was recorded at the time of drilling as each of the intervals at 1150–1200 m, 1310–1420 m and 1835–1880 m was penetrated [Erzinger et al., 2004], although elevated pore pressure was not observed.

The distribution and orientation of macroscopic faults and fractures intersected by the pilot hole was obtained by analyzing data from a Formation Micro Imager (FMI) log [Ekstrom et al., 1987] acquired in the pilot hole. The abundance of macroscopic faults and fractures decreases from approximately 125 per 10 m interval in the upper section of the log (Figure 2.1) to about 25 per 10 m interval at the bottom of the borehole. There are several intervals where the granite is so highly faulted and fractured that the number of individual features within each of these zones is impossible to ascertain. The most prominent of these intervals are between 1150–1200 m, 1310–1420 m and 1835–1880 m, the same intervals with anomalous geophysical properties described above.

The orientation of the macrofractures is highly variable at all depths, as can be seen in the stereonets and rose diagrams of fracture strike in Figure 2.2. We hypothesize that the anomalous intervals noted above (1150–1200 m, 1310–1420 m and 1835–1880 m) are associated with major shear zones cutting across the borehole. In addition to having anomalous geophysical properties and an extremely high number of fractures and faults, these zones are hydraulically conductive (as indicated by the increase in gases) and thus appear to be active faults [Barton et al., 1995; Townend and Zoback, 2000]. The high V_p/V_s ratio in these intervals is indicative of increased microcracks [Moos and Zoback, 1983] and/or materials with a low shear modulus. However, the porosity log does not reveal high porosity confined within any of the anomalous intervals, but rather

shows a step in density/porosity indicating a change of lithology. These step changes in density/porosity are correlated with analogous steps in gamma ray radiation values implying a change of lithology across the fault(s) in the shear zones.

2.3 Seismic velocity anisotropy

Data from a Dipole Sonic Shear Image (DSI) log [e.g., Chen, 1988; Mueller et al., 1994] acquired in the pilot hole is used to assess shear wave velocity anisotropy. The DSI tool consists of a relatively low frequency source (0.8–5 KHz), which causes a flexing of the borehole wall that, in turn, directly excites shear waves penetrating approximately 1.5 m into the formation. The flexural wave is dispersive with low frequencies having a large penetration depth and reflecting shear velocities away from the wellbore. The effect of stress concentrations around the borehole is removed by filtering out the high frequencies that correspond to penetration depths of less than 3 borehole radii (equivalent to about 67 cm for the pilot hole).

The results of the shear wave anisotropy analysis are shown in Figure 2.2 with the fast polarization directions shown for ten discrete 150 m intervals of the borehole. The amount of velocity anisotropy (defined as $100(V_{s1} - V_{s2})/V_{s1}$, where V_{s1} is the fastest shear velocity and V_{s2} is the slower velocity) is averaged over 3 m intervals and found to decrease with depth from approximately 10 % at 775 m to 3 % at 2150 m (Figure 2.3). We ensure data quality of the dipole shear wave data by requiring the following: 1) A velocity anisotropy greater than 2 % (although it cannot be ruled out that low amounts of shear anisotropy below this tool sensitivity may be indicative of a less anisotropic formation); 2) An energy difference between the fast and slow waves of more than 50 %; 3) A minimum energy greater than 15 %. We observe intervals in the pilot hole where anisotropy appears to increase significantly above the overall trend. For example, in the interval of 1310–1420 m the amount of anisotropy increases from approximately 4 % to 11 %. This phenomenon is also observed clearly between depths of 1835 and 1880 m (Figure 2.3). Caliper measurements of borehole diameter indicate that this increase in anisotropy is not an artifact due to borehole shape or size.

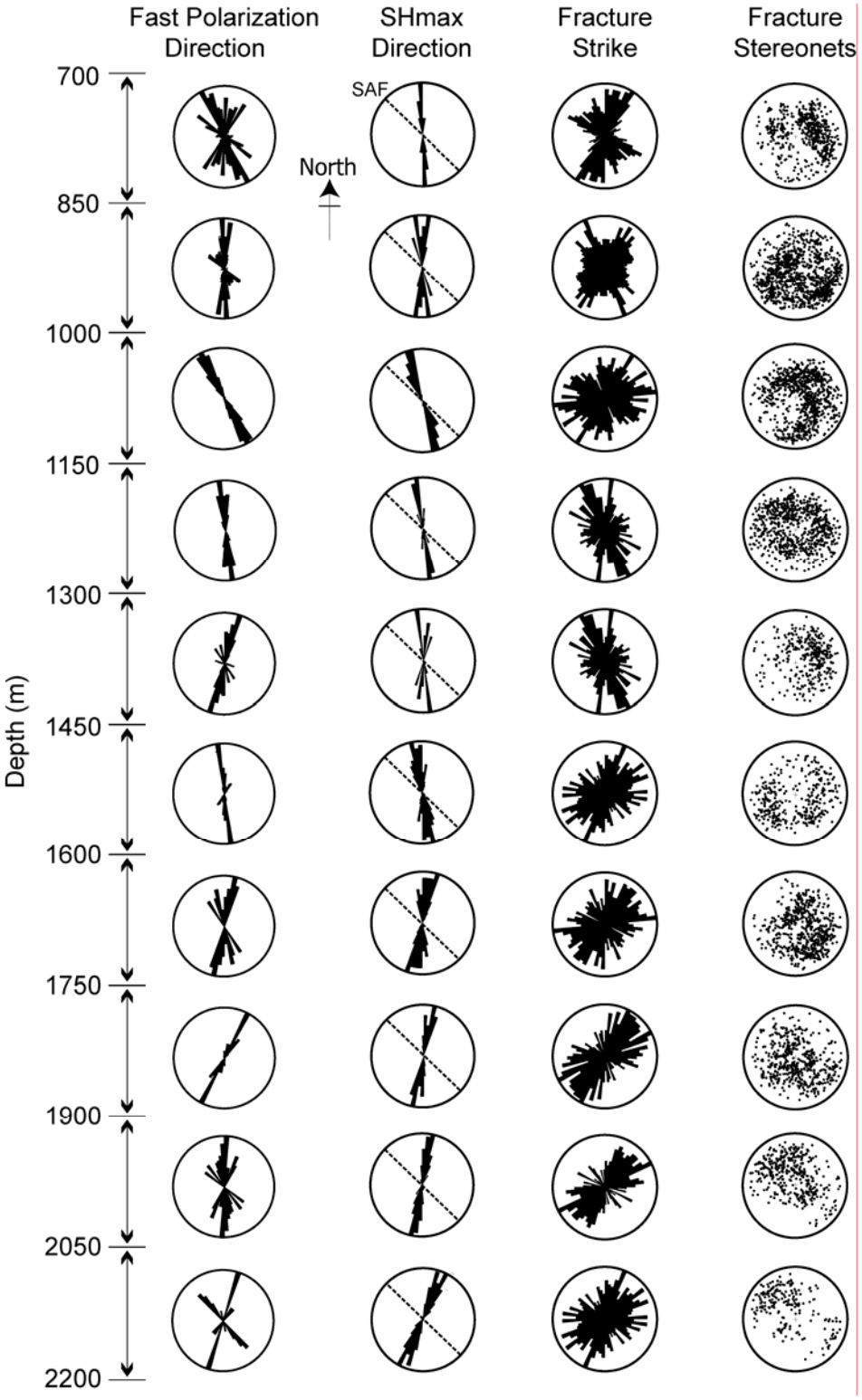

Figure 2.2: Comparison of the fast shear polarization direction with S_{Hmax} determined from borehole breakouts and tensile cracks [Hickman and Zoback, 2004] and fracture orientations as observed on the FMI log. The strike of the San Andreas Fault (SAF) is shown for reference. The direction of the fast shear direction correlates very well with the orientation of S_{Hmax} whereas the distribution of fractures shows little preferential orientation.

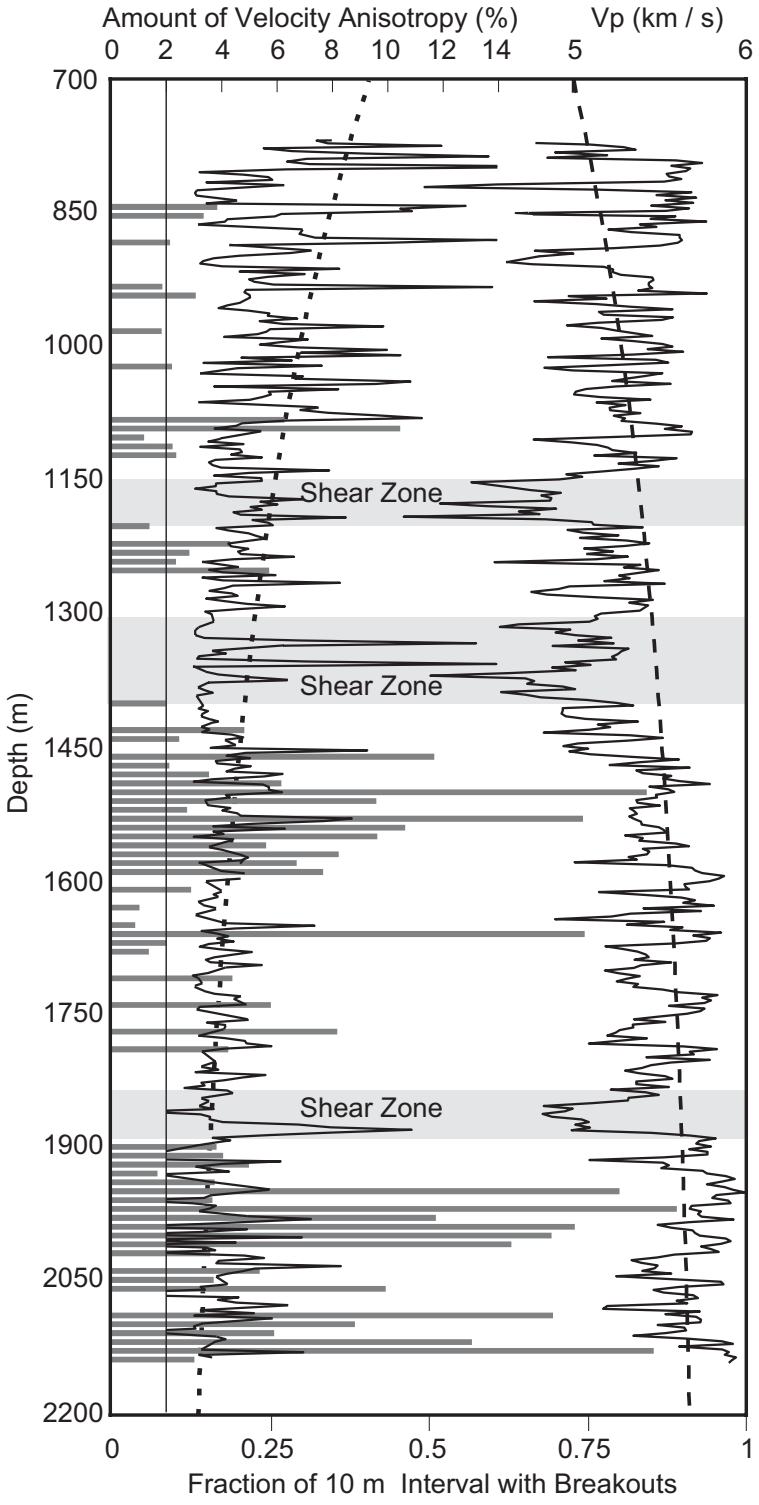

Figure 2.3: Fraction of the pilot hole with borehole breakouts shown as a bar graph with the amount of velocity anisotropy and P-wave sonic velocity superimposed. The highlighted shear zones are associated with high amounts of velocity anisotropy that correlate with an absence of borehole breakouts and low sonic velocity indicating the presence of stress relief zones.

There are five known causes of shear wave anisotropy in the crystalline crust [see reviews by Crampin et al., 1984; Crampin, 1987; Crampin and Lovell, 1991]: 1) Anisotropic in situ stresses cause the preferred closure of fractures at all scales in a highly fractured crust, thus generating a fast direction parallel to S_{Hmax}; 2) Dilatancy of stress aligned fluid-filled microcracks that also produce a fast direction aligned with S_{Hmax}; 3) Alignment of macroscopic fractures without stress effects; 4) The direct effect of an anisotropic stress field on the elastic properties of intact rock; and 5) Alignment of minerals or grains.

We observe highly variable orientations of macroscopic fractures and faults cutting across the pilot hole (Figure 2.2) that show no systematic relationship to either the fast polarization directions or S_{Hmax}. This leads us to believe that we can eliminate aligned macroscopic fractures as the cause of the shear wave anisotropy since the fast polarization directions show a consistent orientation (Figure 2.2). In direct contrast, the direction of maximum horizontal compression, S_{Hmax}, from stress-induced wellbore breakouts and drilling-induced tensile cracks [Hickman and Zoback, 2004] correlates very well with the fast polarization directions of the shear waves (Figure 2.2). Note the correlation of the fast polarization direction and S_{Hmax} at all depths: From 850–1000 m both the fast direction and S_{Hmax} are approximately north–south, from 1000–1600 m the orientations both rotate to slightly east of north and below a depth of 1600 m both the fast direction and S_{Hmax} are east of north.

Direct stress-induced anisotropy is improbable since the deviatoric stresses in the Earth are orders of magnitude smaller than those required to produce the observed amount of velocity anisotropy [Dahlen, 1972]. We also eliminate aligned minerals and grains as a cause of the observed anisotropy since the pilot hole cuttings showed no evidence of aligned minerals or grains.

The alignment of fluid-filled microcracks in response to the stress field, commonly known as Extensive Dilatancy Anisotropy (EDA) [Crampin et al., 1984; Crampin, 1987], is widely hypothesized as the cause of crustal shear wave anisotropy. However, note that the amount of velocity anisotropy increases in regions where breakouts are absent (Figure 2.3), whilst the fast directions remain consistent with

observations of S_{Hmax}. While the lack of borehole breakouts could be due to either high rock strength, or locally low differential stress, we observe that the sonic velocities are low in the regions without breakouts (Figure 2.3), indicating that the rock strength is not anomalously high in these intervals and that these are indeed stress relief zones [Hickman and Zoback, 2004]. The increase in velocity anisotropy in the intervals containing few breakouts probably results from an increase in the sensitivity of seismic velocity to stress at low mean stress magnitudes [Nur and Simmons, 1969] or an increase in microcracking [Moos and Zoback, 1983]. As the high anisotropy zones also correlate in depth with the intervals of the pilot hole interpreted as major shear zones from the petrophysical data, slip on faults within these zones [Hickman and Zoback, 2004] would explain both local stress drops and an increased amount of microcracking.

It should be noted that these observations are not consistent with EDA since microcrack dilatancy requires high differential stress that would promote breakout formation, contradictory to our observations in the inferred stress-relief zones. All things considered, the most viable model for the seismic anisotropy of the crust in this region is that the anisotropic stress field causes the preferred closure of fractures at all scales in a highly fractured crust. The decrease in the number of fractures with depth explains the decrease in the amount of velocity anisotropy.

2.4 Summary

Using geophysical logs from the SAFOD pilot hole we have characterized the variation of physical properties with depth within the Salinian granite. We find that P- and S-wave velocity and density increase with depth while the number of faults and fractures in the rock and shear wave velocity anisotropy decreases. There is an excellent correlation between the fast polarization direction of the shear waves and the direction of maximum horizontal compression as determined from borehole breakouts. We interpret three intervals of anomalous physical properties at depths of 1150–1200 m, 1310–1420 m and 1835–1880 m as major shear zones. These intervals are associated with anomalously low sonic velocities and high shear velocity anisotropy. The absence of breakouts in these intervals (even though the materials are almost certainly weaker than the surrounding rock) indicates locally lower stress anisotropy and/or stress magnitudes. The shear

velocity anisotropy appears to be caused by the preferential closure of fractures (either macroscopic or microscopic) in response to the stress field.

Acknowledgements

We are grateful to Daniel Moos and an anonymous reviewer for their critical reviews and valuable suggestions that improved this paper. This work was supported by National Science Foundation grant EAR 02-08493 and the International Continental Drilling Program

References

Barton, C. A., Zoback, M. D., and Moos, D., 1995, Fluid flow along potentially active faults in crystalline rock: *Geology*, **23**, 683-686.

Brace, W. F., 1971, Resistivity of saturated crustal rocks to 40 km based on laboratory measurements, in *The Structure and Physical Properties of the Earth's Crust*, pp. 243-255, AGU, Washington DC.

Brace, W. F., and Orange, A. S., 1968, Further studies of the effect of pressure on electrical resistivity of water saturated crystalline rocks: *J. Geophys. Res*., **73**, 5407.

Brace, W. F., Orange, A. S., and Madden, T. R., 1965, The effect of pressure on electrical resistivity of water saturated crystalline rocks: *J. Geophys. Res*., **70**, 5669-5678.

Catchings, R. D., et al., 2002, High-resolution seismic velocities and shallow structure of the San Andreas fault zone at Middle Mountain, Parkfield, California: *Bull. Seismol .Soc. Am*, **92**, 2493-2503.

Chen, S. T., 1988, Shear-wave logging with dipole sources: *Geophysics*, **53**, 659-667.

Crampin, S., Evans, R., and Atkinson, B. K., 1984, Earthquake prediction: a new physical basis: *Geophys. J. R. Astr. Soc*., **76**, 147-156.

Crampin, S., 1987, Geological and industrial implications of extensive-dilatancy anisotropy: *Nature*, **328**, 491-496.

Crampin, S., and Lovell, J. H., 1991, A decade of shear-wave splitting in the Earth's crust: what does it mean? what use can we make of it? and what should we do next?: *Geophys. J. Int*., **107**, 387-407.

Dahlen, F. A., 1972, Elastic velocity anisotropy in the presence of an anisotropic initial stress: *Bull. Seismol. Soc. Am*., **62**, 1183-1193.

Ekstrom, M. P., et al., 1987, Formation imaging with microelectrical scanning arrays: *The Log Analyst*, **28***,* 294-306.

Erzinger, J., Wiersberg, T., and Dahms, E., 2004, Real-time mud gas logging during drilling of the SAFOD Pilot Hole: *Geophys. Res. Lett*., **31**, L13S18.

Hickman, S., and Zoback, M. D., 2004, Stress orientations and magnitudes in the SAFOD Pilot Hole from observations of borehole failure: *Geophys. Res. Lett*., **31**, L15S12.

McPhee, D., Jachens, R., and Wentworth, C., 2004, Crustal structure across the San Andreas Fault at the SAFOD site from potential field and geologic studies: *Geophys. Res. Lett*., **31**, L12S03.

Moos, D., and Zoback, M. D., 1983, In situ studies of velocity in fractured crystalline rocks: *J. Geophys. Res*., **88**, 2345-2358.

Mueller, M. C., Boyd, A. J., and Esmeresoy, C., 1994, Case studies of the dipole shear anisotropy log: *SEG Expanded Abstracts*, **64**, 1143-1146.

Nur, A., and Simmons, G., 1969, Stress induced velocity anisotropy in rock: An experimental study: *J. Geophys. Res*., **74**, 6667-6674.

Palacky, G., 1987, Resistivity characteristics of geologic targets, in Naibighian, M. N., ed., Electromagnetic methods in applied geophysics: *Soc. Expl. Geophys*., Tulsa, Oklahoma, pp. 53.

Pezard, P., and Luthi, S. M., 1988, Borehole electrical images in the basement of the Cajon Pass scientific drillhole, California; Fracture identification and tectonic implication: *Geophys. Res. Lett*., **15**, 1017-1020.

Townend, J., and Zoback, M. D., 2000, How faulting keeps the crust strong: *Geology*, **28**, 399-402.

Unsworth, M. J., et al., 2000, Along strike variations in the electrical structure of the San Andreas Fault at Parkfield, California: *Geophys. Res. Lett*., **27**, 3021-3024.

Williams, C., Grubb, F., and Galanis, P., 2004, Heat Flow in the San Andreas Fault Observatory at Depth (SAFOD) Pilot Hole and Implications for the Strength of the San Andreas Fault: *Geophys. Res. Lett*., **31**, L15S14.

Zablocki, C. J., 1964, Electrical properties of serpentinite from Mayaguez, Puerto Rico, in A study of serpentinite: *Nat. Acad. Sci. Rep*, 107-11.

Chapter 3

Fine-scale controls on shear velocity anisotropy in the San Andreas Fault Observatory at Depth.

Abstract

We present an analysis of shear velocity anisotropy using data in and near the San Andreas Fault Observatory at Depth (SAFOD). We examine the physical mechanisms controlling velocity anisotropy and investigate the effects of frequency and scale. We analyze data from dipole sonic logs in both the SAFOD pilot hole and main hole and present the results from a shear wave splitting analysis performed on waveforms from microearthquakes recorded on a down-hole seismic array deployed in the pilot hole. We show how seismic anisotropy is linked either to structures such as sedimentary bedding planes or the state of stress, depending on the physical properties of the formation. For an arbitrarily oriented wellbore, we theoretically model the apparent fast direction that is measured with dipole sonic logs if the shear waves are polarized by arbitrarily dipping transversely isotropic structural planes (bedding/fractures). We show that when shear waves are polarized by the maximum compressive stress, the fast direction is equivalent to the azimuth of the maximum stress. Our results indicate that the contemporary state of stress is the dominant mechanism governing shear velocity anisotropy in both highly fractured and faulted granitic rocks and bedded arkosic sandstones. In contrast, within the more finely bedded shales, anisotropy is governed by the structural alignment of clays along the sedimentary

The material in this chapter has appeared in Boness, N. L., and Zoback, M. D., 2005, Fine scale controls on shear velocity anisotropy in the San Andreas Fault Observatory at Depth: *Geophysics*, submitted.

bedding planes. By analyzing shear velocity anisotropy at sonic wavelengths over scales of meters and at seismic frequencies over scales of several kilometers we show that the polarization of the shear waves and the amount of anisotropy recorded is strongly dependent on the frequency and scale of investigation. The shear anisotropy data also provides further constraints on the orientation of the maximum horizontal compressive stress and suggests that at a distance of only 100–300 m from the San Andreas Fault, the maximum horizontal stress is at an angle of approximately 70° to the strike of the fault. This observation is consistent with the hypothesis that the San Andreas Fault is a weak fault slipping at low levels of shear stress.

3.1 Introduction

Shear wave velocity anisotropy is commonly referred to as shear wave splitting because an isotropic shear wave traveling in an anisotropic medium separates into two quasi-shear waves. At a given receiver the quasi-shear waves are characterized by their orthogonal polarization directions (fast and slow directions) and a delay between their arrival times. There are numerous documented examples of shear wave anisotropy in the upper crust and various mechanisms have been proposed to explain these observations including: lithologic alignment of minerals/grains [e.g., Sayers, 1994; Johnston and Christensen, 1995; Hornby, 1998]; sedimentary bedding planes [e.g., Alford, 1986; Lynn and Thomsen, 1986; 1990; Willis et al., 1986]; aligned macroscopic fractures [e.g., Mueller, 1991; 1992; Meadows and Winterstein, 1994; Li et al., 1993]; extensive dilatancy anisotropy of microcracks [e.g., Crampin and Lovell, 1991]; and the preferential closure of fractures in rock with a quasi-random distribution of fractures due to an anisotropic stress field [Boness and Zoback, 2004]. These mechanisms can be divided into two major categories: 1) Stress-induced anisotropy in response to an anisotropic tectonic stress state (Figure 3.1b). This could arise in a medium in which there are aligned microcracks or the preferential closure of fractures in a randomly fractured crust. In this case, vertically propagating seismic waves will be polarized with a fast direction parallel to the open microcracks [Crampin, 1986], or perpendicular to the closed fractures [Boness and Zoback, 2004], in both cases parallel to the maximum horizontal compressive stress, S_{Hmax}; 2) Structural anisotropy due to the alignment of parallel planar features such as macroscopic fractures, parallel sedimentary bedding planes or the alignment of minerals/grains (Figure 3.1c). In this case the vertically propagating shear waves exhibit a fast polarization direction parallel to the strike of the structural fabric. In geophysical exploration, shear velocity anisotropy is commonly modeled with a transversely isotropic (T.I.) symmetry (Figure 3.1a) where the shear waves propagate in a direction perpendicular to the T.I. symmetry axis and are polarized parallel and perpendicular to the planes normal to the formation symmetry axis [Thomsen, 1986].

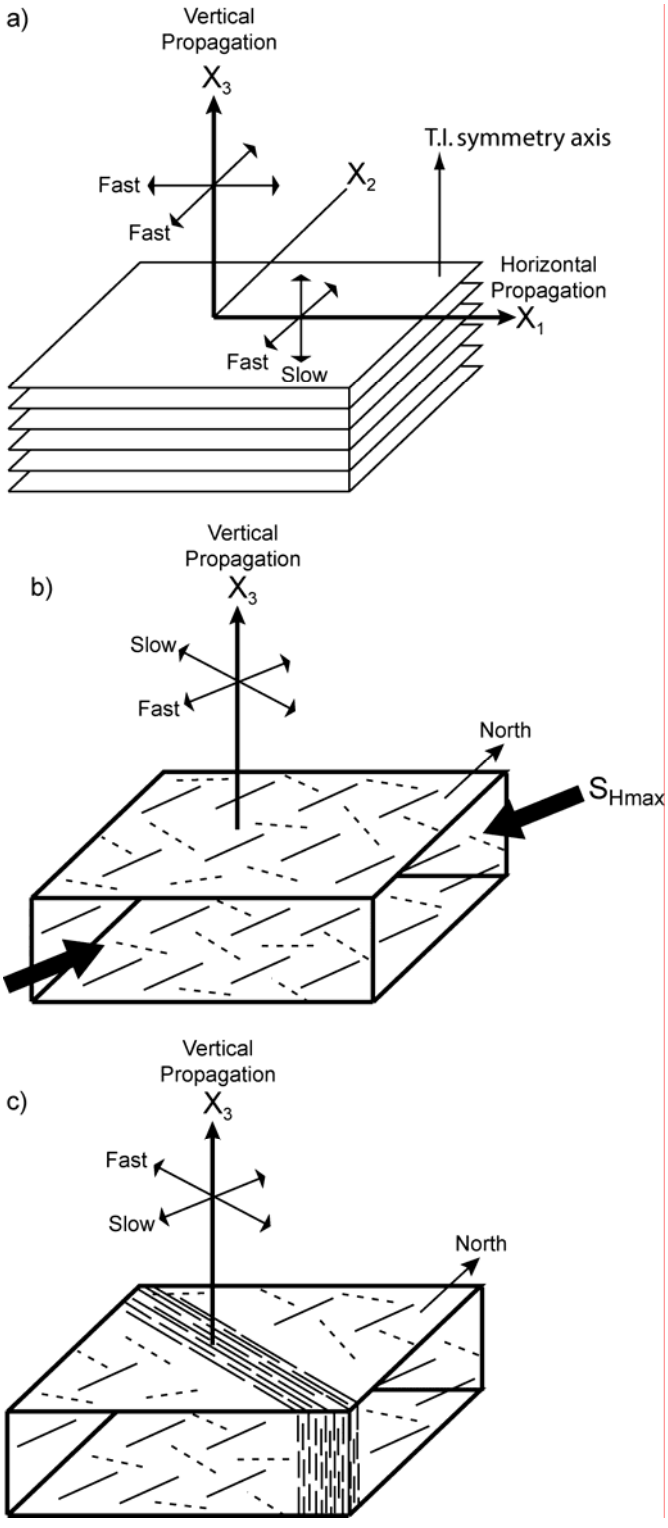

Figure 3.1: a) Transverse isotropy associated with horizontal bedding (vertical T.I. axis of symmetry) for vertically and horizontally propagating shear waves. b) Transverse isotropy in the context of stress-induced anisotropy due to the preferential closure of fractures in a randomly fractured crust and c) structural anisotropy due to aligned planar features such as the fabric within a major fault zone, sedimentary bedding planes or aligned minerals/grains.

Data from the San Andreas Fault Observatory at Depth (SAFOD) drilling project in Parkfield, California, provides the opportunity to study shear velocity anisotropy in the context of physical properties and stress conditions at a variety of scales. SAFOD consists of two boreholes: A vertical pilot hole was drilled in 2002 to a depth of 2200 m at a distance of 1.8 km southwest of the surface trace of the San Andreas Fault (SAF) and a main borehole (immediately adjacent to the pilot hole) drilled in 2004 and 2005. At the surface, the main borehole is only 7 m from the pilot hole. It remains essentially vertical to a depth of ~1500 m before deviating from vertical at an angle of 54° - 60° to the northeast toward the SAF (Figure 3.2) to a total vertical depth of 3000 m. A seismic array consisting of 25 three-component seismometers was installed in the pilot hole between depths of 800 m and 2000 m and recorded microearthquakes over a two year period from August 2002 to August 2004.

The structural fabric in the Parkfield region is clearly dominated by the northwest-southeast trend of the right-lateral, strike-slip SAF and associated sub-parallel strike-slip and reverse faults (Figure 3.3). Parkfield is located on the transition zone between the 300 km-long locked portion of the fault to the southeast that ruptured during the magnitude 7.9 Fort Tejon earthquake of 1857, and the creeping section to the northwest. The Parkfield segment of the SAF in central California is of particular interest because of seven historical magnitude six earthquakes [e.g., Roeloffs and Langbein, 1994], including the event which occurred in September 2004.

Regional *in situ* stress measurements indicating a direction of S_{Hmax} at a high angle to the SAF [Mount and Suppe, 1987; Zoback et al., 1987; Townend and Zoback, 2001; 2004] and the absence of a frictionally generated heat flow anomaly [Brune et al., 1969; Lachenbruch and Sass, 1980; Williams et al., 2004] indicate that the fault is a weak fault slipping at low shear stress. Measurements of stress orientation in the SAFOD pilot hole indicate that of S_{Hmax} rotates with depth to become nearly fault-normal at depth [Hickman and Zoback, 2004].

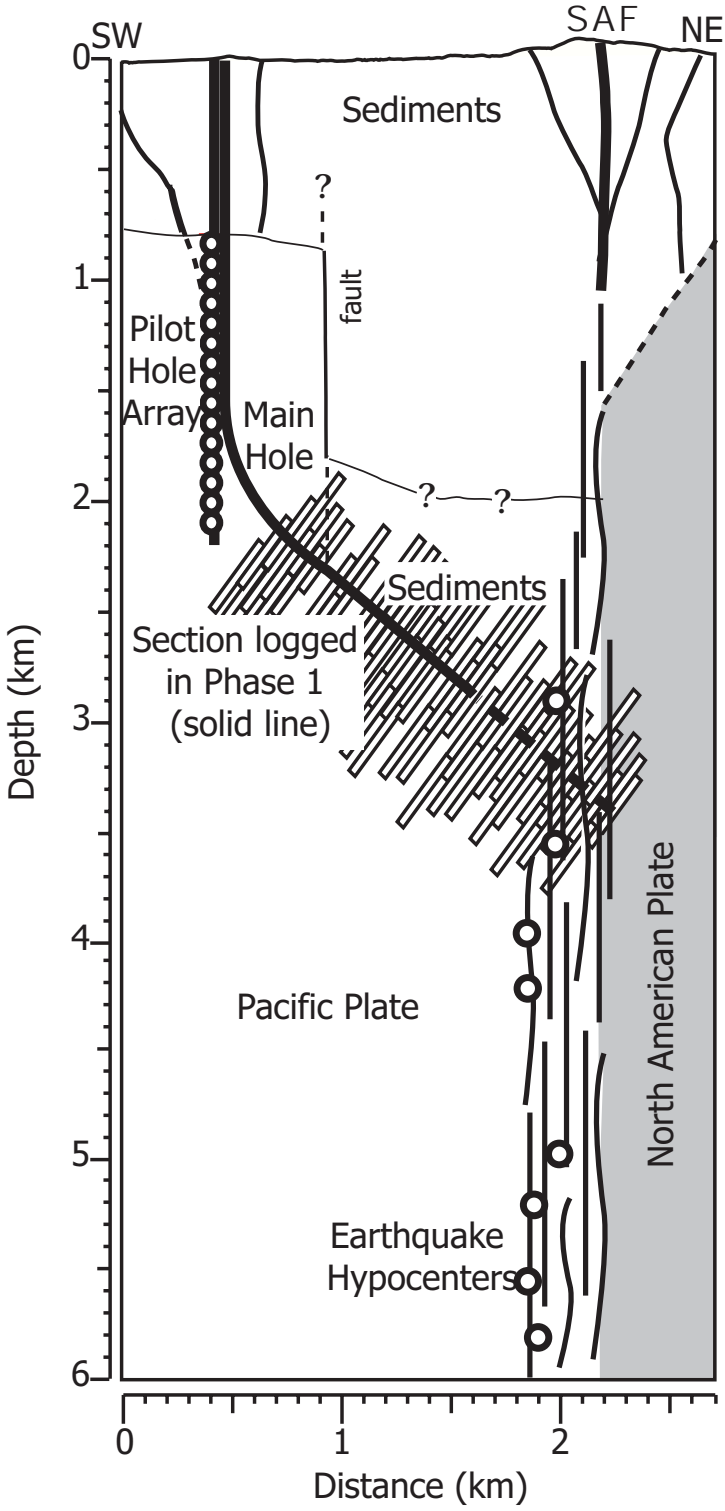

Figure 3.2: Scaled cartoon with the SAFOD main borehole and pilot hole array superimposed on the simplified geology of the North American and Pacific plates separated by the SAF, showing the section of the main borehole where geophysical logs were acquired. Please note the depth extent of the lower sedimentary sequence is unconstrained.

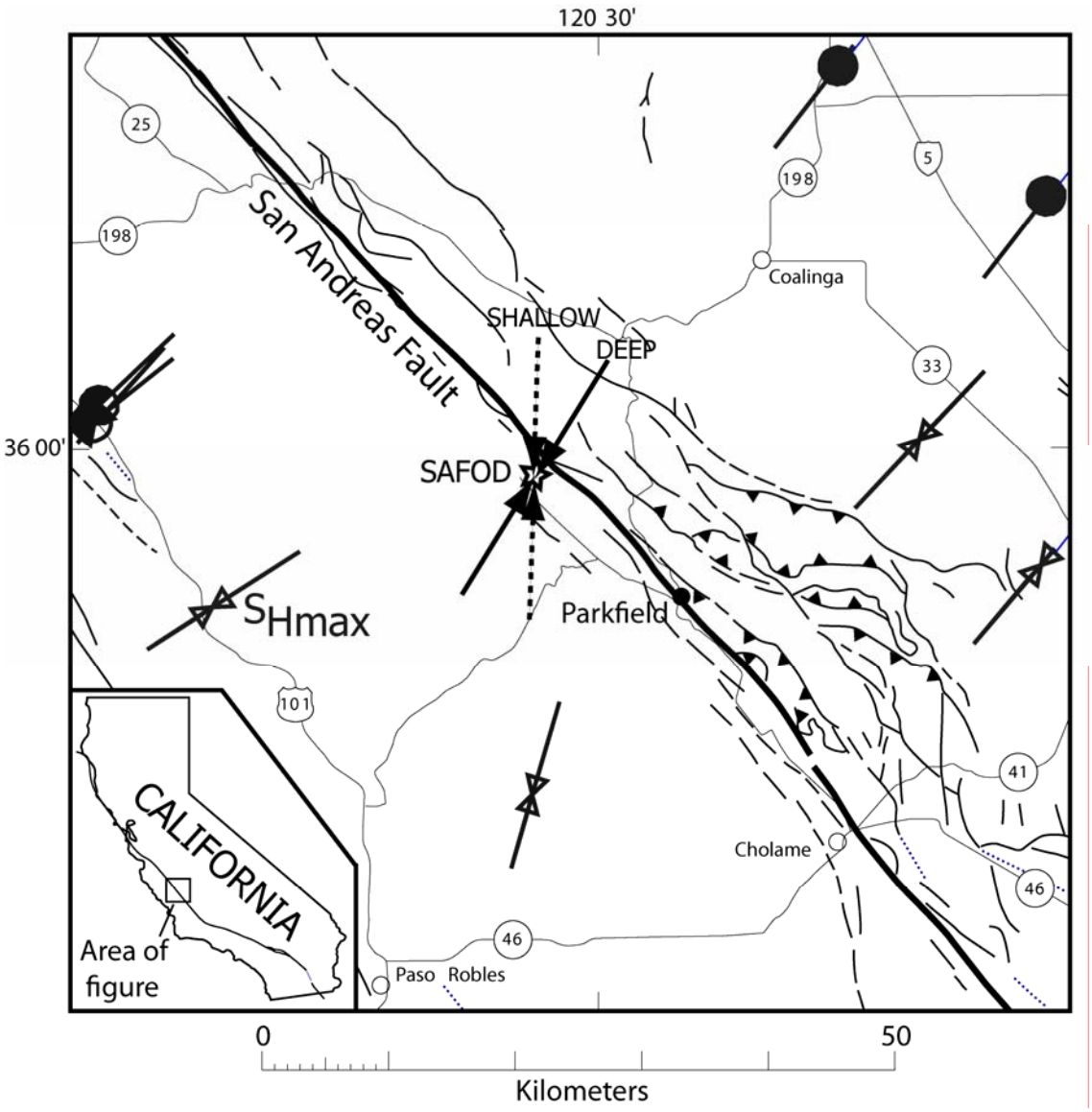

Figure 3.3: Map showing the location of SAFOD 1.8 km southwest of the SAF in central California. The orientation of the maximum horizontal compressive stress, S_{Hmax} (data from World Stress Map) is at a high angle to the northwest-southeast trend of the structural fabric. In the SAFOD pilot hole shallow and deep measurements of S_{Hmax} [Hickman and Zoback, 2004] indicate a clockwise rotation with depth to more fault-normal compression at a depth of ~2 km.

Parkfield is a good natural laboratory for studying the physical mechanisms controlling seismic velocity anisotropy because the northeast orientation of S_{Hmax} is at a high angle to the structural fabric (Figure 3.3), thus allowing us to distinguish between structural and stress-induced anisotropy in a manner similar to Zinke and Zoback [2000]. However, whereas Zinke and Zoback were restricted to microearthquake data recorded at single three-component seismometers at the surface, we also present observations of stress-induced seismic velocity anisotropy recorded at depth in the immediate proximity of the SAF. These data supplement previous stress measurements from borehole breakouts and focal mechanism inversions, providing further data on the strength of the SAF.

We are also interested in how observations of anisotropy at both sonic and seismic frequencies at different scales of investigation correlate with physical properties, lithology and the state of stress inferred from borehole measurements and regional geophysical studies. In particular, the frequency dependence of shear anisotropy may contain useful information regarding the scale of the heterogeneities polarizing the shear waves.

To investigate the fine-scale controls on shear wave velocity anisotropy we present an integrated analysis of dipole sonic logs in the pilot hole and phase 1 of SAFOD between a measured depth of 600 m and 3000 m. We correlate the sonic observations with a comprehensive suite of geophysical logs including sonic velocity, resistivity, gamma ray and porosity; an analysis of macroscopic fractures using the electrical conductivity image logs; and geologic analyses of cuttings/core. The sonic logs are investigating the anisotropy of the rocks at a scale of a few meters around the borehole but we also present shear wave splitting measurements at seismic wavelengths for nine microearthquakes recorded on the pilot hole array that are sampling a volume of the crust on the order of about eight cubic kilometers.

3.2 Lithology and physical properties

In this section we present an integrated analysis of data acquired in the SAFOD pilot hole and phase 1 of the main borehole to a measured depth of 3050 m. The data set includes petrophysical logs (Figure 3.4), electrical conductivity Formation Micro Imager (FMI) image logs (Figures 3.5 and 3.6) and thin section analysis of rock cuttings collected every 3 m during drilling. Real-time gas measurements [T. Wiersberg, personal communication, 2005] were used to identify hydraulically conductive intervals that could correspond to faults/fractures or more permeable sedimentary units. Note that all depths are measured depths along the borehole trajectory and referenced to the main hole kelly bushing at 10 m above the ground level (including data from the pilot hole).

Tertiary and Quaternary sediments were encountered to a depth of 780 m above granite and granodiorite, the expected basement rocks of the Salinian terrane west of the SAF. The vertical pilot hole (Figure 3.2) then remained in Salinian granite to a depth of 2200 m. However, after "kicking off" toward the SAF (Figure 3.2), the main borehole penetrated a major fault zone at 1920 m (230 m to the northeast of the kickoff from vertical), below which a sequence of sedimentary rocks was encountered. The sedimentary sequence mostly consists of packets of alternating sandstone and siltstone with intervals of finely laminated shale, some with conglomeritic clasts. A 12 m core sample was obtained at the bottom of phase 1 between depths of 3055 m and 3067 m and was composed of well-cemented arkosic sandstones and fine silt stones with numerous fractures and faults [J. Chester, personal communication, 2005].

The petrophysical logs (sonic velocity, resistivity, gamma ray, density and neutron porosity) were used to characterize the lithologic units penetrated by the main borehole. In the pilot hole, three major shear zones at 800 m, 1400 m, 1920 m and 2550 m were identified with anomalous physical properties: low sonic velocity, low resistivity, high natural radiation gamma ray, changes in porosity, increased fracturing on the FMI log and increased gas emissions [Boness and Zoback, 2004]. However, within the lower suite of sedimentary rocks in the main hole, it may be difficult to distinguish between shale units and shear zones from the geophysical logs as they could have very similar physical properties.

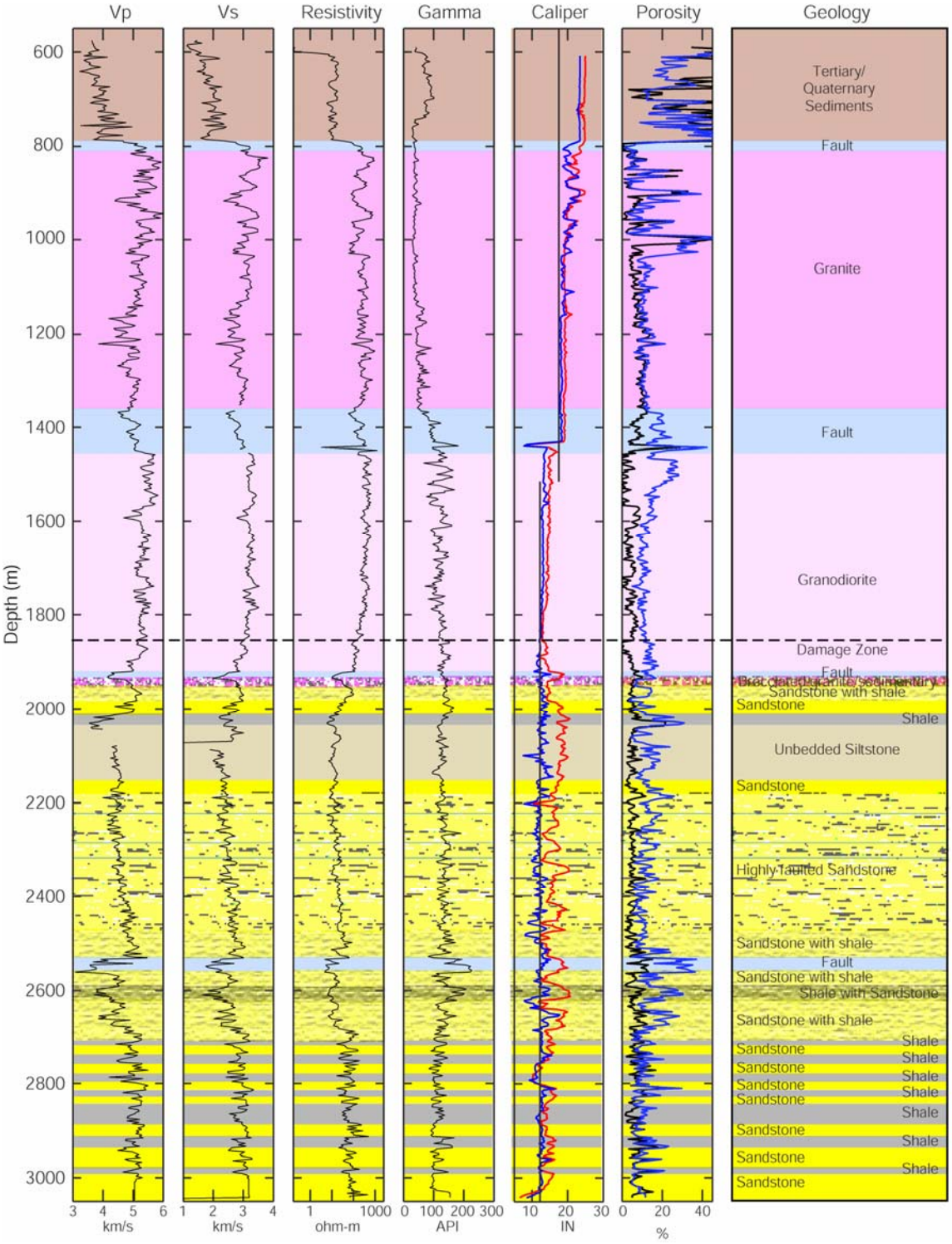

Figure 3.4: Petrophysical logs collected in the SAFOD main borehole. These were used in conjunction with electrical conductivity image logs, real-time gas observations and cuttings analysis to determine the lithologic profile shown in the right panel. The caliper has 4 arms, giving two orthogonal measurements of the borehole diameter. Two measurements of porosity are shown: density porosity (in black) determined from the density log using a reference grain density of 2.65 g/cm^3 and neutron porosity (in blue), which reflects the amount of free and bound water in the formation.

The upper granitic section of the SAFOD main hole is characterized by physical properties that are very similar to those reported in the pilot hole by Boness and Zoback [2004]. As shown in Figure 3.4, the compressional and shear sonic velocities (V_p and V_s) generally increase with depth, although there are many short-wavelength intervals of lower velocity associated with minor fractures. At the base of the granodiorite in the main borehole, both V_p and V_s show a marked decrease leading into the major fault located at 1920 m, probably indicating a fault damage zone. Overall, the resistivity increases from 10 Ohm-m in the Tertiary sediments to a maximum of 500 Ohm-m in the granodiorite. The resistivity decreases from 1800 m to 1920 m down to 90 Ohm-m, before showing a major decrease to 10 Ohm-m in the fault separating igneous and sedimentary units at 1920 m. The natural gamma shows an increase from about ~50 API in the granite to ~100 API in the granodiorite, probably reflecting the increase in felsic minerals like plagioclase feldspar.

Density and neutron porosity in the granite appears to be very high in some intervals from 820 m to 1050 m. We note, however, that the 4-arm caliper data indicates this section of the hole is washed out and we suggest these are erroneous measurements caused by hole enlargement in these intervals. Below 1050 m where the hole is in gauge, the density and neutron porosity are in agreement and indicate a porosity of about 10 %. Porosity measurements of a granite sample from the pilot hole reveal a matrix porosity of 1-2 %. We attribute the higher bulk porosities observed in the density and neutron porosity logs to the result of pervasive in situ macroscopic fractures and perhaps alteration zones that are not present in the small intact core sample. An analysis of the FMI logs in both the main hole and pilot hole (Figure 3.5) indicates an average fracture density of 30 fractures per 10 m. However, the number of fractures visible in the image logs from the main hole is approximately one third less than in the pilot hole due to poor image quality because the FMI tool has less coverage in the larger-diameter main hole. The rose diagrams of fracture strike illustrate the highly variable orientations of fractures and the lack of correlation with measurements of S_{Hmax} in the pilot hole. In addition, it should be noted that many of the fractures are low angle and the significance of these more ambiguous strike directions is over-represented by the rose diagrams.

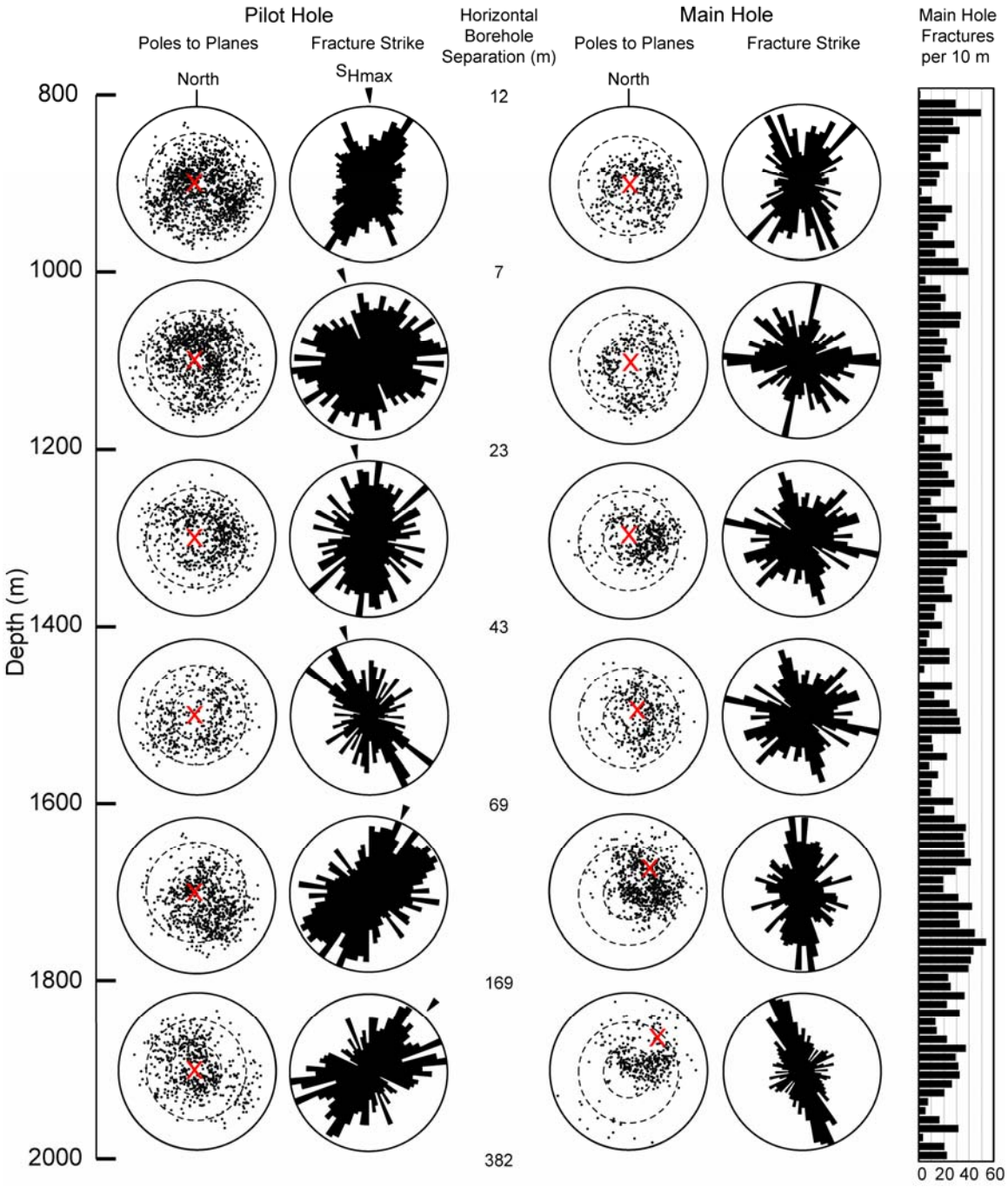

Figure 3.5: Lower hemisphere stereographic projections of poles to fractures and rose diagrams of fracture strike determined from the electrical conductivity image logs in the granitic section of both the pilot hole and main hole at 200 m intervals. The trajectories of the pilot hole and main hole are shown as red crosses on the stereonets and the dashed circles represent dips of 30° and 60° for reference. The measurements of S_{Hmax} in the pilot are also shown for reference as black triangles on the rose diagrams. The lateral distance between the boreholes at each depth is also shown. The histogram depicts the number of fractures per 10 m observed in the SAFOD main hole.

There is also a sampling bias due to the orientation of the borehole, which prohibits the observation of fractures that are parallel to the borehole trajectory. In the stereonets in Figure 3.5 this phenomenon is manifest by an absence in fracture poles in a halo 90° from the red crosses marking the average borehole trajectory within each interval.

In addition to the visual analysis of the fracture orientations using stereonets, we also use directional statistics designed to determine clusters of directional data in an objective way. Objective grouping of the data is performed by optimizing the mean pole vector that describes the fractures within each 200 m interval [Anderberg, 1973]. An orientation matrix is computed for each interval and the optimal orientation of the mean value is found by principal component analysis of the orientation matrix [e.g., Kiraly, 1969; Darot and Bouchez, 1976]. We compute the normalized maximum eigenvalue and corresponding eigenvector, which represents the "principal" direction of the fractures. The eigenvectors are described by a strike and dip which characterizes the properties of the fracture clusters within the interval. Eigenvalues range between 0 and 1, where 0 indicates complete statistical randomness of fracture orientations and 1 indicates that all fractures within the interval have exactly the same orientation. For the fractures intersected by the SAFOD boreholes, the maximum eigenvalues for each interval range between 0.2 and 0.56 indicating that there is limited preferential direction of the macroscopic fractures. The depth range with the most preferential orientation of fractures is between 1600 m and 2000 m fractures in the main hole, which show a fairly consistent north to northwest strike direction. However, the same interval in the pilot hole is only a lateral distance of less than 400 m away and does not show the same consistent pattern. Below 1500m the borehole trajectory is highly deviated and the lack of consistency between main hole orientations and the highly variable orientations in the pilot hole suggests a sampling bias due to the differing hole deviations. The sedimentary section was found to occur at a depth of 1920 m and we postulate that between 1800 m to 2000m some of the linear features in the FMI log interpreted to be fractures are actually sedimentary bedding planes explaining the degree of correlation in the strike direction.

The orientation of S_{Hmax} in the pilot hole as determined by Hickman and Zoback [2004] using wellbore breakouts and drilling-induced tensile fractures is also shown for

reference on the stereonets. Little consistent correlation between the fractures and stress orientation is observed [Boness and Zoback, 2004].

Below the granodiorite, the SAFOD main hole encountered a sedimentary sequence of rocks, consisting primarily of arkosic sandstones, shales and siltstones. In general, the sonic velocities within the sedimentary rocks that are only slightly lower than those measured within the granite above, with V_p between 4.2 km/s and 5.4 km/s and V_s between 2.2 km/s and 3.2 km/s and both showing an overall increasing trend with depth. Similarly, the resistivity shows an increase in the sedimentary rocks with depth.

The gamma ray in the sedimentary units is very similar to the measurements within the granodiorite and remains fairly high, which makes sense given the arkosic composition of the sandstones that are rich in potassium feldspar and the clay-rich shales. Within some fault zones (e.g., 2550 m) the gamma exhibits a local high perhaps due to an increase in clay content and enrichment of mobile radioactive elements (potassium, uranium, thorium). However, the major fault that juxtaposes granite and sedimentary rocks at 1920 m does not have a distinct gamma ray signature.

Porosity derived from density measurements is fairly consistent through the sedimentary section at about 10 %. However, the neutron porosity, which is sensitive to hydrous mineral phases in addition to free water, is much more variable and increases from a background level of ~10 % to a maximum of ~40 %. Although there are clear overall trends in all the physical properties with depth throughout the entire sedimentary sequence, we have identified a number of discrete sandstone and shale units that are characterized by obvious deviations from the average properties.

The sandstone units are characterized by higher velocities and resistivity, lower gamma radiation, and slightly lower density and neutron porosity than the other sedimentary units. An analysis of the cuttings samples in thin section reveals that these are arkosic sandstone units, composed of angular grains of granitic origin that have been well-cemented together [D. Moore, personal communication, 2005]. We discriminate bedding planes from fractures on the FMI by looking for intervals of very consistently striking and dipping planes that are regularly spaced. The orientation of bedding planes is shown on Figure 3.6.

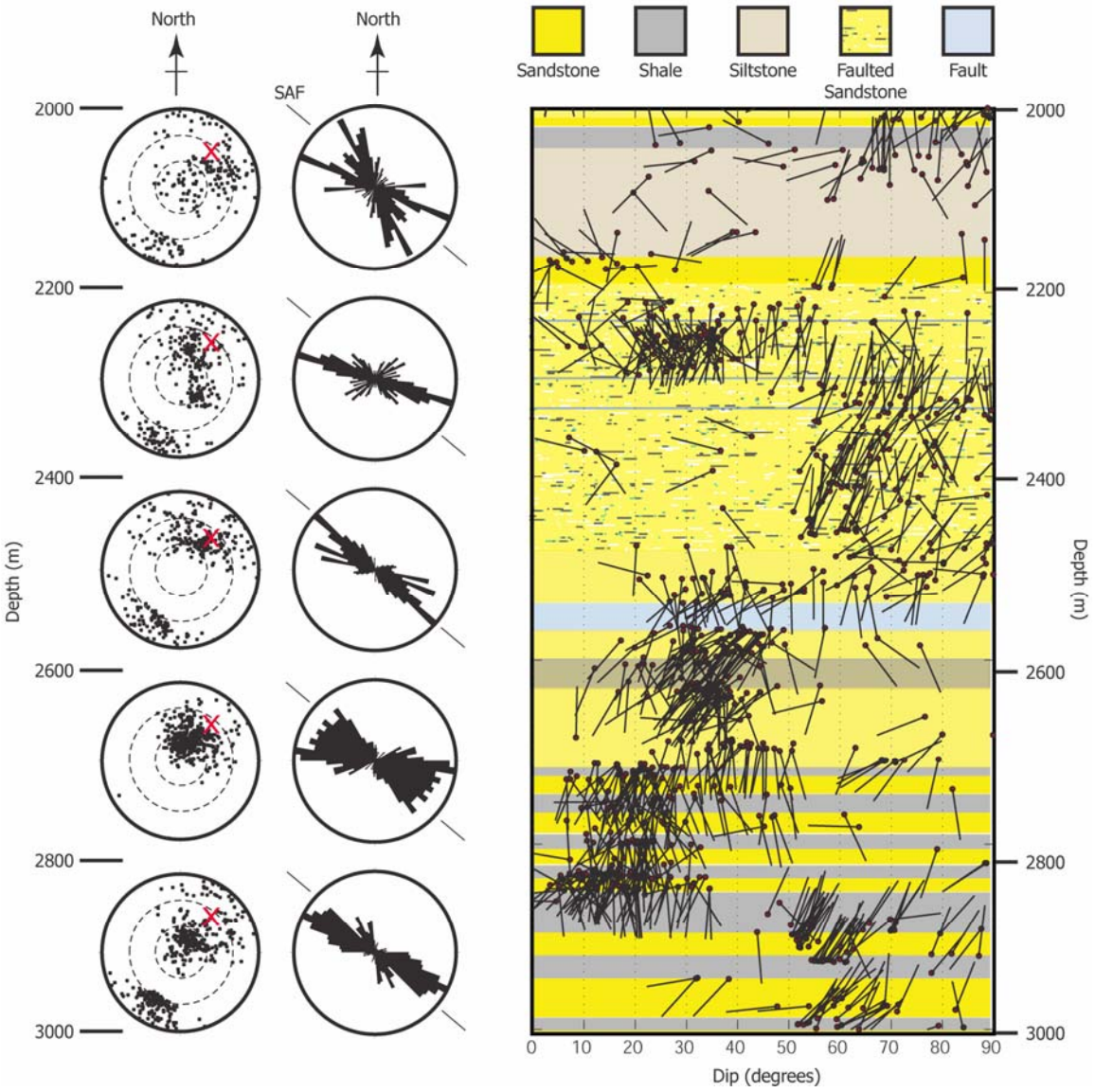

Figure 3.6: Bedding planes in the sedimentary sequence between 2000m and 3000 m in the main hole over 200 m intervals as determined from the electrical conductivity image logs. Stereonets show the poles to planes of all bedding planes within each interval and rose diagrams emphasize the strike of the beds. The average trajectory of SAFOD is shown with a red cross on the Stereonets and the strike of the SAF is shown on the rose diagrams for reference. A tadpole plot is overlain on the sedimentary lithology with a point indicating the dip of each bed and the tail pointing in the dip direction.

Within the sandstones, bedding planes are observed on the FMI image log at regularly spaced intervals of 0.5 m to 2 m. In contrast, there are many shale intervals that are associated with decreased velocity, decreased resistivity, increased gamma and increased neutron porosity. In these intervals, thin section analyses [D. Moore, personal communication, 2005] and X-ray diffraction analysis of the cuttings [J. Solum, personal communication, 2005] indicate an increase in clay minerals and sheared grains relative to the sandstones. The FMI image log reveals that these intervals are also characterized by a very conductive granular fabric with the presence of small resistive clasts. The bedding in these intervals is difficult to discern on the FMI image log amidst the conductive matrix but where it is visible it shows a much tighter spacing than the sandstone units, and may be better described as finely laminated (Figure 3.6). We interpret these intervals to be conglomeritic shale similar to the three Cretaceous debris flow deposits found in the Great Valley sequence in the general vicinity of Parkfield. The Juniper Ridge conglomerate is the uppermost of these channel-levee units and is found in outcrop slightly west of Coalinga, interbedded with thick-bedded sandstones, mudstones and shales [Hickson, 1999; Hickson and Lowe, 2002]. Although as noted above, we cannot rule out the possibility that some of these shale layers may be faults.

One other unit of interest is the siltstone found at a depth of ~2000 m. This siltstone is characterized by intermediate velocities and resistivity but is known from drilling to contain oxidized iron minerals causing it to be very red in color. The bedding in this interval, when visible in the FMI image log, is finely laminated, and reminiscent of the thin fine-grained muddy turbidites deposited in the Great Valley during periods of low sediment influx [Lowe, 1973].

In all the units, the bedding planes strike nearly parallel to the surface trace of the SAF and the majority dip away from the San Andreas to the southwest with an average dip of 39° (Figure 3.6), although there are increasingly more beds dipping to the northeast near the bottom of the borehole. The opposite sense of dip (to both the southwest and northeast) within different intervals of the sedimentary sequence may indicate folds associated with the transpressional nature of this tectonic region or faults

separating distinct blocks. It is relevant to note that the majority of observed bedding planes are essentially perpendicular to the borehole trajectory of SAFOD.

3.3 Shear anisotropy measured with dipole sonic shear logs

Data from open-hole dipole sonic shear logs are used to assess shear wave velocity anisotropy at sonic frequencies [Kimball and Marzetta, 1984; Chen, 1988; Harrison et al., 1990]. In the pilot hole a Dipole Sonic Shear Imager (DSI) log was acquired in 2002 and in the main borehole a Modular Sonic Imaging Platform (MSIP) log was obtained in 2004. The MSIP and DSI tools are multi-receiver tools with a linear array of 13 and 8 receiver stations respectively, spaced at 6" intervals [Schlumberger, 1995]. On the MSIP tool each receiver station consists of 8 azimuthal receivers and on the DSI there are 4 receivers, resulting in 104 and 52 waveforms, respectively, with which to compute shear velocity anisotropy. The transmitter on these dipole sonic tools is a low-frequency dipole source operating in the frequency range of 0.8 KHz to 5 KHz [Schlumberger, 1995]. A flexural wave propagates along the borehole wall that, in turn, directly excites shear waves with a depth of investigation of approximately 1.5 m into the formation.

We define the amount of velocity anisotropy as $100(V_{s1}-V_{s2}) / V_s$, where V_{s1} is the fast shear velocity, V_{s2} is the slow velocity and V_s is the mean shear velocity. We require that these data satisfy the following quality control measures to ensure that the dipole shear wave data is reliable: 1) velocity anisotropy greater than 2 %; 2) a difference in the energy of the fast and slow waves of more than 50 %; 3) a minimum energy of less than 15 % on the receiver in the slow direction after rotating the waveforms into the fast and slow directions.

Stress concentrations due to the presence of the borehole are expected to exist around the wellbore to distances of up to ~3 borehole radii [Jaeger and Cook, 1979]. The dispersive nature of the flexural wave (Figure 3.7) is used to filter out the high frequencies corresponding to short wavelengths that sample the rocks subjected to the stress concentration around the borehole [Sinha et al., 1994]. The observations presented here are thus shear velocities that correlate with low frequencies that penetrate deeper into the formation beyond the stress-perturbed zone around the wellbore.

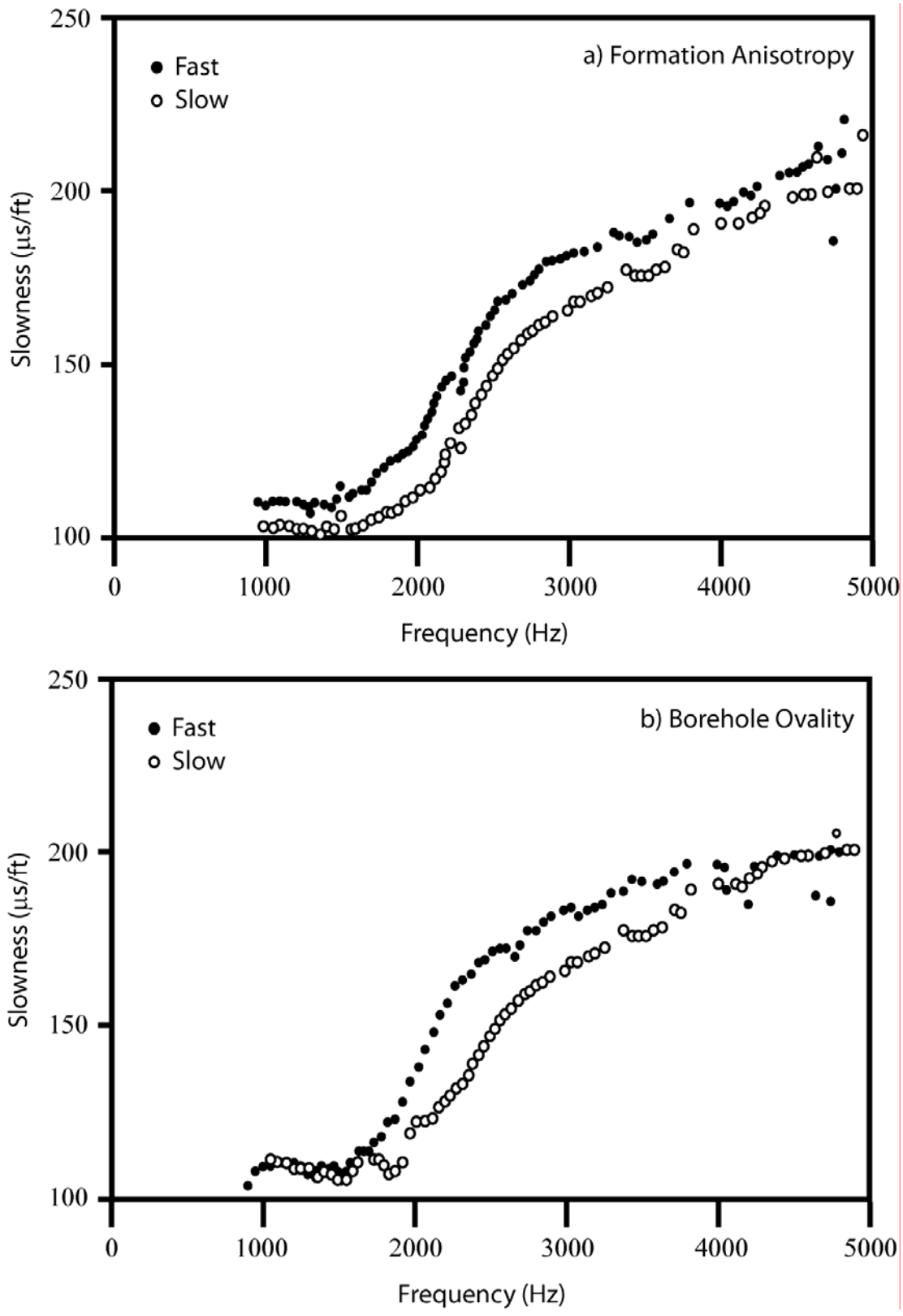

Figure 3.7: Example of dispersion curves for rotated waveforms used to distinguish between a) formation anisotropy and b) anisotropy caused by borehole ovality.

In addition, borehole ovality is known to bias the results of shear wave splitting analyses with dipole sonic logs [Leslie and Randall, 1990; Sinha and Kostek, 1996]. The dispersion curves of the rotated fast and slow waveforms exhibit a separation when shear velocity anisotropy is present. When the anisotropy is due to the formation it is present at all frequencies, which is reflected in parallel dispersion curves (Figure 3.7a). However, when there is apparent anisotropy due to borehole ovality the dispersion curves show a significant separation at mid-range frequencies but are identical at both low and high frequencies (Figure 3.7b). In theory, the lack of separation between the shear velocities at low frequencies means that anisotropy due to borehole ovality would automatically be removed in the quality control procedure described above. However, when the borehole is enlarged, the shear velocity at low-frequencies is not always well constrained. We analyze the dispersion curves at every depth interval and remove all data from depth intervals which exhibit separation at mid-range frequencies but not at high frequencies, the characteristic dispersion in the case of borehole ovality.

The geometry of the dipole sonic tools is best suited for investigating T.I. formations when the borehole is perpendicular to the axis of symmetry (Figure 3.1), e.g., parallel to the bedding planes. The shear waves generated and received by the dipole sonic tools are recorded in the planes normal to the axis of the borehole. Thus, the minimum and maximum shear velocities observed (and used to compute the amount of anisotropy) are not necessarily the absolute minimum and maximum velocities in the Earth, which may lie in planes that are not perpendicular to the borehole axis. We define the true fast direction as the orientation in the Earth with the absolute fastest shear velocity (a series of parallel planes described by a dip and dip direction) and the apparent fast direction as the fastest direction in a plane perpendicular to the borehole.

Sinha et al. [1994] modeled elastic wave propagation in a borehole with an axis at a range of angles to the formation symmetry axis. They demonstrated how the amount of anisotropy varies as the borehole becomes more oblique to the symmetry axis of the formation and that the maximum anisotropy is recorded at a 90° angle to that axis. The geometry of the borehole relative to the formation will not only dictate the amount of anisotropy observed but also the apparent fast direction that is recorded by the tool.

Figure 3.1a illustrates the case when the borehole (and thus shear wave propagation) is either parallel or perpendicular to the T.I. axis of symmetry. However, in reality it is probable that the borehole will be at some oblique angle to the symmetry axis (Figure 3.8a) and more generally, that neither the borehole nor the formation will be aligned with the vertical and horizontal coordinate axes (Figure 3.8b).

3.4 Modeling shear anisotropy in an arbitrarily oriented borehole

We present a three-dimensional model for computing the apparent fast direction that will be recorded on the dipole sonic tools for any arbitrary orientation of the borehole in a T.I. formation. Figure 3.9 shows the geometry used in our model. In the case of stress-induced anisotropy, the true fast direction is parallel to the maximum compressive stress, oriented across the closed fractures. Unless the borehole is oriented exactly along the T.I. symmetry axis, the apparent fast direction is described by a unique line that lies within the plane normal to the borehole, in the direction normal to the fracture opening direction. Since SAFOD is in a strike-slip/reverse stress state we expect the maximum compressive stress to be horizontal and thus the fastest shear velocity will be described by an azimuth in the horizontal plane. The apparent fast direction is the vertical projection of the maximum compressive stress on the plane perpendicular to the borehole and will have the same azimuth as S_{Hmax} (Figure 3.9b), with a dip that depends on the orientation of the borehole. In the case of structural anisotropy, the true fast direction is oriented along the planes (be they fractures/bedding/aligned minerals) and the dip of the fast direction in the plane will be dependant on the propagation direction of the shear waves. However, the apparent fast direction has to be in the plane perpendicular to the borehole. Therefore, the apparent fast direction that is observed with the sonic tool will be an azimuth that lies in both the true fast plane and the plane normal to the borehole, i.e. a line that marks the intersection of both planes (Figure 3.9c). Our formalism allows one to either determine the true fast direction in the Earth given an observed apparent fast direction or if the formation geometry is known one can predict the apparent fast direction that will be recorded by the dipole sonic tool for the assumed T.I. formation.

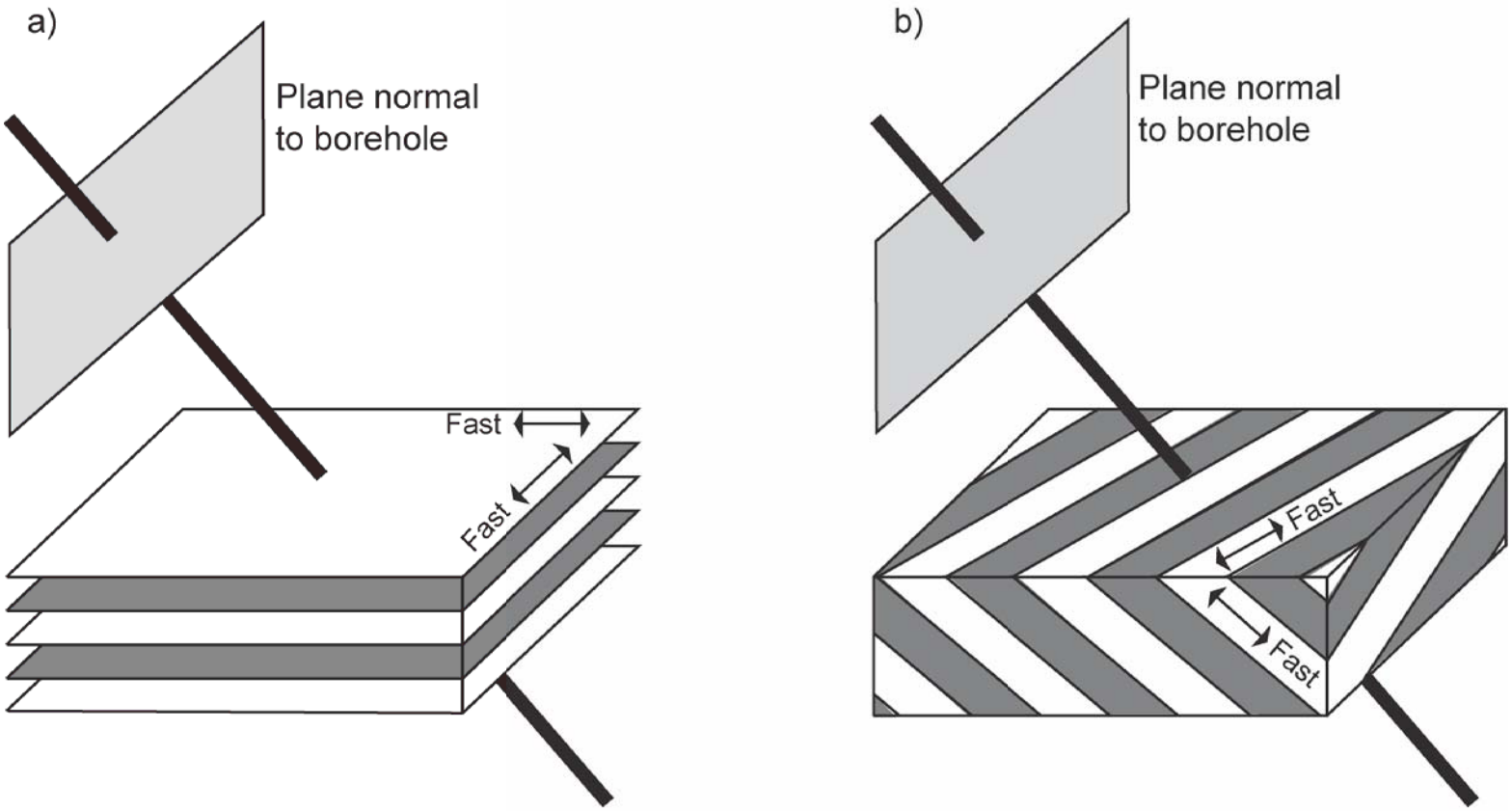

Figure 3.8: a) Geometry of a borehole at an oblique angle to a vertically transverse formation and b) the general case when a borehole is oblique to a formation with a symmetry axis that is not aligned with one of the Cartesian coordinate axes.

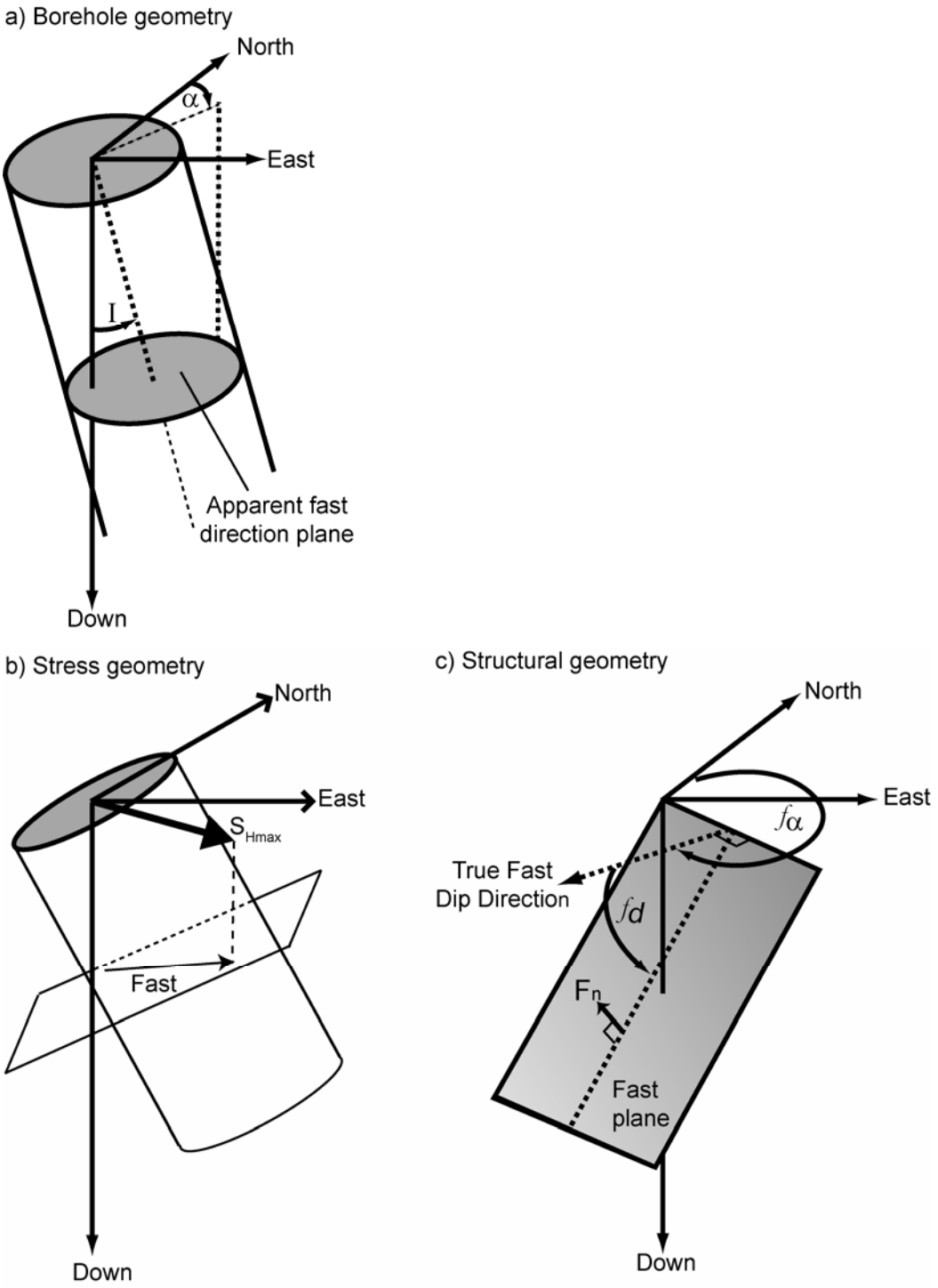

Figure 3.9: a) Figure illustrating the geometry of the borehole with the plane in which the apparent fast direction is measured with the sonic logs. b) In the case of stress-induced anisotropy, the apparent fast direction in the plane perpendicular to the borehole has an azimuth equivalent to that of S_{Hmax}, although the dip depends on the borehole trajectory. c) Geometry used to compute the apparent fast direction that will be observed on the dipole sonic tool for structural anisotropy when the fast direction lies in an arbitrarily oriented plane.

As shown in Figure 3.9a, for a borehole with azimuth from North, α, and inclination from the vertical, I, the vector, B_n that defines the axis of the borehole from an arbitrary origin is given by:

$$B_n = \left[\sin(\alpha)\sqrt{1+\left(\sin\left(\frac{\pi}{2}-I\right)\right)^2} \quad \cos(\alpha)\sqrt{1+\left(\sin\left(\frac{\pi}{2}-I\right)\right)^2} \quad -\sin\left(\frac{\pi}{2}-I\right) \right], \qquad (1)$$

where all angles are in radians. Given the dip, f_d, and dip direction, f_α, of the true fast plane we compute three discrete points, F_1, F_2 and F_3, in the fast plane that has a corner at the origin used to define the borehole. The normal to the fast plane, F_n, may now be computed using $A = F_1 - F_2$ and $B = F_2 - F_3$, thus giving $F_n = A \times B$. The vector, f^a, that describes the apparent fast direction, f^a_d (defined to be in the dip direction), and the apparent fast dip, f^a_α, from the origin is then found by computing the line that is perpendicular to the borehole and perpendicular to the normal to the fast plane (i.e. in the fast plane) such that $f^a = B_n \times F_n$.

Figure 3.10 shows the results of this computation for the arbitrary case of a well with an azimuth of 45° (i.e. northeast) deviated at 45°. We show the apparent fast direction and dip that will be measured in the borehole for true fast directions dipping to the north, east, south and west (i.e., 0°, 90°, 180° and 270°) over a range of true fast dip angles from horizontal to vertical (i.e., 0° to 90°). Typically the azimuth of the fast direction is reported (as a direction between -90° west and 90° east) but the dip of the fast direction is omitted as only a vertical T.I. symmetry is considered. However, given the orientation of the borehole the dip of the apparent fast direction can easily be computed as the observed azimuth lies in a plane normal to the borehole. For completeness we present both the azimuth (as an angle between -180° and 180° in the direction of dip) and the dip of the apparent fast direction. We also show that the dip of the fast azimuth provides valuable information about the true orientation of the fast direction within the formation.

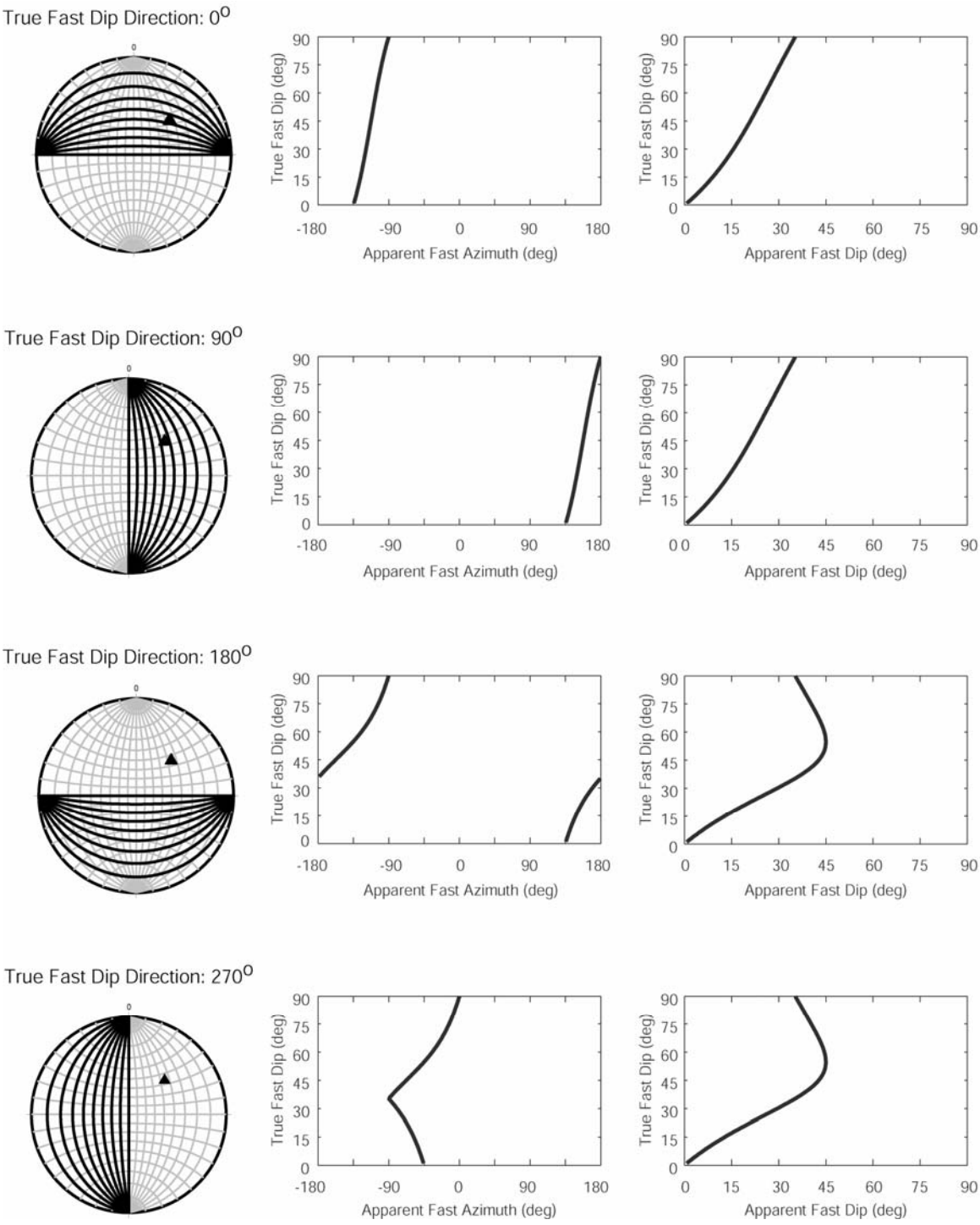

Figure 3.10: Model results for the arbitrary case of a borehole with an azimuth of 45° deviated at 45° (shown as a triangle on the stereonets), for four true fast dip directions of 0°, 90°, 180° and 270°, at a full range of dips from 0-90° (shown as great circles).

Figure 3.10 illustrates the strong dependence that the relative geometry of the borehole and true fast direction (shown here as a bedding plane) has on the apparent fast direction. In this example with a northeast trending borehole, one can see that if the beds dip to the north the apparent fast direction will be southwest. However, if the beds dip to the east, the apparent fast direction is southeast. It should be noted that when the bedding planes are either close to horizontal or vertical the true fast direction is hard to determine from the apparent fast direction. Otherwise, the results from this modeling indicate that the true fast directions will give rise to a unique apparent fast direction in the borehole.

For this borehole trajectory, the dip of the true fast direction (or bedding planes) has the biggest effect on the apparent fast direction when the beds are dipping to the south and west, i.e. away from the direction of penetration. The true fast direction is most closely approximated by the apparent fast direction when the formation axis is close to being perpendicular to the borehole. This corresponds to the results of Sinha et al. [1994] showing the amount of anisotropy will also be at a maximum when the formation axis is normal to the borehole.

3.5 Dipole shear anisotropy in SAFOD

3.5.1 Data Analysis

After applying the quality control measures described in Section 3.3 to the dipole sonic data collected in the SAFOD boreholes, we compute the mean fast direction of the shear waves over 3 m intervals. We choose Bingham statistics [Fischer, 1987] because the fast directions are unit vectors. The normalized eigenvalues give a measure of the relative concentration of orientations about the mean and we discard any mean fast direction over a 3 m interval with a normalized eigenvalue of less than 0.9.

The upper section of the main hole essentially overlaps with the pilot hole and we choose to use the seismic velocity anisotropy results from the pilot hole within this depth interval as the borehole is smaller and has fewer washouts so the sonic tool was better centered within the hole. However, a comparison of both logs indicates a high level of repeatability. The combined dipole sonic anisotropy results from both holes are shown in Figure 3.11.

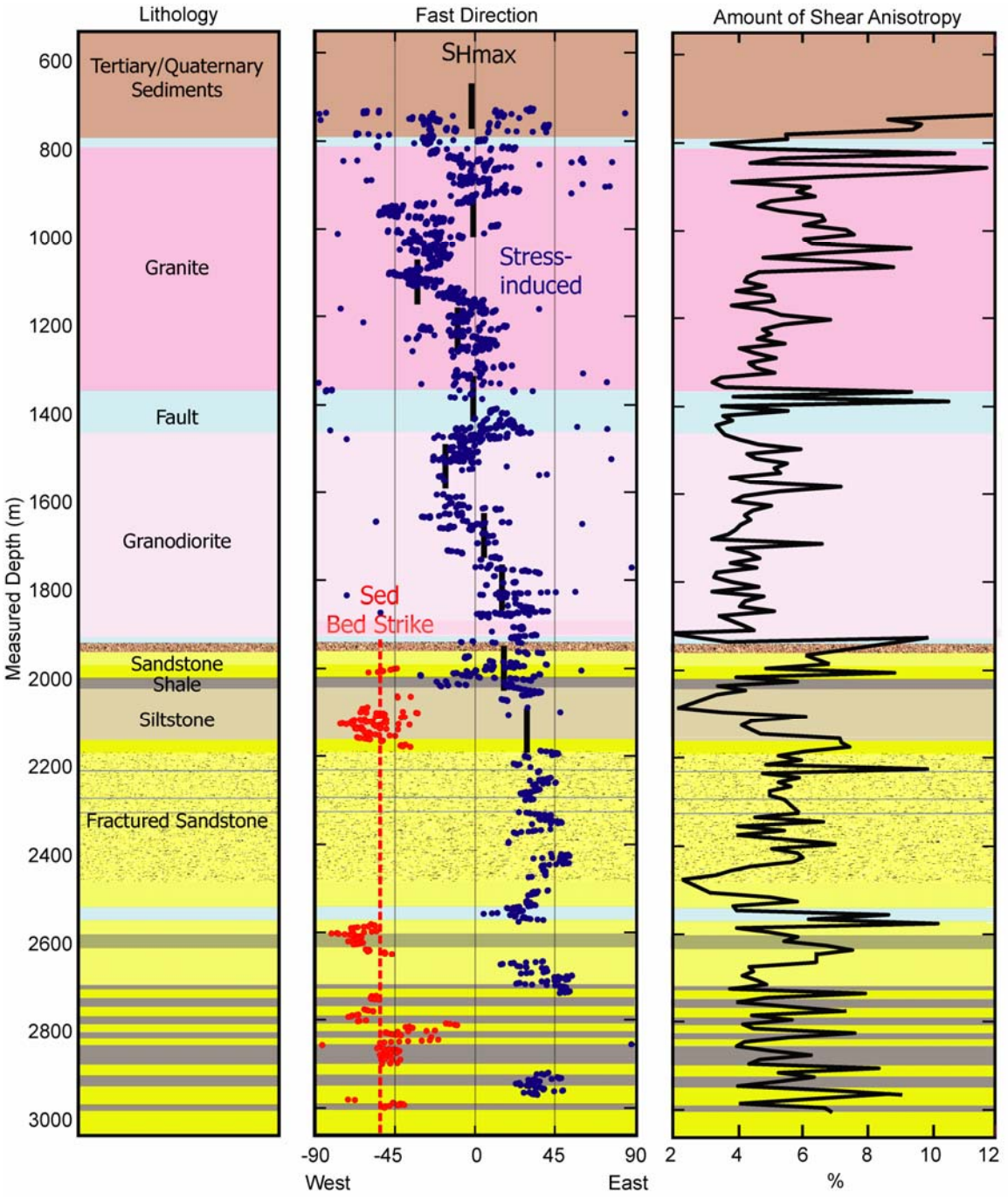

Figure 3.11: Observations of shear velocity anisotropy from the dipole sonic logs in the pilot hole and main hole. Anisotropy inferred to be stress-induced and structurally controlled is shown as blue and red dots, respectively. The direction of the sedimentary bedding planes, shown as a red dashed line, is the mean strike determined in the electrical conductivity image. The black bars in the middle plot indicate the orientation of S_{Hmax} in the pilot hole determined by Hickman and Zoback [2004].

Within the granite, from 760 m to 1920 m, the fast polarization direction of the shear waves is approximately north-south and exhibits a rotation to a more northeasterly direction with depth. The amount of anisotropy is observed to decrease from about 10 % at the top of the granite to approximately 3 % at the bottom of the granodiorite. There are three distinct intervals within the granite where the amount of anisotropy is observed to increase by up to 10 % above the overall trend in both the pilot hole and the main borehole. The depths of these intervals in the pilot hole were reported by Boness and Zoback [2004] to be 1150-1200 m, 1310-1420 m and 1835-1880 m. In the main borehole we observe increases in the amount of anisotropy at 1050-1100, 1360-1455 m and at the granodiorite-sediment interface at 1920 m. It is relevant to note that in both the pilot hole and main borehole the fast polarization direction within these intervals remains consistent with the fast direction throughout the rest of the granite even though the amount of anisotropy increases.

Above a depth of 1920 m in both the pilot hole and main hole the faults and fractures observed on the image logs show highly variable orientations (Figure 3.5). However, the direction of S_{Hmax} from a wellbore failure analysis in the pilot hole [Hickman and Zoback, 2004] as shown in Figure 3.11 illustrates the remarkable correlation between fast polarization direction and stress within the granitic section. The seismic anisotropy is interpreted to be stress-induced, caused by the preferential closure of fractures in response to an anisotropic stress state [Boness and Zoback, 2004]. Further evidence for stress-induced anisotropy is that the amount of velocity anisotropy decreases with depth in the granite section of the borehole from approximately 10 % at 780 m to 3 % at 1920 m (Figure 3.11). We interpret this decrease to be the result of increasing confining pressure with depth that tends to close fractures in all orientations and thus make velocity anisotropy less stress sensitive at higher pressure [e.g., Nur and Simmons, 1969].

The zones in the granite where the amount of anisotropy in the sonic log increases by up to 10 % above the overall trend correlate with intervals of anomalous physical properties (e.g., low sonic velocity, low resistivity, high gamma ray, increased fracturing). As discussed in detail by Boness and Zoback [2004], these intervals are intensely fractured but do not exhibit borehole breakouts, which is curious considering

that the low velocity would imply lower rock strength. These intervals are interpreted to be shear zones with low shear stress [Boness and Zoback, 2004] probably resulting from past slip events on faults. The high amounts of velocity anisotropy within the shear zones are inferred to be either because of the increased sensitivity of seismic velocity to stress at low mean stress [e.g., Nur and Simmons, 1969] or enhanced microcracking [Moos and Zoback, 1983]. The fact that the fast shear waves are polarized parallel to the stress in the shear zones leads us to believe this is not structural anisotropy but instead directly related to perturbations in the stress state. It is well known that fault zones are often associated with a rotation of S_{Hmax} and a localized absence of breakouts [Shamir and Zoback, 1992; Barton and Zoback, 1994] and interestingly we observe westerly rotations in the fast direction of the shear waves over depth intervals of approximately 100 m just below the major shear zones at 800 m, 1400 m, and 1920 m. It is interesting that the rotation in fast directions is below the shear zones, whereas the gradual change in physical properties that we interpret to be a damage zone appears to lead into the shear zones from above.

At the transition from granite to sedimentary lithology at 1920 m, Figure 3.11 illustrates that the amount of velocity anisotropy significantly increases again to an average value of about 6% and then remains approximately constant to the bottom of the hole but with a number of fluctuations on the order of ± 2 %. Within the sedimentary section (1920 m to 3000 m) there are two trends in the fast polarization directions of the shear waves: a northwest orientation and a northeast orientation consistent with the gradual eastward rotation in the fast directions in the granitic upper section. In the following sections, we correlate the fast polarization directions with lithology and petrophysical properties and propose that both stress and lithologic structure are dominant controls on the anisotropy we observe.

3.5.2 Application of modeling to SAFOD dipole sonic data

To further our understanding of the structural anisotropy within the sedimentary section we forward model the fast shear directions due to the observed bedding planes in the FMI log and compare these to the fast directions observed in the dipole sonic data. We consider the FMI log from 2000 m to 3000 m in discrete intervals of 10 m and

compute the mean bed orientation (dip direction and strike) using Fisher vector distribution statistics [Fisher et al., 1987]. We discard all intervals with less than four beds or with a normalized mean eigenvalue of less than 0.9. After computing the mean bed orientations, we use the theoretical formulation presented above to compute the apparent fast direction for each discrete 10 m interval that would be observed in the SAFOD borehole if the shear waves were being polarized with a fast direction parallel to the bedding planes. Between 2000 m and 3000 m the borehole has an average azimuth and deviation from vertical of 35° and 54°, respectively, but a gyroscopic survey is used to input the exact borehole azimuth and inclination at each depth interval. In Figure 3.12 we show the number of bedding planes used to compute the mean orientation and compare the theoretical apparent fast direction with the fast direction observed on the dipole sonic tool.

In most of the finely laminated, clay-rich shale and siltstone units below 2550 m and the weaker, faulted sandstones that also contain a lot of clay, the northwest fast direction of the sonic shear waves generally correlates well with the theoretical fast directions for structural anisotropy. One notable exception occurs at a depth of ~2900 m, where the theoretical model predicts northeast fast directions but the averaged data indicates a northwest observed fast direction. This may be because many of the bedding planes in this interval are very low angle (Figure 3.6) and, as described in Section 3.4, this makes the theoretical fast directions harder to constrain. We interpret the seismic anisotropy within most of these finely bedded stratigraphic layers to be controlled by the alignment of clay and mica platelets in the strike direction of the bedding planes.

Within the well-cemented (high seismic velocity), massively bedded sandstones (2170 m to 2550 m), Figure 3.12 shows that the sonic log exhibits a northeast fast polarization direction consistent with observations in the granite at shallower depths. However, the theoretical fast directions computed from the bedding planes show a lot of scatter due to the highly variable nature of the bed orientations (Figure 3.6), and do not show a good correlation with the consistent dipole sonic observations.

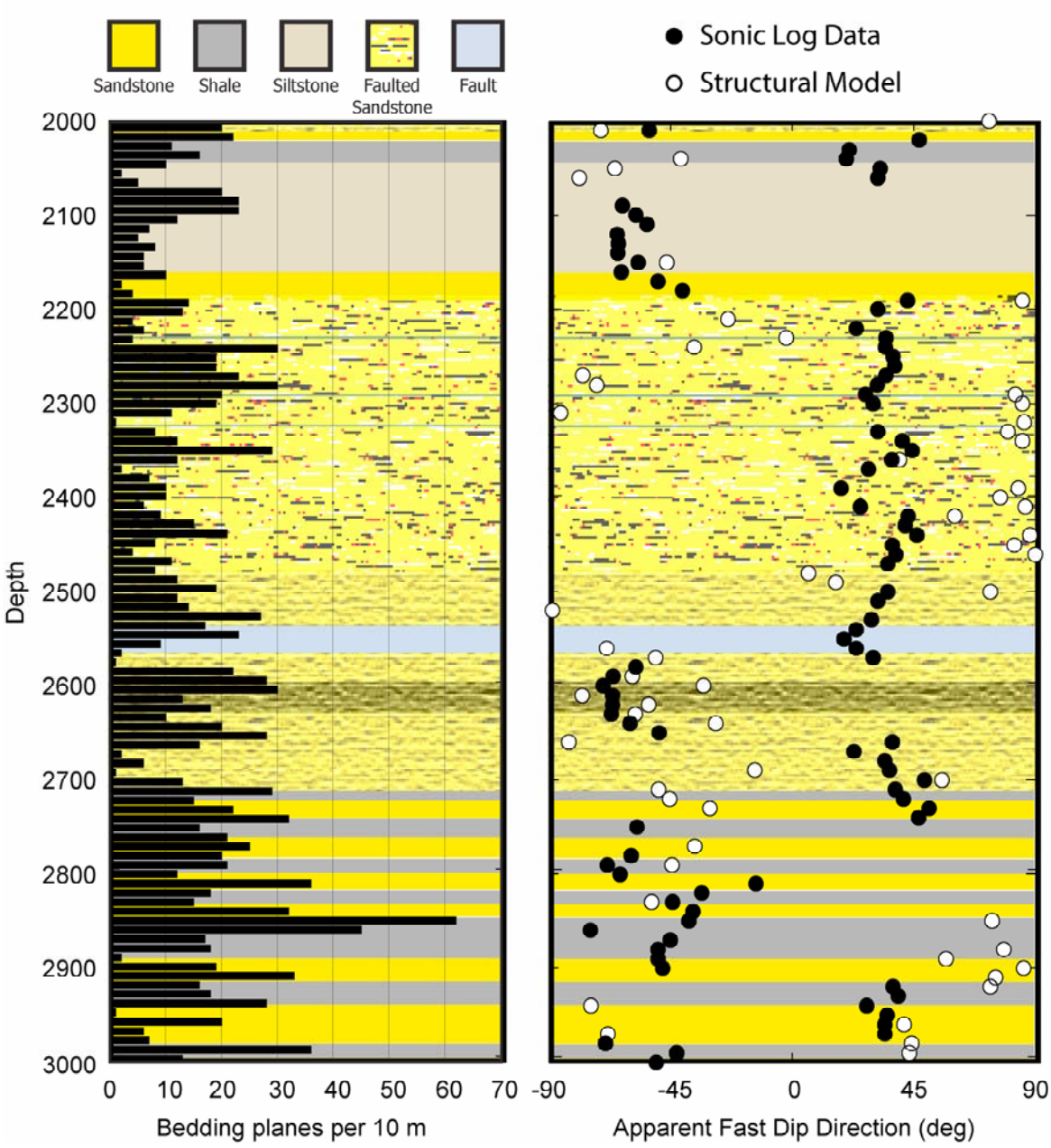

Figure 3.12: Histogram showing the number of bedding planes per 10 m interval used to compute the mean bed orientation using Fisher statistics, and comparison of observed fast directions from the sonic logs with the theoretical apparent fast direction that would be observed assuming the fast direction is oriented along the bedding planes.

The lack of correlation between the theoretical predictions for structural anisotropy and the observations in the well-cemented sandstones suggests stress-induced anisotropy in these units. The geometry of the borehole relative to the maximum compressive stress will dictate the amount of anisotropy observed [Sinha et al., 1994].

The FMI log indicates that the bedding within most of the sandstone units is spaced at much larger intervals on the order of 0.5 m to 2 m. The spacing of these bedding planes is comparable to the 1.5 m wavelength of the sonic waves at the low frequencies of interest, which explains why we only observe structural anisotropy within the shale despite the sub-parallel bedding planes being present within all the sedimentary units.

The fast direction is found by rotating the sonic log waveforms until the maximum and minimum energy is found at the time of the shear wave arrival, so the accuracy of the measurement is diminished when there is less anisotropy. Assuming, the observed anisotropy is due to S_{Hmax} preferentially closing fractures, the 54° inclination of SAFOD will reduce the amount of stress-induced anisotropy observed by up to ~50 % [Sinha et al., 1994]. Of course, this depends on the magnitudes of the other two principal stresses. However, in the sedimentary section of SAFOD the observed amount of anisotropy is over 4 % so we believe that the fast direction is a robust measurement. We cannot rule out that some of the anisotropy observed in the deviated section of the borehole is partly due to fractures being preferentially closed by the vertical stress, S_v. However, since the plane perpendicular to the borehole is at approximately 45° to both S_{Hmax} and S_v, and we expect S_{Hmax} to be slightly larger in magnitude in this strike-slip stress regime, it is unlikely that S_v is a dominant stress polarizing the shear waves.

Within the sandstone units, the S_{Hmax} direction inferred from anisotropy appears to be between 0° and 45° (north to northeast), which correlates well with observations in the pilot hole [Hickman and Zoback, 2004]. In the pilot hole there is a clockwise rotation of S_{Hmax} with depth, indicating increasing fault-normal compression deeper in the crust adjacent to the SAF. The results from this analysis support that interpretation, with S_{Hmax} estimated to be at an angle of 70° to the strike of the San Andreas at a vertical depth of

2500 m, corresponding to a measured depth of 2900 m., which is only 800 m lateral distance from the surface trace of the SAF.

3.6 Pilot hole array

In 2002, an array of 32 three-component 15 Hz seismometers was installed in the granitic portion of the pilot hole between depths of 850 m and 2050 m [see Chavarria et al., 2004, for more details]. Data from this array is well-suited for a shear wave splitting analysis because of the high sampling frequency (2 KHz) allowing us to pick the onset of the shear waves accurately. We analyze seismograms from 9 local microearthquakes at the 25 seismometers that were operational in the pilot hole at the time of the events. The earthquakes analyzed in this study are located on the SAF approximately 1.5 km laterally to the northeast and between depths of 2.7 and 7.3 km (Figure 3.13). The events were chosen as they had particularly well-constrained relocations [A. Chavarria, personal communication, 2005], were distributed laterally along a limited 4 km along-strike section of the SAF and had especially high signal to noise ratios with impulsive shear wave arrivals. The waveforms used in this study arrive on the array receivers at incidence angles of less than 40° within the shear wave window [Nuttli, 1961; Booth and Crampin, 1985] minimizing the likelihood of contamination from converted phases. The shear wave energy peaks at 20 Hz so we filter the seismograms using a Butterworth bandpass filter with limits of 5 Hz and 35 Hz.

The shear wave splitting analysis was conducted using a method that combines the methods of Silver and Chan [1991] and Zhang and Schwartz [1994]. We use a grid search to find the values of fast polarization direction and the time delay between the split shear waves that best correct the seismograms for the effects of anisotropy. The recorded seismograms are rotated to be parallel and perpendicular to the ray path and the particle motion of the S_H and S_V waveforms is plotted on a hodogram. The shear wave arrival is then determined by looking for an abrupt change from linear to elliptical particle motion. The seismograms are windowed around the shear wave arrival with 0.2 seconds before the shear wave arrival and 0.5 seconds after.

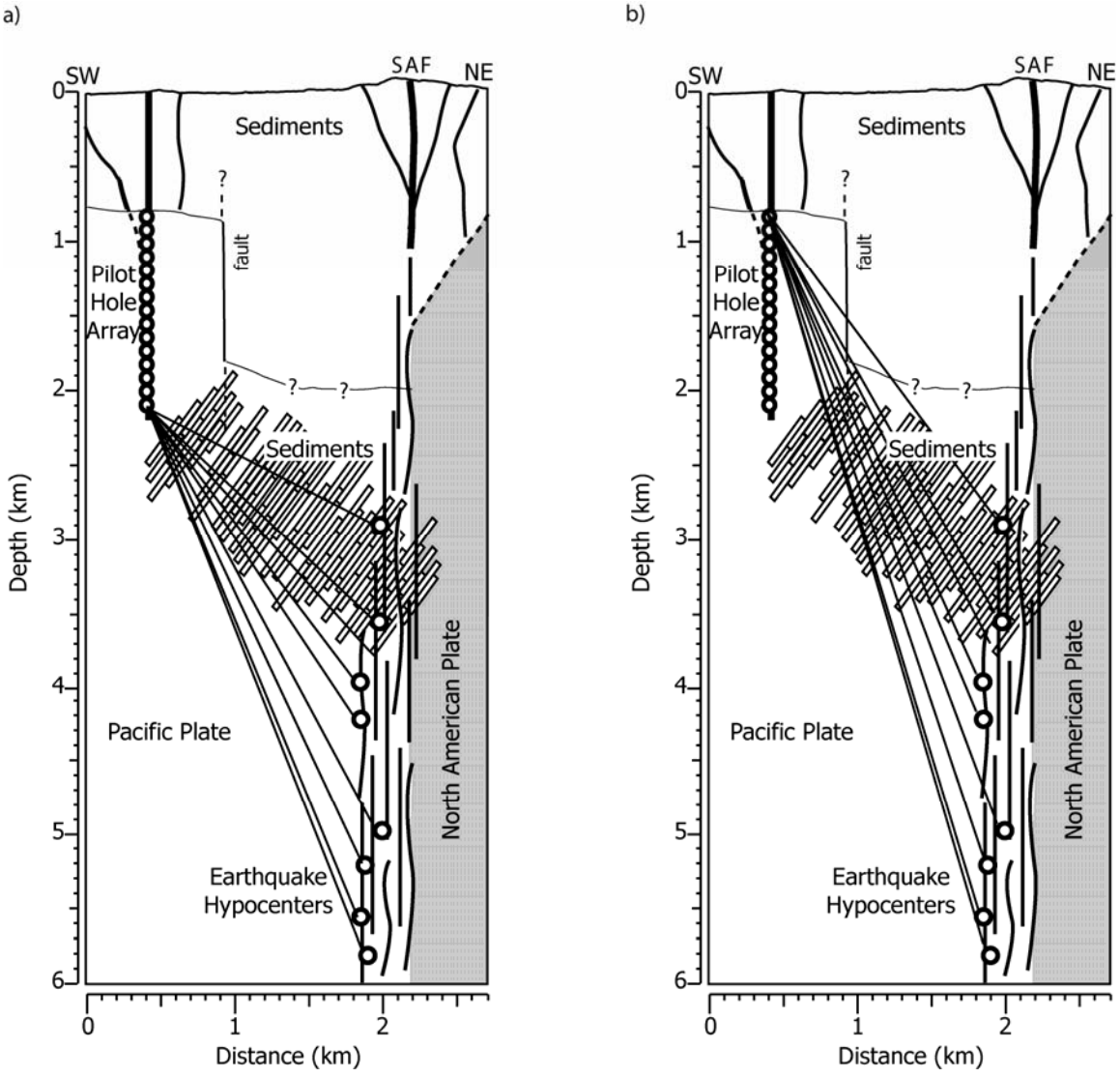

Figure 3.13: Diagram drawn to scale showing the pilot hole array and the nine earthquakes with approximated linear ray paths to a) a lower receiver in the array and b) an upper receiver in the array.

For orthogonal shear wave displacement vectors, u_1 and u_2 (directions 1 and 2 typically refer to north-south and east-west although may be any orthogonal geographic directions), the covariance matrix of the particle motion is computed by

$$c_{ij}(\alpha, \delta t) = \int_{-\infty}^{\infty} u^{\alpha}{}_i(t)\, u^{\alpha}{}_j(t - \delta t)\, dt \qquad i, j = 1,2 \qquad (2)$$

where $u^{\alpha}{}_l$ indicates a horizontal rotation of u_l by α degrees. We search over values of α, in one degree increments between -90° to 90° and over delay times, δt, between 0 and 50 ms in increments of the sampling frequency of 0.05 ms. If anisotropy exists, c_{ij} will have two non-zero eigenvalues, λ_1 and λ_2, where λ_1 is the largest (unless $\alpha = n\pi/2$ for n=1,2,…). The fast direction and delay time that best linearizes the particle motion is determined by minimizing λ_2 of the particle motion covariance matrix. To quantify the accuracy of the measurement we compute the degree of rectilinearity [Jurkevics, 1988] as:

$$r = 1 - \left(\frac{\lambda_1}{\lambda_2} \right). \qquad (3)$$

We only report measurements with a degree of linearity greater than 0.8 (1 being perfectly linear). Once rotated into a fast-slow coordinate system the fast and slow waveforms should have similar pulse shapes. Following the method of Zhang and Schwartz [1994] we confirm the fast polarization direction and more accurately determine the delay time by cross-correlating the windowed seismograms at each rotation step over lags of ± 0.2 seconds. Silver and Chan [1991] point out that maximizing the cross-correlation coefficient is similar to minimizing the determinant so we use the maximum cross-correlation coefficient to confirm that the seismograms have been rotated into the fast and slow polarization directions. We discard any measurement that has a cross-correlation coefficient of less than 0.7. To ensure the highest level of confidence we only report the fast polarization direction from the covariance matrix decomposition if the maximum cross-correlation coefficient is for a rotation azimuth within ± 10° of this measurement. The maximum uncertainty on the fast polarization directions is therefore estimated to be a maximum of ± 10°. The time delay we document is from the cross-

correlation procedure and is normalized by the distance along a linear ray path from the source to the receiver. An example of the shear wave splitting analysis procedure is shown in Figure 3.14.

The results of this study using data from the pilot hole array are shown in Figure 3.15 plotted at the depth of each receiver. The fast polarization directions are north-northeast in the upper receivers on the array, but below a depth of 1400 m the fast direction of the shear waves rotates to a northwest orientation.

The northeast fast direction observed on the upper receivers corresponds with delay times that decrease with depth from 8 ms/km at the top of the array to 4 ms/km at 1400 m. The fast directions determined on the upper receivers also correlate with the direction of S_{Hmax} determined in the pilot hole stress analysis [Hickman and Zoback, 2004] and the decrease in the amount of anisotropy is consistent with a decrease in the magnitude of stress-induced anisotropy as the confining pressure increases with depth.

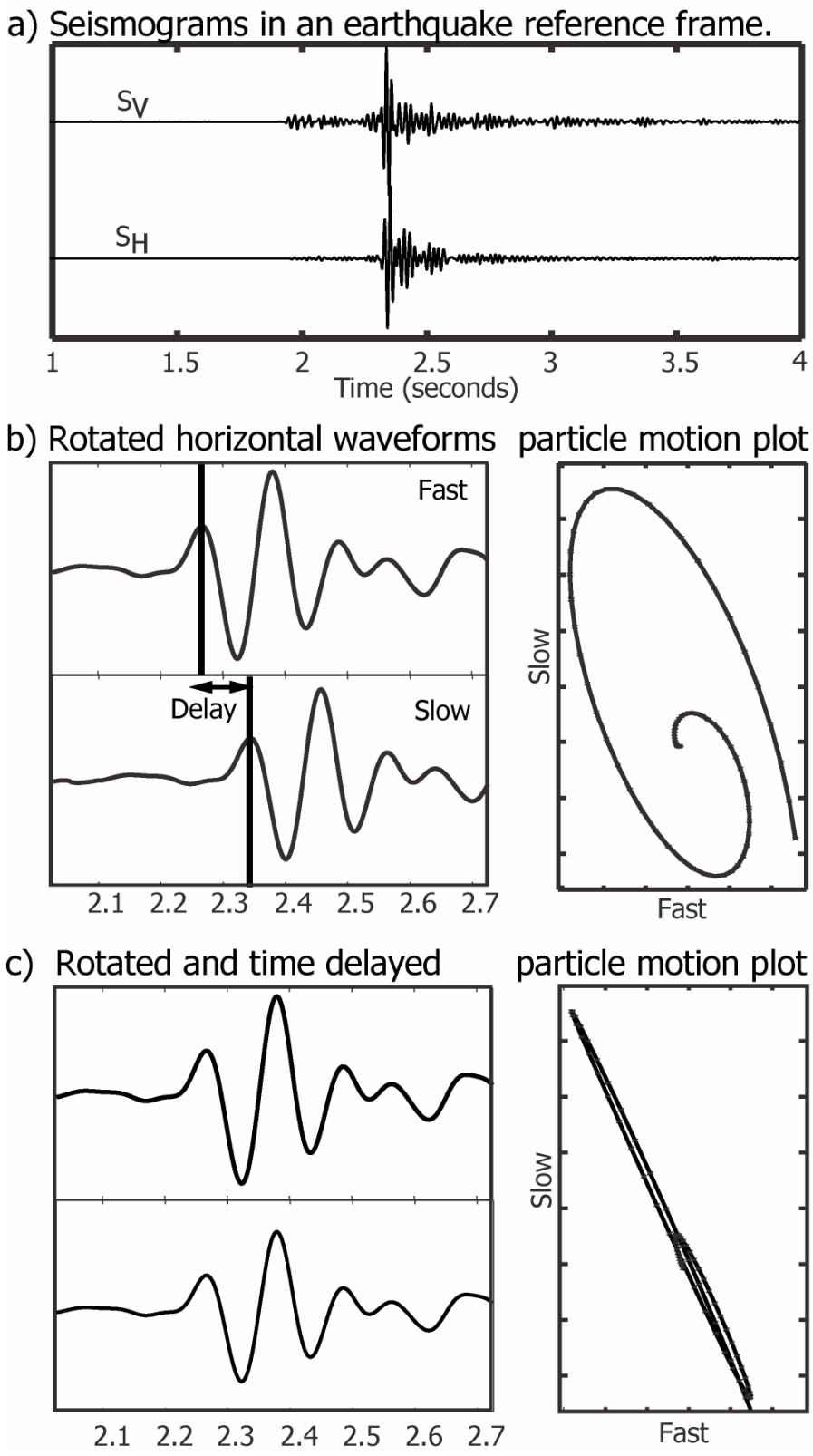

Figure 3.14: Example of the shear wave splitting procedure for one of the nine earthquakes to one of the receivers.

The northwest fast direction observed on the lower receivers are associated with delay times that show an apparent increase with depth from 4 ms/km at 1400 m up to about 10 ms/km at 2000 m. The fast direction of shear velocity anisotropy on the lower receivers of the pilot hole array is not consistent with stress-induced anisotropy, but the fast polarization directions do correlate with the fabric of the sedimentary bedding seen at greater depth along the ray paths (Figures 3.13 and 3.15) . The deeper a receiver is on the array, the more relative time the seismic waves spend being polarized by the fault fabric which accounts for the increasing delay time with depth. We contend that on these lower receivers we are observing structural anisotropy. However, it is not intuitively obvious how shear waves generated by a single earthquake can display both stress-induced anisotropy and structural anisotropy at different receivers in the same vertical array. To explain this apparent paradox we show simplified (i.e., linear) ray paths from the 9 earthquakes analyzed to both an upper and a lower receiver in Figure 3.13. Ray paths to the lower receivers are mostly through the northwest-striking sedimentary bedding seen in the SAFOD phase 1 image logs, explaining the presence of structural anisotropy observed on the lower receivers. Of course, the depth extent of the sedimentary package is unconstrained, so it is possible that these sediments extend to the deepest hypocenters studied here and that the lowermost ray paths are entirely in the sediments. In order to explain the presence of stress-induced anisotropy on the upper receives – even though these ray paths pass through this same sedimentary sequence – it is important to note that the amount of anisotropy is cumulative along the ray path but the polarization direction is controlled by the last anisotropic medium encountered by the wave [e.g., Crampin, 1991]. Thus, the lower ray paths, which are in the sediments immediately before being recorded, are polarized by the bedding. The ray paths to the upper receivers also go through the sedimentary sequence but the last portion of the ray paths is through the fractured Salinian granite above the sedimentary section, giving rise to the observed stress-induced anisotropy.

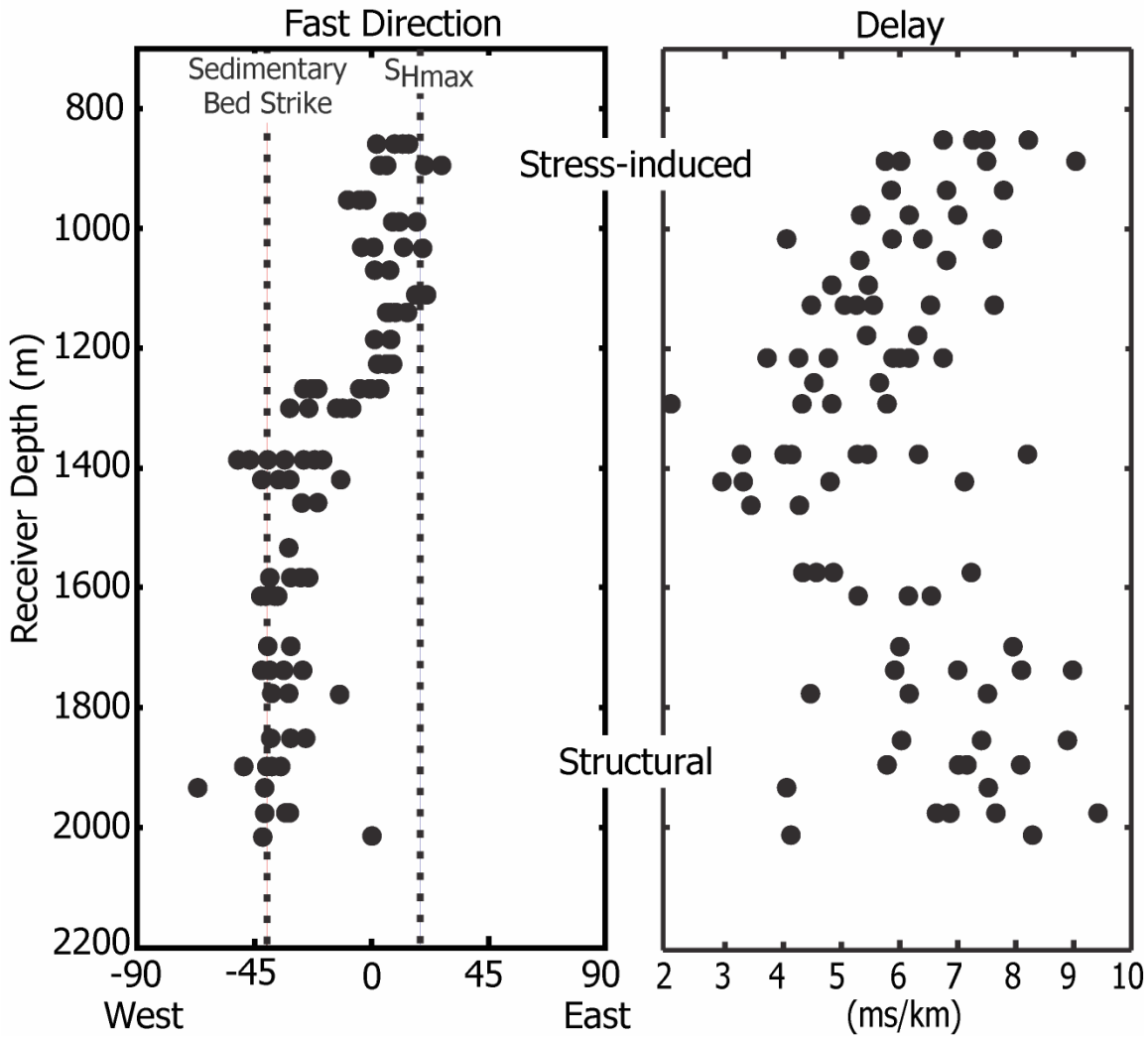

Figure 3.15: Results from shear wave splitting analysis of nine microearthquakes recorded on the pilot hole array. The strike of the sedimentary bedding planes and the orientation of S_{Hmax} are also shown for reference.

3.7 Discussion

Our observations of shear velocity anisotropy at multiple scales illustrate the effect of both frequency and scale. Seismic waves will only be polarized if the smallest wavelength is much larger than the individual layer thicknesses [Backus, 1962; Berryman, 1979]. The dipole sonic logs acquired within SAFOD correspond to wavelengths on the order of 1.5 m and are subsequently only polarized by the sedimentary bedding in the finely laminated shale when the bedding planes are closely spaced. In contrast, the seismograms recorded on the pilot hole array from earthquakes approximately 2 to 4 km away exhibit structural anisotropy for ray paths through the sedimentary sequence as both the shale and the sandstones have bedding planes at a much closer spacing than the seismic wavelengths of ~30 m.

The frequency dependence of anisotropy has important implications for the scale length of heterogeneities and establishing relationships between fractures and permeability anisotropy. Interestingly, we observe that the frequency of investigation has a significant effect on the amount of velocity anisotropy. In the sonic log the amount of velocity anisotropy is in the range of 2-10 %, whereas at seismic frequencies the amount of anisotropy is between 1-5 %. This is in direct contrast to the findings of Liu et al. [2002] who observed a decrease in the amount of velocity anisotropy as the frequency increased for identical shear wave paths. However, the sonic and seismic waves in this study sample very different volumes of the crust and the geometry of the ray paths with respect to the formation symmetry axes is significantly different for our sonic and seismic experiments.

Within the sedimentary sequence we shall first consider the lithologic effect at the two different scales. The amount of velocity anisotropy is usually in the range of 1-4 % for most rocks below a depth of 1-2 km [Crampin, 1994]. However, shales, clays and mudstones can induce a lithologically controlled anisotropy of several tens of percent. We suggest that the reason we observe an increase in anisotropy at higher frequencies is because the sonic waves are traveling over small volumes of highly anisotropic rock associated with the clay-rich sedimentary layers and/or shear zones. The lower amount of anisotropy at seismic frequencies recorded on the pilot hole is reflecting a loss of

resolution as the larger wavelengths average the properties of the anisotropic layers over tens of meters.

In the Parkfield region, the crust is anisotropic due to both stress and structure that act as competing mechanisms. At seismic frequencies, the shear waves are affected by structural anisotropy within the sedimentary sequence but the polarity of the time delay is reversed as the waves also travel through the granite/sandstones where stress-induced anisotropy is dominant. The integrated time delays from all anisotropic layers along the ray path are much smaller than one would expect if the waves had only traveled through anisotropic layers with the same sense of delay. In contrast, the sonic logs show increased amounts of anisotropy but the sonic waves are traveling through a much smaller volume (with homogeneous anisotropy) and thus retain the full anisotropic signature of each lithologic unit.

In addition, the geometry of investigation plays a key role. The seismic ray paths from the earthquakes to the pilot hole receivers are almost vertical and thus at an oblique angle to the sedimentary bedding. Thus, the horizontal components are not in a principle direction. In contrast, the sonic logs were acquired in a borehole-formation geometry where the tool was perpendicular to many of the bedding planes, so the fast direction recorded is close to the true fast direction of the formation. In other words, the seismic study has lower resolution because of the larger scale of investigation in such a heterogeneous crust and the geometry of the formation relative to ray path dictates the maximum anisotropy measured at the receiver.

3.8 Conclusions

We have analyzed shear velocity anisotropy in the crust adjacent to the SAF in Parkfield, CA, using dipole sonic shear logs and earthquakes recorded on a vertical three-component seismic array. We find that in the granite country rock the fast polarization direction of the shear waves in the vertical section of the pilot hole and main hole is parallel to the direction of S_{Hmax} and suggest this is stress-induced anisotropy caused by the preferential closure of macro- or microscopic fractures in response to an anisotropic stress state. We have developed a model to predict the fast direction that will be observed

for any arbitrary geometry of fast direction due to structure and borehole trajectory. For stress-induced anisotropy we show that the apparent fast direction will have the same azimuth as the maximum compressive stress, although the dip will depend on the orientation of the borehole. In the vertical sections of the pilot hole and main hole, the fast direction observed in the sonic log correlates remarkably well with measurements of S_{Hmax} from borehole breakouts, indicating stress-induced anisotropy. The amount of anisotropy in the granite decreases with depth, as expected for stress-induced anisotropy because the overall increase of confining pressure with depth closes fractures in all orientations and the shear velocity of the rock becomes less sensitive to stress.

In the sedimentary sequence penetrated at depth by SAFOD the sonic log exhibits two distinct fast shear polarizations: a northeast fast direction in the sandstones and a northwest fast in the siltstone and shale units characterized by finely laminated, clay-rich planes. We use our theoretical model to show that in the clay rich shale and siltstone units the observed fast direction is due to the sonic shear waves being polarized along the bedding planes. In the well cemented sandstones (that have physical properties similar to the granite) we observe stress-induced anisotropy. The theory we present allows us to examine the importance of the geometry of the borehole relative to both the structural (i.e. bedding) and stress-induced directions of velocity anisotropy when interpreting the sonic logs. The observation of a northeast-southwest fast direction is in good agreement with other stress measurements in the region [Townend and Zoback, 2004] and locally at the SAFOD site [Hickman and Zoback, 2004]. Our results support the theory of a weak SAF with nearly fault-normal compression at a vertical depth of 2.5 km at a distance of about 800 m southwest of the surface trace of the fault.

An analysis of earthquakes recorded on the pilot hole array at seismic frequencies reveals stress-induced anisotropy at receivers in the top of the array and structural velocity anisotropy for ray paths to receivers in the lower half of the array. We contend that this is because ray paths to the upper receivers pass back through the granite where stress-induced anisotropy dominates and the fast polarization direction observed is highly dependent on the last anisotropic medium encountered.

Structural anisotropy is a stronger mechanism than stress-induced anisotropy at depth and we observe an increase in delay times at both sonic and seismic frequencies for structural mechanisms. In particular, within clay-rich intervals the intrinsic anisotropy of the clay platelets gives rise to an extremely high anisotropy (up to 10%) at sonic frequencies. This may prove useful as a lithologic indicator. At seismic frequencies the amount of anisotropy is in the range of 1-4 % as the longer seismic wavelengths average out the anisotropic effect of many layers. In conclusion, both structural and stress-induced mechanisms control the velocity anisotropy at sonic and seismic frequencies and are strongly dependent on the scale and geometry of investigation.

Acknowledgements

We thank Tom Plona and Jeff Alford at Schlumberger for helpful discussions and comments on sonic log acquisition and interpretation. We also thank the many members of the SAFOD science team for thought-provoking discussions. This work was supported by NSF grant EAR-0323938-001 and the Stanford Rock Physics and Borehole project.

References

Alford, R. M., 1986, Shear data in the presence of azimuthal anisotropy: *Ann. Internat. Mtg., Soc. Expl. Geophys*., Expanded abstracts, **56**, 476-479.

Anderberg, M. R., 1973, *Cluster analysis for applications (Probability and mathematical statistics, 19)*: Academic Press, New York, 359 pp.

Backus, M., 1962, Long-wave elastic anisotropy produced by horizontal layering: *J. Geophys. Res*., **67**, 4427.

Barton, C. A., and Zoback, M. D., Stress perturbations associated with active faults penetrated by boreholes: Possible evidence for near-complete stress drop and a new technique for stress magnitude measurement: *J. Geophys. Res*., **99**, 9373-9390.

Berryman, J. G., 1979, Long-wave elastic anisotropy in transversely isotropic media: *Geophysics*, **44**, 897-917.

Boness, N. L., and Zoback, M. D., 2004, Stress-induced seismic velocity anisotropy and physical properties in the SAFOD Pilot Hole in Parkfield, CA: *Geophys. Res. Lett*., **31**, L15S17.

Booth, D. C., and Crampin, S., 1985, Shear-wave polarizations on a curved wavefront at an isotropic free-surface: *Geophys. J. R. Astron. Soc*., **83,** 31-45.

Brune, J. N., Henyey, T. L., and Roy, R. F., 1969, Heat flow, stress, and rate of slip along the San Andreas fault, California*: J. Geophys. Res*., **74**, 3821-3827.

Chavarria, J. A., Malin, P. E., and Shalev, E., 2004, The SAFOD Pilot Hole seismic array: Wave propagation effects as a function of sensor depth and source location: *Geophys. Res. Lett*., **31**, L12S07.

Chen, S. T., 1988, Shear-wave logging with dipole sources: *Geophysics*, **53**, 659-667.

Crampin, S., 1986, Anisotropy and transverse isotropy: *Geophys. Prosp.,* **34,** 94-99.

Crampin, S., 1991, Wave propagation through fluid-filled inclusions of various shapes: interpretation of extensive dilatancy anisotropy: *Geophys. J. Int.,* **107,** 611-623.

Crampin, S., 1994, The fracture criticality of crustal rocks: *Geophys. J. Int.,* **118,** 428-438.

Crampin, S., and Lovell, J. H., 1991, A decade of shear-wave splitting in the Earth's crust: what does it mean? what use can we make of it? and what should we do next?: *Geophys. J. Int*., **107**, 387-407.

Darot, M., and Bouchez, J. L., 1976, Study of directional data distributions from principal preferred orientation axes: *J. Geol*., **84**, 239-247.

Fisher, N. I., Lewis, T., and Embleton, B. J. J., 1987, *Statistical Analysis of Spherical Data*: Cambridge University Press, Cambridge, 329 p.

Harrison, A. R., Randall, C. J., Aron, J. B., Morris, C. F., Wignall, A. H., and Dworak, R. A., 1990, Acquisition and analysis of sonic waveforms from a borehole monopole and dipole source for the determination of compressional and shear speeds and their relation to rock mechanical properties and surface seismic data: *SPE Annual Technical Conference and Exhibition*, New Orleans, Paper SPE 20557.

Hickman, S., and Zoback, M. D., 2004, Stress orientations and magnitudes in the SAFOD Pilot Hole from observations of borehole failure: *Geophys. Res. Lett*., **31**, L15S12.

Hickson, T. A., 1999, *A study of deep-water deposition; constraints on the sedimentation mechanics of slurry flows and high-concentration turbidity currents, and the facies architecture of a conglomeratic channel-overbank system*: Ph.D. Thesis, Stanford University, 470 pp.

Hickson, T. A., and Lowe, D. R., 2002, Facies architecture of a submarine fan channel-levee complex: Juniper Ridge Conglomerate, Coalinga, California: *Sedimentology*, **49**, 335-362.

Hornby, B. E., 1998. Experimental laboratory determination of the dynamic elastic properties of wet, drained shales: *J. Geophys. Res*., **103**, 29945-29964.

Jaeger, J., and Cook, N. G. W., 1979, *Fundamental of Rock Mechanics*: Chapman & Hall, London, 3rd edition, 593 pp.

Johnston, J. E., and Christensen, N. I., 1995, Seismic anisotropy of shales: *J. Geophys. Res*., **100**, 5991-6003.

Jurkevics, A., 1988, Polarization analysis of three-component array data: *Bull. Seismol. Soc. Am*., **78**, 1725-1743.

Kimball, C. V., and Marzetta, T. M., 1984, Semblance processing of borehole acoustic array data: *Geophysics*, **49**, 264-281.

Kiraly, L., 1969, Statistical analysis (orientation and density): *Geol. Rundshau*, **59**, 125-151.

Lachenbruch, A. H., and Sass, J. H., 1980, Heat flow and energetics of the San Andreas fault zone: *J. Geophys. Res*., **85**, 6185-6223.

Leslie, H. D., and Randall, C. J., 1990, Eccentric dipole sources in fluid-filled boreholes: Experimental and numerical results: *J. Acoust. Soc. Am*., **87**, 2405-2421.

Liu, E., Crampin, S., Queen, J. H., and Rizer, W. D., 1993. Behavior of shear waves in rocks with two sets of parallel cracks: *Geophys. J. Int.,* **113,** 509-517.

Liu, E., Queen, J. H., Li, X.-Y., Chapman, M., Lynn, H. B., and Chesnokov, E. M., 2003, Analysis of frequency-dependent seismic anisotropy from a multicomponent VSP at Bluebell-Altamont field, Utah: *J. App. Geophys*., **54**, 319-333.

Lynn, H. B., and Thomsen, L. A., 1986, Shear-wave exploration along the principle axes: *Ann. Internat. Mtg., Soc. Expl. Geophys*., Expanded Abstracts, **56**, 473-476

Lynn, H. B., and Thomsen, L. A., 1990, Reflection shear-wave data collected near the principle axes of azimuthal anisotropy: *Geophysics*, **55**, 147-156.

Meadows, M., and Winterstein, D., 1994, Seismic detection of a hydraulic fracture from shear-wave VSP data at Lost Hills Field, California: *Geophysics*, **57**, 11–26.

Moos, D., and Zoback, M. D., 1983, In-situ studies of velocity in fractured crystalline rocks: *J. Geophys. Res*., **88**, 2345-2358.

Mount, V. S., and Suppe, J., 1987, State of stress near the San Andreas fault: Implications for wrench tectonics: *Geology*, **15**, 1143-1146.

Mueller, M. C., 1991, Prediction of lateral variability in fracture intensity using multicomponent shear-wave seismic as a precursor to horizontal drilling: *Geophys. J. Int*., **107**, 409-415.

Mueller, M. C., 1992, Using shear waves to predict lateral variability in vertical fracture intensity: *Leading Edge*, **33**, 29-35.

Nur, A., and Simmons, G., 1969, Stress induced velocity anisotropy in rock: An experimental study: *J. Geophys. Res*., **74**, 6667-6674.

Nuttli, O., 1961, The effect of the Earth's surface on the S wave particle motion: *Bull. Seismol. Soc. Am*., **44**, 237-246.

Roeloffs, E. and Langbein, J., 1994, The earthquake prediction experiment at Parkfield, California: *Rev. Geophys*., **32**, 315-336.

Sayers, C. M., 1994, The elastic anisotropy of shales: *J. Geophys. Res*., **99**, 767-774.

Schlumberger, 1995, *DSI* Dipole Shear Sonic Image*: Oilfield Marketing Services, Houston, Texas, pp. 36.

Shamir, G., and Zoback, M. D., 1992, Stress orientation profile to 3.5 km depth near the San Andreas fault at Cajon Pass, California: *J. Geophys. Res*., **97**, 5059-5080.

Silver, P. G., and Chan, W. W., 1991, Shear wave splitting and subcontinental mantle deformation: *J. Geophys. Res*., **96**, 16429-16454.

Sinha, B.K., and Kostek, S., 1996, Stress-induced azimuthal anisotropy in borehole flexural waves: *Geophysics*, **61**, 1899-1907.

Sinha, B. K., Norris, A. N., and Chang, S.-K., 1994, Borehole flexural modes in anisotropic formations: *Geophysics*, **59**, 1037-1052.

Thomsen, L., 1986, Weak elastic anisotropy: *Geophysics*, **51**, 1954-1966.

Townend, J., and Zoback, M. D., 2001, How faulting keeps the crust strong: *Geology*, **28**, 399-402.

Townend, J., and Zoback, M. D., 2004, Regional tectonic stress near the San Andreas fault in central and southern California: *Geophys. Res. Lett*., **31**, L15S11.

Williams, C. F., Grubb, F. V., and Galanis Jr., S. P., 2004, Heat flow in the SAFOD pilot hole and implications for the strength of the San Andreas Fault: *Geophys. Res. Lett*., **31**, L15S14.

Willis, H., Rethford, G., and Bielanski, E., 1986, Azimuthal anisotropy: Occurrence and effect on shear wave data quality: *Ann. Internat. Mtg., Soc. Expl. Geophys*., Expanded Abstracts, **56**, 479-481.

Zhang, Z., and Schwartz, S. Y., 1994, Seismic anisotropy in the shallow crust of the Loma Prieta segment of the San Andreas fault system: *J. Geophys. Res*., **99**, 9651-9661.

Zinke, J. C., and Zoback, M. D., 2000, Structure-related and stress-induced shear wave velocity anisotropy: Observations from microearthquakes near the Calaveras fault in central California: *Bull. Seis. Soc. Am*., **90**, 1305-1312.

Zoback, M. D., Zoback, M. L., Mount, V. S., Suppe, J., Eaton, J. P., Healy, J. H., Oppenheimer, D., Reasenberg, P., Jones, L., Raleigh, C. B., Wong, I. G., Scotti, O., and Wentworth, C., 1987, New evidence on the state of stress of the San Andreas fault system: *Science*, **238**, 1105-1111.

Chapter 4

Physical properties and seismic anisotropy observations in SAFOD: implications for the strength of the San Andreas Fault

Abstract

Measurements from the San Andreas Fault Observatory at Depth (SAFOD) indicate that the core of the San Andreas Fault is a ~20 m wide zone of anomalous physical properties, imbedded within a ~250 m wide damage zone, consistent with inferences from fault zone guided waves. Within the ~20m wide fault core, we observe very low P- and S-wave velocities and very high porosity. In addition, we use shear velocity anisotropy measurements in the borehole to study stress orientation within and immediately adjacent to the active fault zone. By modeling the structural anisotropy associated with sedimentary bedding planes we are able to differentiate between structurally-controlled and stress-induced shear velocity anisotropy. The presence of stress-induced anisotropy in SAFOD enables us to document stress orientations at a fine scale along a 2 km profile across the San Andreas Fault, providing valuable information about the state of stress previously undetected at the resolution of regional stress observations. We find evidence for fault normal compression in the crust outside of the fault zone, but the maximum horizontal compressive stress appears to rotate within the narrow fault core to an angle consistent with the theoretical predictions of Rice [1992] for the model of a weak fault in a strong crust.

4.1 Introduction

The San Andreas Fault Observatory at Depth (SAFOD) provides a unique opportunity to study the physical properties and state of stress of a major plate-bounding fault at seismogenic depths. The SAFOD project consists of two boreholes located 1.8 km southwest of the surface trace of the San Andreas Fault (SAF): a vertical pilot hole that was drilled in 2002 to a depth of 2200 m and a main borehole drilled in two phases in 2004 and 2005. At the surface, the main borehole is only 7 m from the pilot hole. It remains essentially vertical to a depth of ~1500 m before deviating from vertical at an angle of 54° - 60° to the northeast toward the SAF (Figure 4.1) to a total vertical depth of 3200 m.

Drilling of phase 2 across the SAF between measured depths of 3000-4000 m (vertical depths of 2500-3100 m) was completed in September 2005 [Zoback et al., 2005]. The 8.5" borehole was rotary drilled and throughout the drilling process, cuttings samples were collected every 10 m and real-time mud gas analyses were performed [Wiersberg, 2005]. A comprehensive suite of geophysical logs was acquired using logging while drilling (LWD) technology and conventional tubing-conveyed logs were collected in the open hole after drilling was completed [Zoback et al., 2005; Hickman et al., 2005]. A side-wall coring operation yielded 52 small (0.75" diameter, 1" length) side-wall cores over a range of depths in the open hole. Finally, after setting casing, a 4 m spot core (2.6" diameter) was collected at the bottom of the hole at 3.1 km and a hydrofracture experiment was carried out [Zoback and Hickman, 2005].

The locations of the target earthquakes have been relocated using velocities measured at depth in SAFOD [Ellsworth et al, 2005] and are shown on Figure 4.1 for reference. The SAFOD borehole intersects the projected SAF plane determined from the earthquake relocations at a vertical depth of ~2900 m, which corresponds to a measured depth along the borehole of ~3450 m. In this paper I present data acquired in phase 2 of SAFOD across the SAF between measured depths of 3000-4000 m.

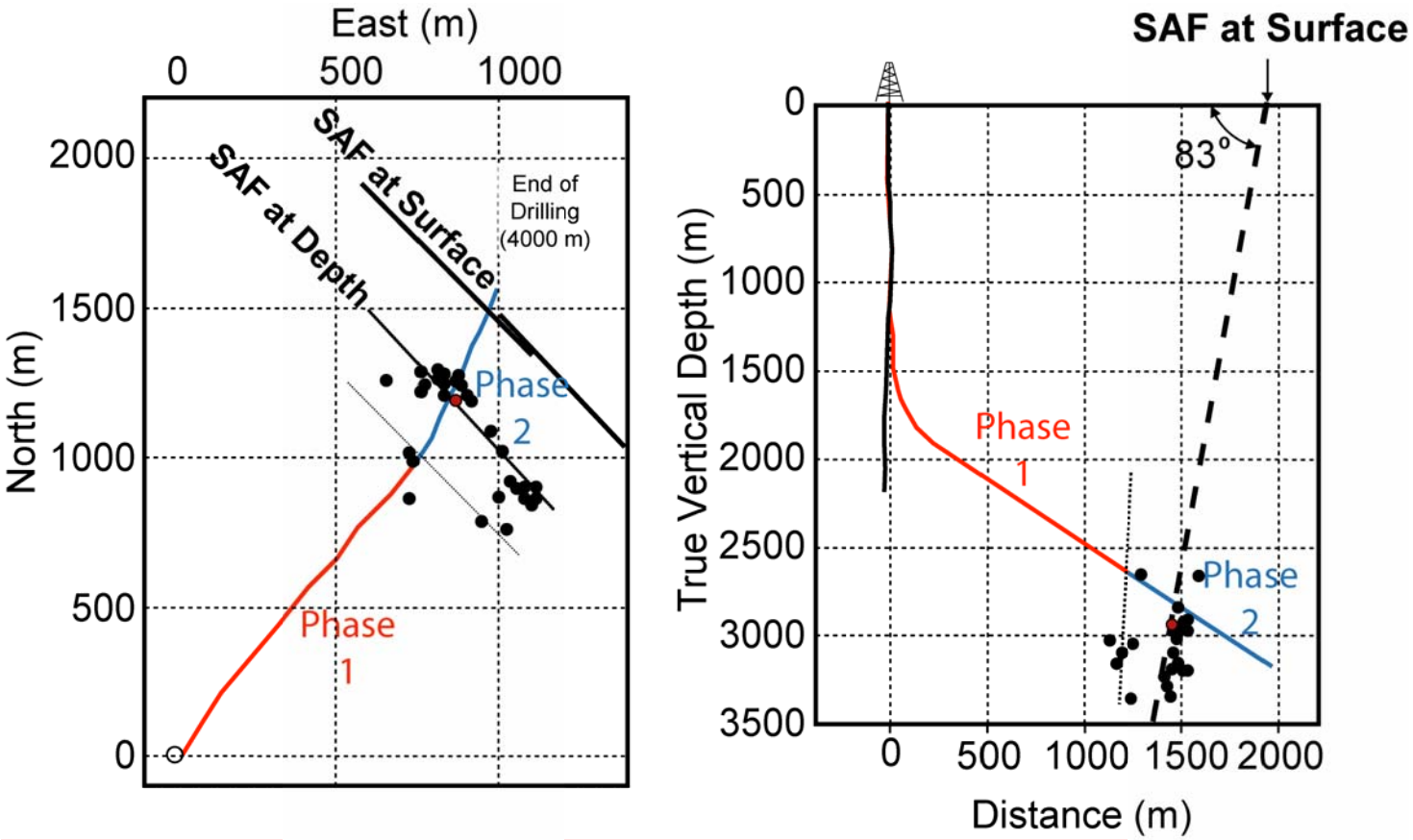

Figure 4.1: a) Map showing the trajectory of SAFOD relative to the surface trace of the SAF and the depth of the fault at depth determined from the precise locations of the target earthquakes. b) Cross section showing the SAFOD pilot hole (black) and main hole along an azimuth of 33° (the average azimuth of phase 2) with the locations of the target earthquakes and the surface trace of the SAF. A plane from the target events to the surface trace would dip to the southwest at an angle of 83°.

Considering the lithologic differences between the rock types on either side of the SAF at Parkfield, it is not surprising that there is a marked lateral variation in the physical properties of the crust across the fault zone. Extensive surface experiments have revealed that the seismic wave velocities and densities of the Franciscan Complex, Salinian block, and fault zone itself, are significantly different, presumably due to varying crustal properties [e.g., Wesson, 1971; Pavoni, 1973; Ellsworth, 1975; Aki and Lee, 1976; Walter and Mooney, 1982; Michelini and McEvilly, 1991; Eberhart-Phillips and Michael, 1993; Thurber et al., 1996; 1997].

However, the variation in physical properties of the upper crust is larger than one can easily explain using rock composition alone. Experiments utilizing explosion sources [Healy and Peake, 1975; Feng and McEvilly, 1983; Li et al., 1997], seismic P-wave tomography studies [Hole, 1992; Lin and Roeker, 1997; Thurber et al., 1997], and observations of fault zone guided waves [e.g., Li et al., 1990; Ben-Zion and Malin, 1990; 1991; Leary and Ben-Zion, 1992; Jongmans and Malin, 1995; Li et al, 1997], indicate that the SAF zone is associated with low velocities. In other words, the fault is not a simple delineation between two rock types but is within a broad zone of unique physical properties.

Velocity models [Rymer et al., 1999] and potential field data [Griscom and Jachens, 1990; Jachens, 2002] indicate a "step" in the basement on the southwest side of the fault, reflecting the markedly different rock types on either side of the fault. This may be a result of the regional data having wavelengths greater than the width of the fault zone. In addition, earthquake relocation studies indicate that the densest clusters of earthquakes are correlated with a sharp contrast in P-wave velocity [Michael and Eberhart-Phillips, 1991].

Electrical resistivity anomalies determined from surface magnetotelluric data Unsworth et al., 1997; 1999; 2000; Unsworth and Bedrosian, 2004; Eberhart-Phillips et al., 1990; 1995] and geophysical logs [Boness and Zoback, 2005] in the vicinity of Parkfield indicate low resistivity associated with sedimentary rocks on the southwest side if the SAF and perhaps the fault zone itself. Since the presence of fluids, serpentinite, or clays significantly lowers the resistivity of the host rock, decreased resistivity within the

fault zone is clearly of great importance for understanding the earthquake process. Unsworth et al. [1997] also observe that microseismicity mapped by Nadeau et al. [1995] coincides with the western edge of the low resistivity zone. Seismic reflection studies have revealed a notable absence of coherent reflectors and studies of fault zone guided waves suggest the fault zone consists of heavily fractured material [McBride and Brown, 1986]. The Parkfield segment of the SAF also has a high V_p/V_s ratio of 1.9 [Michelini and McEvilly, 1991], revealing a much greater reduction in S-wave velocity than in P-wave velocity. The lateral extent of the fault zone remains a controversial topic with estimates ranging from 100 m [Li et al., 1990; Li and Leary, 1990] to a few kilometers [Healy and Peake, 1975; Feng and McEvilly, 1983; Li et al., 1997; Eberhart-Phillips and Michael, 1993]. This problem remains partly because of the lack of in situ data.

The nature and extent of the SAF zone at depth is unknown, with different data sets illuminating different features. Studies of exhumed faults within the SAF system, like the Punchbowl fault [Chester and Logan, 1986; Chester et al., 1993; Chester et al, 2005] and the San Gabriel Fault [Chester et al., 1993; Evans and Chester, 1995] provide limited constraints on physical properties for use in models of crustal faulting. Field observations indicate that the Punchbowl is composed of a fault zone core of sheared cataclasite and ultracataclasite a few meters across, surrounded by a substantial damage zone of highly fractured country rock on the order of a few hundred meters wide (Figure 4.2). However, the relevance of these observations to the SAF in general is dependent on two assumptions: First, that the structure of an exhumed fault is indicative of processes and conditions at depth when the fault was actively deforming and that the physical properties are representative of the physical nature of faults at seismogenic depths. This assumption will depend on the exhumation process, which may significantly alter the physical properties of the fault. Second, that the exhumed faults are similar to other fault segments along the SAF system with which they are compared. Studies of exhumed faults provide information about one unique portion of the fault that may have deformed by significantly different processes compared to other segments (e.g., creep vs. seismic slip).

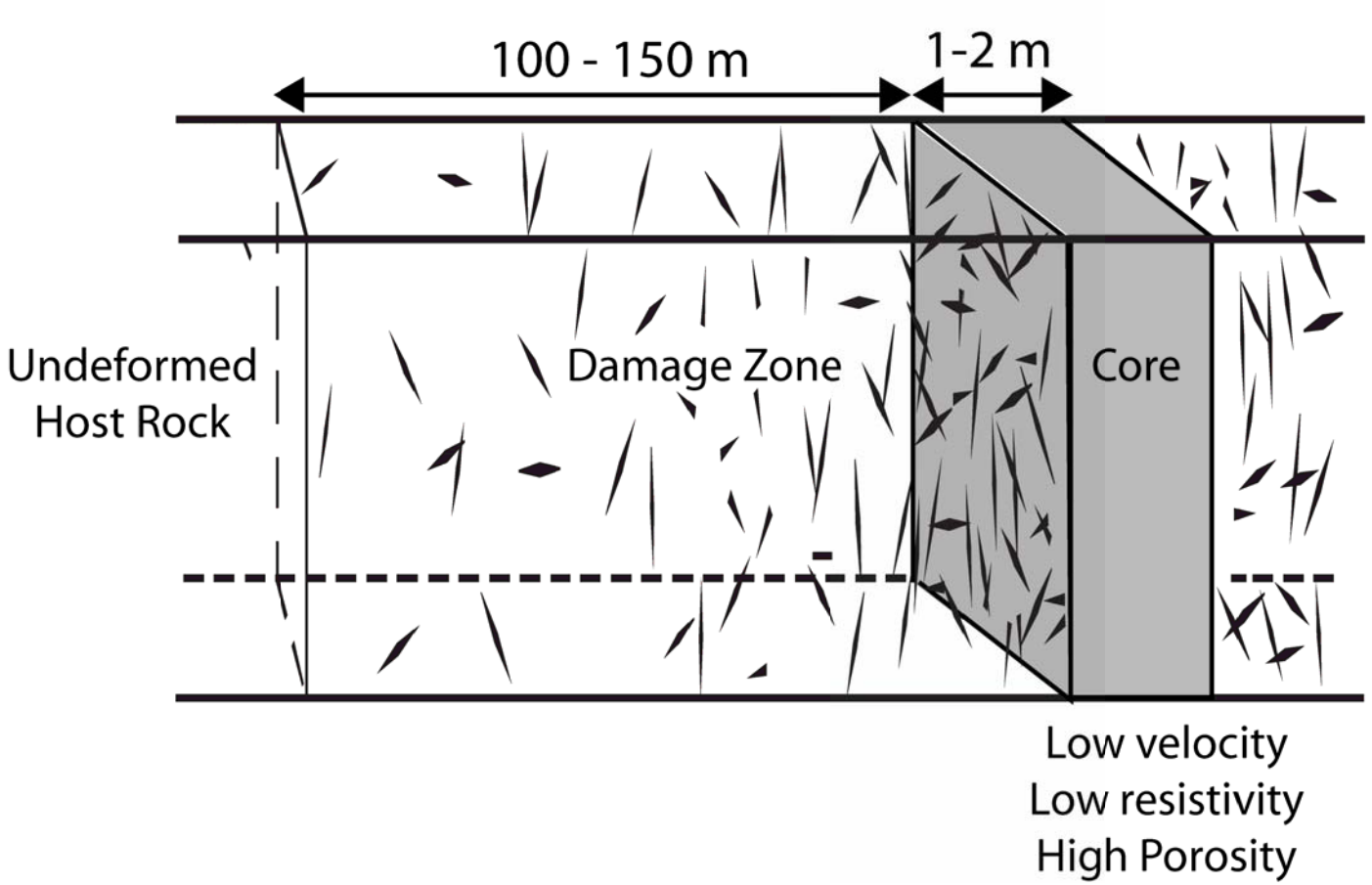

Figure 4.2: Cartoon illustrating the structure of the exhumed Punchbowl Fault, within the SAF system, as determined from field observations [Modified from Chester et al., 2005]. The fault core is a few meters wide surrounded by a 200 m wide damage zone consisting of highly fractured rocks.

In addition to understanding the physical properties of major fault zones, the state of stress along faults like the San Andreas is critical for furthering our knowledge of faulting mechanics. Regional observations of the direction of the maximum horizontal compressive stress (S_{Hmax}) from earthquake focal mechanism inversions and wellbore data (Figure 4.3a), indicate that S_{Hmax} is at a very high angle to the SAF fault [Zoback *et al.*, 1987; Mount and Suppe, 1987; Townend and Zoback, 2004]. However, in the creeping section of the SAF, focal mechanism inversions very close to the fault (1-3 km) indicate a localized rotation of S_{Hmax} to an angle of about ~45° to the fault [Provost and Houston, 2001]. From these observations of S_{Hmax} and the lack of a heat anomaly due to frictional heating [e.g., Lachenbruch and Sass, 1973; 1980; Williams et al., 2004], the SAF appears to be a weak fault that slips at low shear stress [Zoback *et al.*, 1987; Mount and Suppe, 1987].

The possible explanations for this stress-heat flow paradox include high pore pressure within the fault zone to reduce the effective normal stress [e.g., Rice, 1992; Sleep and Blanpied, 1992], material properties with a low coefficient of friction that are able to promote sliding at low shear stress [e.g., Lachenbruch and Sass, 1980] and dynamic weakening mechanisms [e.g., Brune et al., 1993]. The concept of a weak fault in a strong crust would predict that in the adjacent crust the orientation of S_{Hmax} is at a high angle to the fault. However, within the fault core there is a rotation of S_{Hmax} to a more acute angle to the fault due to either elevated pore pressure or the presence of frictionally weak materials [Rice, 1992]. However, the width of this zone must be extremely narrow with respect to any deforming region to satisfy the condition of right-lateral, fault-parallel slip.

The closest measurement of stress to the SAF was made in 2002 at a depth of 2.2 km in the SAFOD pilot hole [Hickman and Zoback, 2004] and S_{Hmax} was found to be in good agreement with the northeast-southwest regional stress field (Figure 4.3b). However, the measurement in the pilot hole is still 1.8 km away from the surface trace of the SAF and appears to be reflecting the strong crust adjacent to the fault zone. The lack of stress measurements in the immediate proximity of the fault core has made it impossible to fully test the hypothesis of a narrow weak fault in a strong crust.

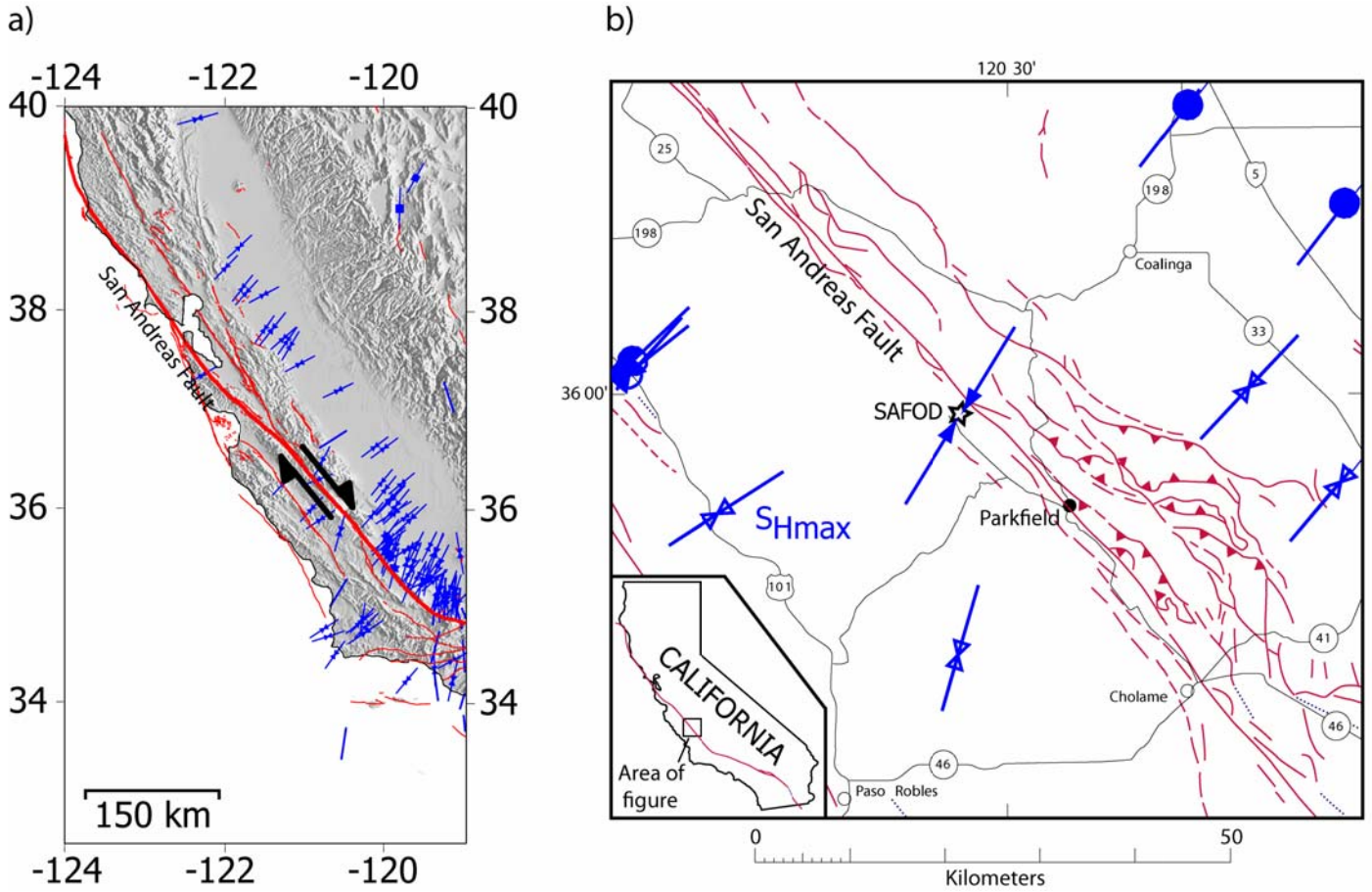

Figure 4.3: a) Map showing regional observations of S_{Hmax} (in blue) from focal mechanism inversions and wellbore data relative to the surface trace of the SAF. b) Map of the Parkfield region centered on the SAFOD drill site showing the good agreement between the measurement of S_{Hmax} at 2.2 km depth in the pilot hole, 1.8 km away from the surface trace of the SAF, with regional stress data.

In this paper I present an analysis of the physical properties and shear velocity anisotropy data observed in SAFOD across the SAF. Shear velocity anisotropy at this scale is sensitive to the state of the stress and structural controls like sedimentary bedding [Boness and Zoback, 2005]. I utilize the theoretical model developed in Chapter 3 to differentiate between structural and stress-induced anisotropy, with the ultimate goal of profiling the orientation of S_{Hmax} at high resolution across the fault plane.

4.2 Physical properties of the San Andreas Fault

During phase 1 of drilling, the SAFOD borehole intersected granite to a measured depth of 1920 m and then penetrated a sequence of sedimentary rocks consisting of alternating sandstone and shales [Boness and Zoback, 2005]. The rocks encountered during phase 2 of drilling across the SAF are similar in nature to the sedimentary rocks at the bottom of phase 1 and in this section I document the physical properties characterizing the lithologic units and faults. I present an integrated analysis of petrophysical data from the SAFOD borehole between depths of 3000-4000 m including physical property logs, Logging While Drilling (LWD) azimuthal resistivity (GVR) and post-drilling electrical conductivity image logs (STAR), rock cuttings collected every 3 m during drilling and real-time gas measurements (Wiersberg and Erzinger, 2005). Initially, I use the petrophysical logs (compressional and shear velocity, resistivity, gamma ray, density and neutron porosity) to characterize units of similar physical properties (Figure 4.4). I then assess the lithology by studying the texture and bedding visible in the sections of the image logs that are of good quality (Figure 4.5).

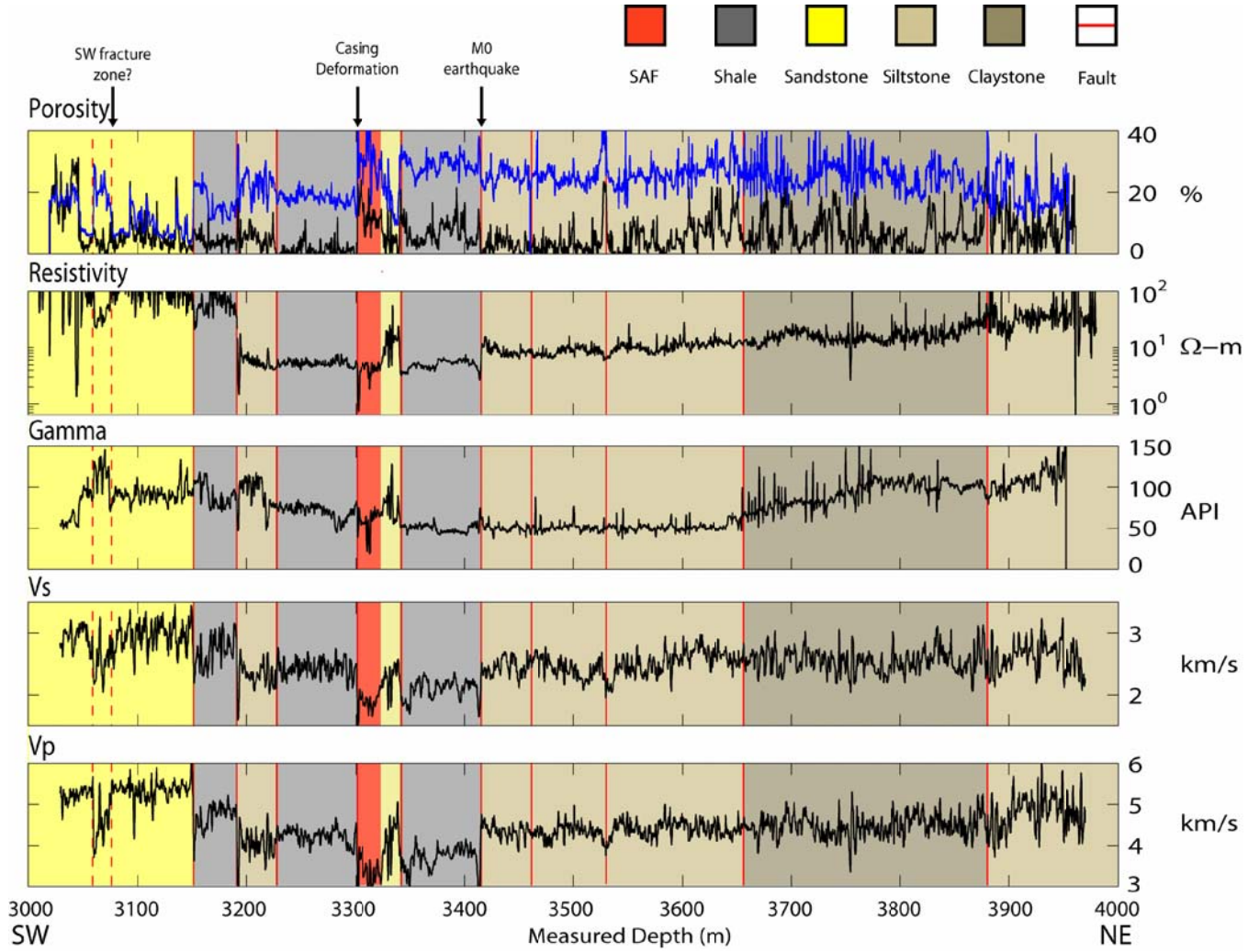

Figure 4.4: Petrophysical logs acquired in phase 2 of SAFOD overlain on major geologic units determined from physical properties, image logs and cuttings analyses. On the porosity log, the density porosity is shown in black and the neutron porosity is shown in blue.

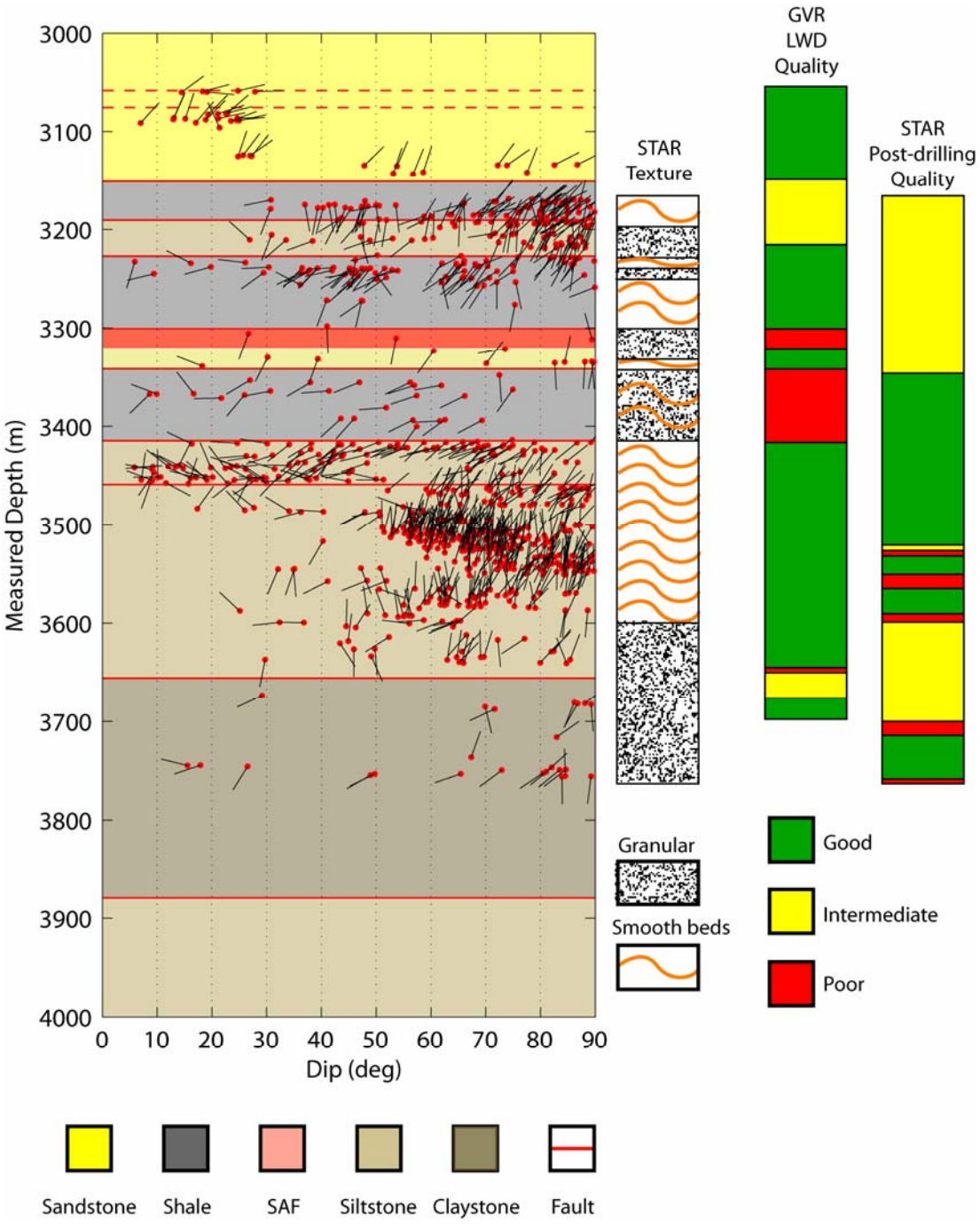

Figure 4.5: Tadpole plot showing the bedding planes determined from an analysis of the LWD azimuthal resistivity image log and the post-drilling resistivity image log. The dots mark the dip of the beds and the associated tails point in the dip direction. I also show the depth extent and quality of both image logs, in addition to the texture of the rocks visible in the post-drilling log.

The LWD log was acquired between 3050 m and 3703 m, but due to memory limitations of the tool is of lesser absolute quality than the post-drilling log between depths of 3170 m and 3765 m. In Figure 4.5 I show the quality of each log with depth and the texture of the rocks visible in the higher resolution post-drilling image log. Finally, I correlate the physical properties with the lithologic analyses of cuttings collected during drilling.

Of particular interest is identifying the location and extent of anomalous physical properties associated with the SAF. Shear zones in the pilot hole and phase 1 of drilling were identified by their anomalous physical properties: low sonic velocity, low resistivity, high gamma ray, changes in porosity, increased fracturing or abrupt changes in bedding orientations on the FMI log and increased gas emissions [Boness and Zoback, 2004; 2005]. I use the same criteria for identifying faults, although I note that many smaller faults currently remain undocumented because the resolution of the image log data is not high enough to resolve them.

Overall, the sedimentary sequence penetrated in phase 2 can be divided into three major units: an upper sandstone rich unit that was encountered at the end of phase 1 and extends down to a depth of 3150 m, the SAF zone (including the damage zone) that is between 3150 m and 3415 m, and a lower sedimentary sequence consisting largely of siltstone and claystone.

The upper sandstone-rich interval is characterized by the highest sonic velocities seen in the borehole with a compressional velocity, V_p, of between 5 km/s and 6 km/s and a shear wave velocity, V_s, of between 2.5 km/s and 3.5 km/s. The resistivity in this unit is also very high, up to 200 ohm-m. The density porosity and neutron porosity both indicate a fairly low porosity of about 5 % to 10 %. Only the LWD image log was acquired in this section so the resolution is not very high, but the beds that are visible are all dipping to the northeast (Figure 4.5). There is a short interval within this unit (shown as dashed red lines on Figure 4.4), near the top of the log, which is characterized by low velocity, high gamma, low resistivity and a high neutron porosity (indicating the presence of bound water in minerals like clay). This interval corresponds to a clay-rich shear zone that was cored at the end of phase 1. When one projects the location of the southwest fracture zone

from the surface, this is approximately the depth at which it would be intersected by the borehole.

At a depth of 3150 m, there is a very sudden decrease in the sonic velocities, a slight decrease in the resistivity, very little change in the gamma, but most significant is the increase in the neutron porosity to ~15 % while the density porosity remains about the same. The neutron log records the number of collisions with hydrogen atoms, which are usually in the pore fluids, but may also be in the bound water of some hydrous mineral phases. An analysis of cuttings over this interval reveals that it is a clay-rich shale unit. The size of the hole recorded with the caliper also increases in this interval, indicating the weak nature of the rocks. I interpret this shale to be the start of the damage zone on the southwest side of the SAF. The high resistivity indicates this unit is not very conductive and perhaps indicative of a low permeability seal on the fault zone.

At the base of this shale unit, there is a sharp decrease in velocity and a large decrease in resistivity to about 50 ohm-m (the biggest step in the resistivity log throughout phase 2). The neutron porosity also shows a slight increase to about 20 %. The image logs indicate that many beds dip to the southwest in this unit, in contrast to the shale above, and the lithology analysis of cuttings indicate that this unit is primarily a siltstone. Immediately below the siltstone is another shale unit, although the physical properties are fairly constant with the siltstone and all the beds observed dip to the southwest.

I interpret the SAF to be a 20 m wide zone starting at a depth of 3300 m. There are sharp discontinuities in all of the physical property logs, indicating the presence of a major shear zone. Over a 20 m interval, the velocities are the lowest that are seen throughout phase 2, with V_p decreasing to 3 km/s and V_s decreasing to 1.7 km/s. The gamma ray is also anomalously low and the resistivity decreases to 20 ohm-m. The most distinct change is seen in the density porosity and neutron porosity logs, which both increase dramatically. There is still some separation between the two logs, although not as pronounced as in the adjacent lithologic units, but the density porosity increases from 3 % to a maximum of 25 %, and the neutron porosity increases from 20 % to 40 %. The decrease in gamma and the lack of separation in the porosity logs may indicate less clay

minerals or that the clays have been leached away from the fault. In addition, to the physical property logs, the gas measurements indicate that this zone is very hydraulically conductive. This interval is 150 m above the projected depth of the SAF from the target earthquake locations, but a 40-arm caliper log conducted within the borehole on October 6th, 2005 indicates localized deformation of the casing at the southwestern limit of the interpreted fault core at 3300 m (Figure 4.4).

The 20 m interval below the SAF to the northeast is characterized by a sharp reversal in the physical property logs, with sharp increases in velocity, gamma and resistivity, and sharp decreases in the porosity, similar to the upper sandstone unit in phase 2. The lithologic analysis of cuttings also reflects a marked increase in the percentage of sandstone in this depth range (up to 60 %). I suggest that these physical characteristics may represent some sort of strong sandstone fault seal and interestingly a similar sandstone unit is also observed adjacent to the fault core gouge layer of the Punchbowl fault [Wilson et al., 2003].

The next deeper unit is a shale rich unit, marked by physical properties very similar to the damage zone shale on the southwestern side of the SAF, although the density and neutron porosities do appear to be slightly higher at 10 % and 25 % respectively. The bedding planes on the image logs indicate westerly dipping beds, in contrast to the southwest dipping beds in the unit above. The base of this shale shows a pronounced step increase in velocity and resistivity and I interpret this to be the extent of the fault damage zone on the northeastern side of the SAF. Figure 4.6 shows a detailed section of the logs across the fault zone, illustrating the ~20 m wide fault core embedded in a ~250 m wide damage zone.

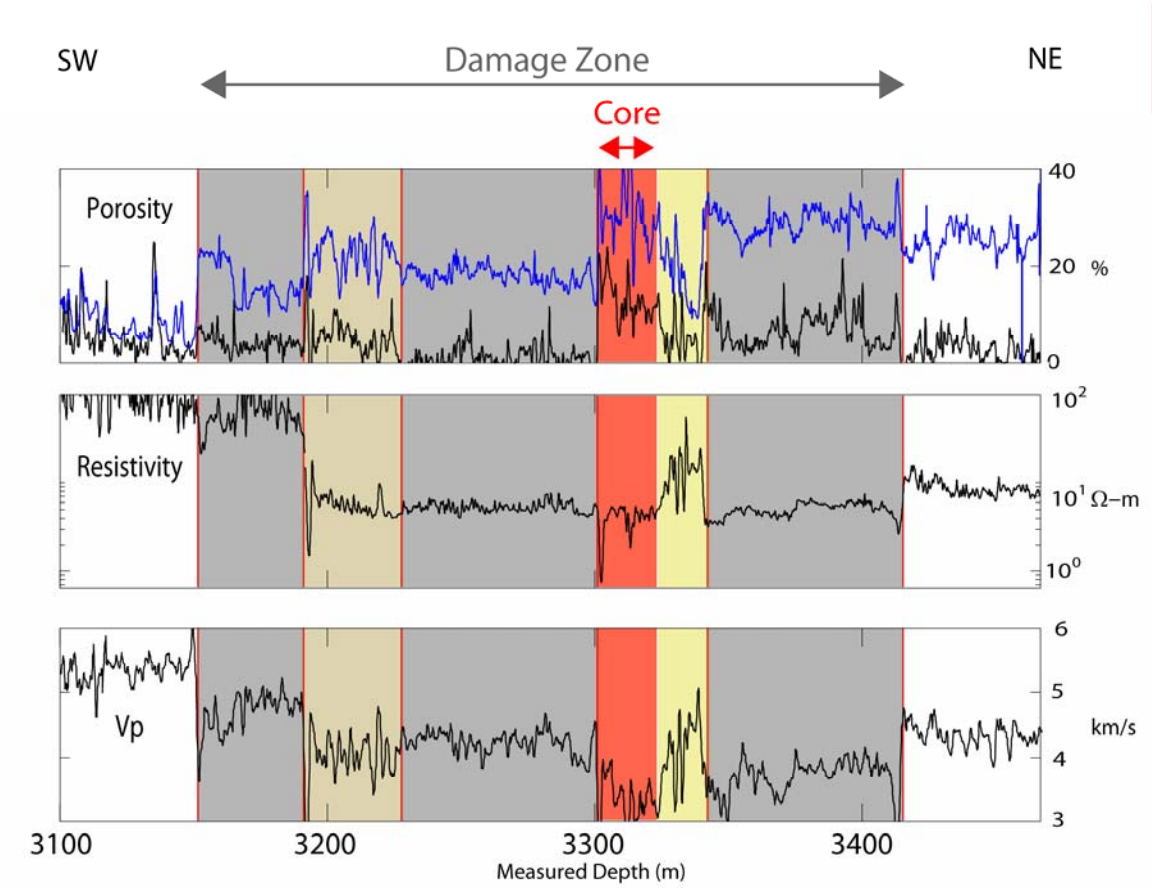

Figure 4.6: Detailed section of the logs around the ~20 m wide fault core exhibiting low velocity and high porosity, embedded in a ~250 m wide clay-rich damage zone.

On the northeastern side of the fault zone, the lithologies appear to be fairly similar, mostly siltstone and claystone, to a depth of 3880 m. From the image log analysis there does appear to be a fault at a depth of 3420 m, which separates westerly dipping beds above from northeasterly dipping beds below. Interestingly, this depth corresponds almost exactly to the projected depth of the SAF from the target earthquake locations and was the location of a magnitude 0 earthquake that occurred on May 5th, 2005 [Ellsworth et al, 2005; Zoback et al, 2005; Hickman et al., 2005]. However, other than a slight decrease in the sonic velocities, there does not appear to be any other indication of a fault zone in the physical property logs. Over this interval there is an increasing trend in the gamma ray through a more shale-rich layer. Below 3880 m, the cuttings indicate a little more sandstone and this is reflected in higher sonic velocities, with V_p between 4.5 km/s and 6 km/s, and a decrease in the neutron porosity indicating less hydrous minerals (presumably clays).

4.3 Shear velocity anisotropy

Shear wave velocity anisotropy is affected by the state of stress, lithologic controls and the presence of fault fabric in active shear zones. In Chapters 2 and 3, I use data from the pilot hole and phase 1 of SAFOD to show, that with knowledge of the formation properties, it is possible to identify stress-induced anisotropy, and therefore determine the direction of S_{Hmax}. In this section, I present data from a dipole sonic shear log that was acquired immediately after drilling of phase 2 was completed (from depths of 3050 m to 4000 m) to assess shear wave velocity anisotropy at sonic frequencies [Kimball and Marzetta, 1984; Chen, 1988; Harrison et al., 1990]. Only the dipole sonic shear measurements of high quality are considered (low minimum energy in the slow direction at the time of the fast arrival, large energy separations between fast and slow receivers). However, at this time no dispersion curve information is available and while I remove data from sections of the borehole known to be washed-out from the caliper data, I cannot rule out the possibility of borehole ovality influencing the anisotropy measurements in some places.

Figure 4.7 shows the orientation of the fast shear waves in phase 2 of SAFOD color-coded with the amount of anisotropy, overlain on the lithology. The fast directions

are fairly variable in the upper part of the log, but below a depth of 3450 m, the fast polarizations appear to be predominantly northeast. The amount of anisotropy is fairly high (between 8-10 %) over much of the log, but in the lowermost siltstone unit the anisotropy decreases to 2-5 %. In the sedimentary rocks encountered in phase 1 the anisotropy was noted to increase up to 12 % in the shale rich units but was considerably less in the sandstone layers.

In Chapter 3, I developed a theoretical model to determine the fast polarizations that should be observed in an arbitrarily oriented borehole if the fast shear polarizations are caused by aligned bedding planes. Using the bedding plane orientations observed in the image logs between depths of 3050-3750 m (Figure 4.5), I use this model to predict the theoretical polarizations for the SAFOD borehole trajectory (Figure 4.8). It is evident that the bedding will give rise to structural anisotropy that has a predominantly northwest fast polarization. However, many of the observed fast polarizations are distinctly northeast, leading us to the conclusion that the shear anisotropy in many places is stress-induced.

Of particular interest is the state of stress within and immediately adjacent to the SAF. To address this topic, I investigate the shear wave anisotropy in each lithologic unit within the damage zone and across the SAF, as identified from the physical property analysis over a depth range of 3200 m to 3500 m (Figure 4.9). I remove the shear anisotropy measurements that modeled as being structurally-controlled and suggest that the remaining observations are stress-induced and reflect the direction of S_{Hmax}. The fast polarizations in the damage zone on the southwest side of the fault zone (at shallower measured depths) indicate almost east-west fast polarizations. Within the 20 m wide core of the SAF the fast polarizations rotate locally to a north-south orientation. The polarizations immediately below the fault zone rotate back to a northeast orientation Structural anisotropy appears to be the dominant mechanism in the northeast damage zone with polarizations trending parallel to the strike of the SAF and in the lowermost siltstone unit the stress-induced fast polarizations are once again northeast-southwest.

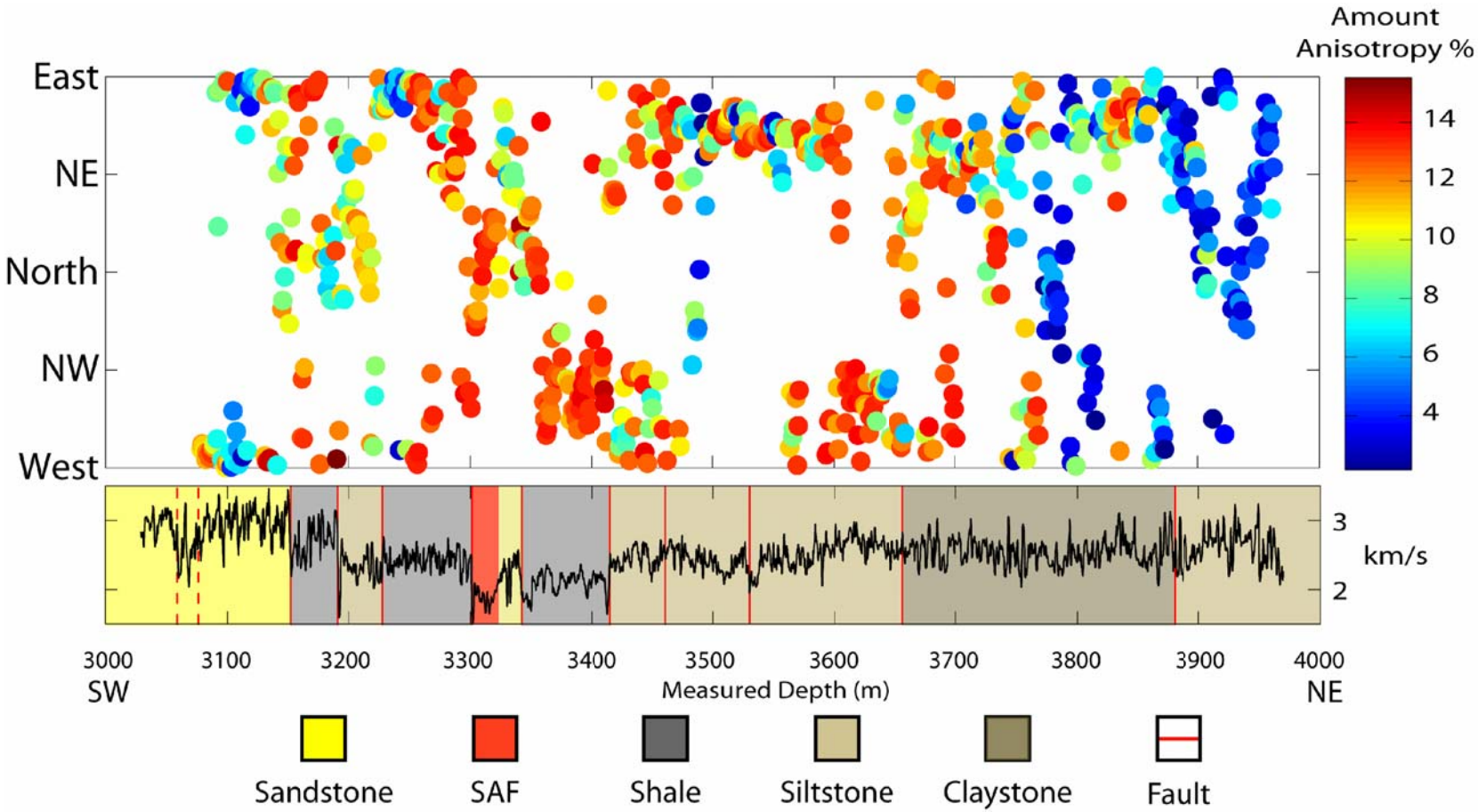

Figure 4.7: Fast polarization directions, color-coded with the amount of anisotropy, in phase 2 of SAFOD, overlain on lithology.

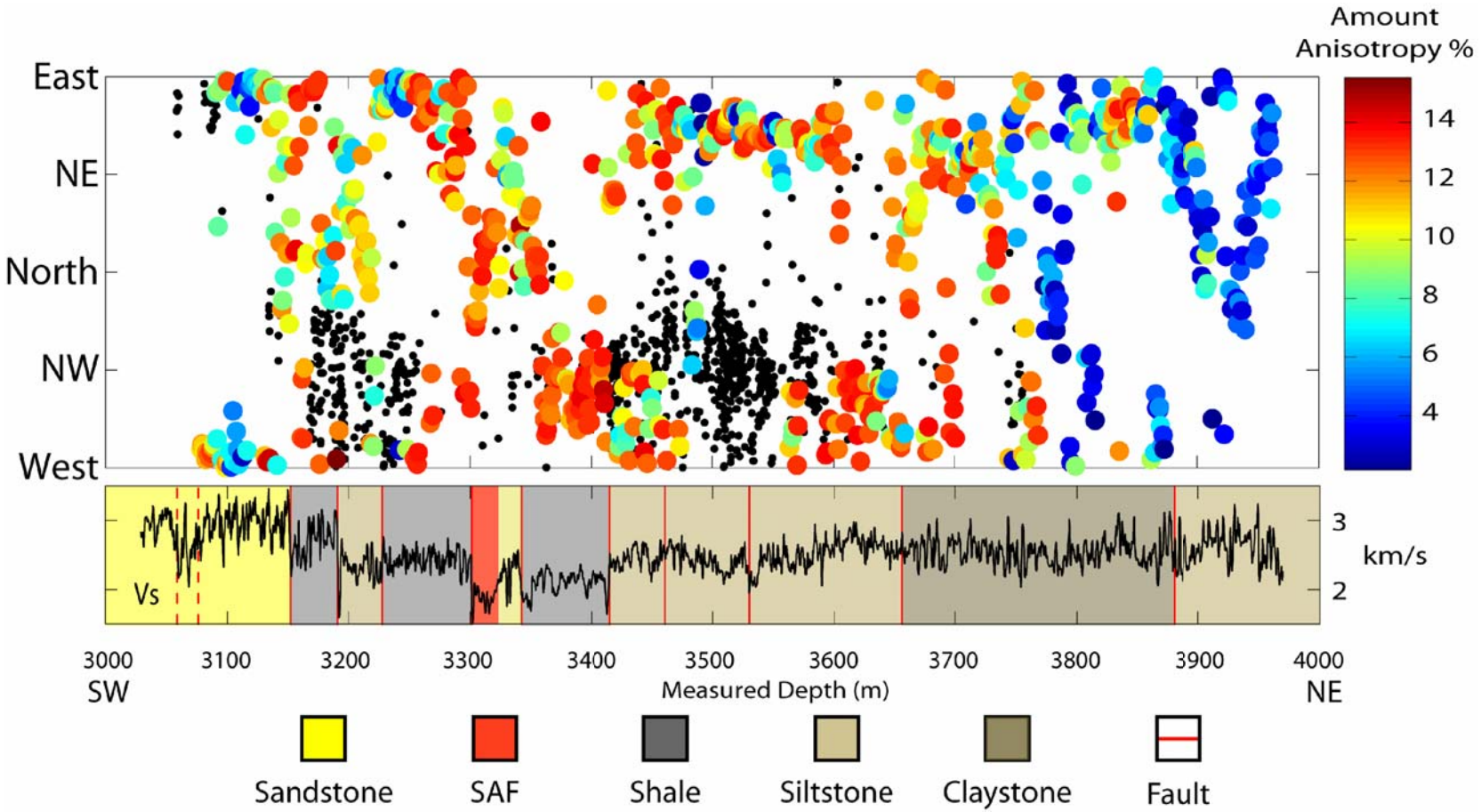

Figure 4.8: Fast polarization direction color-coded with amount of anisotropy (as in Figure 4.7), with the theoretical fast polarizations, in black, that would be observed in SAFOD if the bedding was causing the anisotropy

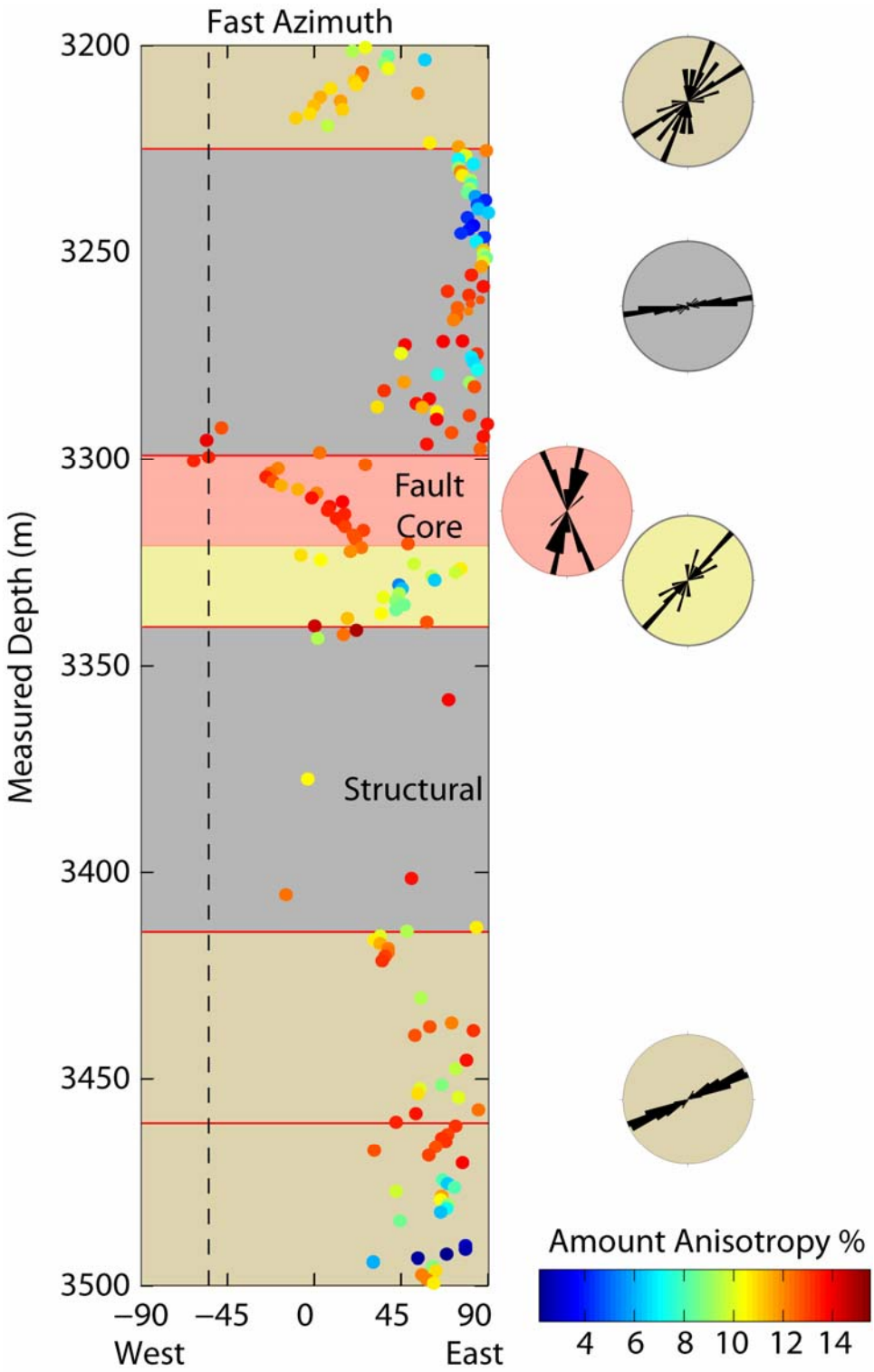

Figure 4.9: Stress-induced fast shear wave polarizations within each lithologic unit across the SAF zone, color coded with the amount of anisotropy. The dashed line indicates the apparent fast direction that would be observed in SAFOD if the anisotropy was due to a fault-parallel fabric. The rose diagrams indicate the orientation of the stress-induced fast directions in each lithologic unit.

In addition to the structural anisotropy caused by the presence of sedimentary bedding, I anticipate that the structural fabric of the SAF itself (that may not be visible on the FMI image logs) may be influencing the shear anisotropy measurements presented here. Chester and Logan [1987] documented the preferred orientation of subsidiary macroscopic faults within the exhumed Punchbowl fault to be striking northwest and almost vertical (i.e., fault-parallel). Oriented samples from the exhumed Punchbowl fault also exhibit open and sealed microfractures that increase in density toward the ultracataclasite core and show preferential orientations [Wilson et al., 2003]. The dominant set of microfractures is composed of steeply dipping northwest striking fractures that form an acute angle to the Punchbowl fault. Using the model described in Chapter 3, I also determine the apparent fast direction that would be observed for such a fault-parallel fabric and show this as the dashed line on Figure 4.9.

However, throughout the damage zone Wilson et al. [2003] also document the presence of other populations of sealed microfractures, the most notable being a group of vertical to steeply northwest dipping microfractures that have strikes perpendicular to the slip direction of the fault. Applying the forward model for such a microfracture population yield apparent fast directions for the SAFOD borehole that are northwest (-63° to -81° for a range of dips between 50° and 90°). To get apparent fast directions that correspond to the observed north-south fast directions observed with the dipole sonic in the fault core, the theoretical model predicts that the structures would have to be close to vertical and striking north-south, for which there is no evidence either at the macroscopic or microscopic scale. Thus, I believe structural anisotropy can be ruled out as a mechanism for the anomalous fast polarization directions observed within the fault core.

4.4 Discussion

Anomalous physical properties including low velocity, low resistivity and high porosity indicate that the width of the SAF core intersected by SAFOD is 20 m. This is consistent with the observed cataclasite fault cores of exhumed faults that are typically 10-100 m wide [Chester et al., 1993]. I interpret the 100-150 m wide zones of anomalous properties on either side of the core to be the damage zone consisting of highly fractured and faulted rock, also consistent with studies of exhumed faults [Chester and Logan, 1986; Chester et al., 1993; Chester et al., 2005] and only slightly wider than the ~150 m wide low velocity zone found from studies of fault zone guided waves [e.g., Li et al., 1990; Ben-Zion and Malin, 1990; 1991; Leary and Ben-Zion, 1992; Jongmans and Malin, 1995; Li et al, 1997]. The real-time lithologic analyses of cuttings indicate that the entire damage zone contains a large quantity of clay-rich material, with the exception of a narrow sandstone unit that abuts the fault core on the northeast side. This sandstone layer is hypothesized to be a fault seal and mud gas and trip gas measurements indicate the presence of underpressure to the southwest of the fault zone and overpressure on the northeast side [Zoback and Hickman, 2005]. In addition, an analysis of gases [Wiersberg and Erzinger, 2005] and elemental and stable isotope chemistry of the cuttings and core samples from SAFOD [Kirschner et al., 2005] indicate significantly different rock/fluid compositions above and below the SAF, implying the fault is acting as a barrier.

From theoretical modeling of the observed sedimentary bedding and fractures, I have shown evidence that I can differentiate between stress-induced and structurally controlled shear velocity anisotropy. By removing the fast shear polarizations that are controlled by structure, the remaining fast shear polarizations across the SAF are reflecting the state of stress (Figure 4.9). These data offer the first opportunity to document stress orientations at such a high spatial resolution across an active plate-bounding fault. Figure 4.10 is a map showing the average values of the stress-induced fast shear directions at 300 m intervals along the SAFOD trajectory and across the SAF. The mapping of stress using shear velocity anisotropy provides the first constraints at such high resolution on the strength of the SAF and the opportunity to test models such as that of Rice [1992].

Outside of the fault zone I observe stress-induced fast polarizations that correlate very well with the regional stress directions. Stress-induced fast polarization directions on the southwest side of the fault (in the pilot hole, phase 1 of SAFOD and at the top of phase 2) agree particularly well with S_{Hmax} determined from borehole breakouts [Boness and Zoback, 2004] and focal mechanism inversions [Townend and Zoback, 2004]. However, one exception is in the clay-rich interval immediately to the southwest of the fault core where I observe east-west orientations (Figure 4.9) that are not consistent with the theoretical polarizations for structural anisotropy for either the sedimentary bedding visible in the image logs or fracture populations observed in exhumed faults. However, these fast polarizations do not correlate with the regional observations of S_{Hmax} either and at this time I do not understand the significance of this result. On the northeast side of the fault core, the shear anisotropy appears to be almost entirely structural within the shale so there is no constraint on the orientation of S_{Hmax}. However, immediately below this unit within the siltstone there are a number of stress-induced polarization directions that correlate very well with regional S_{Hmax} orientations at a high angle to the fault plane (Figure 4.9).

The fast directions within the core of the SAF indicate a localized rotation of S_{Hmax} to a more acute angle to the fault than in the adjacent damage zone and surrounding crust. These measurements of stress-induced fast directions show the orientation of S_{Hmax} exhibits a sudden step at the southwest boundary of the fault core from being almost east-west in the southwest damage zone to an angle of 21° to the strike of the SAF. This is also where localized deformation of the casing is observed in the 40-arm caliper logs. The stress-induced fast polarizations then show a systematic rotation through the fault core to the northeast, becoming consistent with the regional stress directions at the northeastern boundary of the fault core to an angle of 75° to the SAF.

The observation of a stress rotation in the fault core relative to the surrounding crust is consistent with the proposed models of Rice [1992] and Chery et al. [2004] consisting of a narrow fault core that is weak in a Coulomb sense. From frictional faulting theory, the angle that S_{Hmax} makes to the trace of the fault is given by $45 - \phi/2$, where $\phi = \arctan(\mu)$. Laboratory experiments indicate that the coefficient of friction, μ, is

in the range of 0.6 – 0.9 for most crustal rocks. This would predict S_{Hmax} to be at an angle of 25-30° to the fault, which is substantially lower than the high angles observed both regionally and in this study outside of the fault core. The weak fault model predicts that within the fault core, either increased pore pressure of the inherent weakness of the fault zone material will cause S_{Hmax} to rotate to 45° to the fault strike (Byerlee and Savage, 1992). Interestingly, the rotation I observe is actually to a more acute angle than 45°.

These results complement the few direct measurements of stress made in SAFOD: a hydrofracture experiment at the end of phase 1, 300 m to the southwest of the fault core, indicates an elevation in the magnitude of S_{hmin} [Zoback and Hickman, 2005], significantly higher than a measurement made at the bottom of phase 2, 700 m to the northeast of the fault core. The increase in the magnitude of S_{hmin} just in the vicinity of the fault core is consistent with the model of a weak fault with elevated stress magnitudes (necessary to satisfy the conditions of mechanical equilibrium across the fault zone boundary).

Although there appears to be a contrast in pore pressure across the fault zone, high fluid pressures were not observed within the fault core during drilling. The absence of high pore pressure would imply that the fault is weak relative to the surrounding crust due to inherent material strength. However, laboratory analyses reveal that the fault zone material has a fairly high frictional strength, with a coefficient of friction in the range of $\mu = 0.45 - 0.55$ [Tembe et al., 2005]. However, the gradual rotation of S_{Hmax} across the fault core implies that the active fault plane may be extremely narrow and located at the southwest extent of the fault core with the rheology becoming consistently stronger to the northeast. The cuttings analyzed in the laboratory experiments were samples collected during drilling and it is probable that mixing occurred as the cuttings traveled up the borehole, so the laboratory measurements are probably not representative of the very narrow fault gouge layer. Core that will be obtained in 2007 across the fault zone should provide further constraints on the internal structure and variation in mechanical properties of the fault zone.

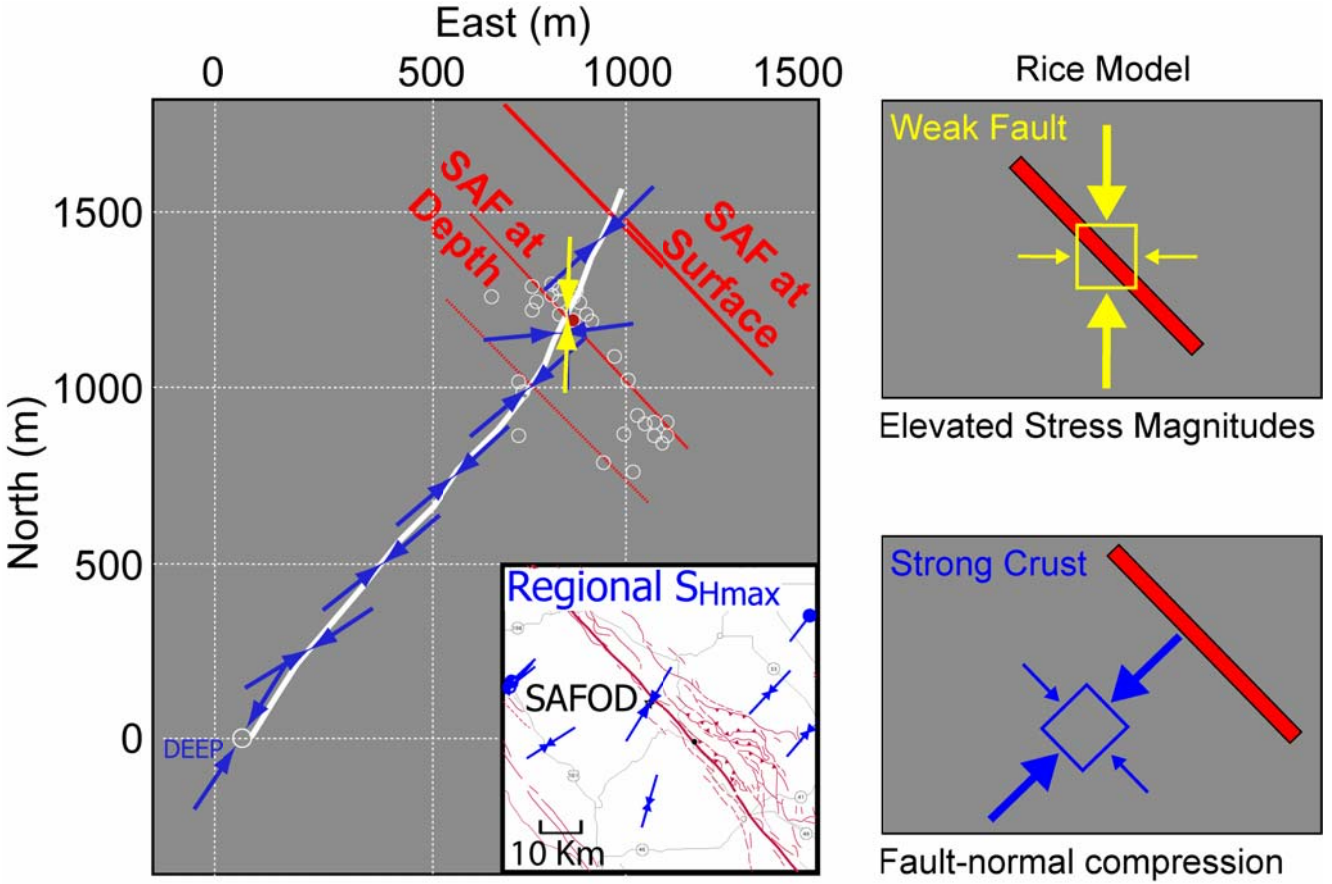

Figure 4.10: Map showing stress-induced fast shear wave polarizations at ~300 m intervals along the SAFOD trajectory, profiling the orientation of S_{Hmax} across the SAF. In the crust adjacent to the fault zone the orientations are consistent with a strong crust but within the narrow fault core there is a localized rotation of S_{Hmax} consistent with the hypothesis of a weak fault in a strong crust.

4.5 Conclusions

In this paper I have identified the SAF from an integrated analysis of physical properties to be a 20 m wide zone, surrounded by a damage zone of approximately 100-150 m on either side. The location of the San Andreas has also been confirmed with a recent caliper log that indicates localized deformation of the casing in this exact interval.

From theoretical modeling of the observed sedimentary bedding and fractures, I have shown evidence that I can differentiate between stress-induced and structurally controlled shear velocity anisotropy. By removing the fast shear polarizations that are structurally-controlled, I have examined the orientation of S_{Hmax} along a profile across the SAF. I find that S_{Hmax} remains at a high angle to the fault zone in the crust, except within the very narrow core of the fault where the stress rotates to approximately north-south. I conclude that the SAF at Parkfield is a narrow zone of active deformation with a localized stress rotation due to its weak rheology relative to the strong crust, consistent with models of Coulomb faulting.

Acknowledgements

I would like to acknowledge the many members of the SAFOD science team with whom I worked to develop a community model of the structure and composition of the San Andreas Fault through an integrated analysis of data collected in phase 2 of SAFOD. Although this work has yet to be published and is therefore written in the first person here, I would like to recognise Mark Zoback for his significant role as my advisor. This work was supported by NSF grant EAR-0323938-001.

References

Aki, K., and Lee, W. H. K., 1976, Determination of three-dimensional velocity anomalies under a seismic array using P-arrival times from local earthquakes: 1. A homogeneous initial model: *J. Geophys. Res*., **81**, 4381-4399.

Ben-Zion, Y., and Malin, P. E., 1990, Fault zone head waves in the San Andreas fault zone near Parkfield, California: *Eos Trans. AGU*, **71**, 1474.

Ben-Zion, Y., and Malin, P. E., 1991, San Andreas fault zone head waves near Parkfield, California: *Science*, **251**, 1592-1594.

Boness, N. L., and Zoback, M. D., 2004, Stress-induced seismic velocity anisotropy and physical properties in the SAFOD Pilot Hole in Parkfield, CA: *Geophys. Res. Lett*., **31**, L15S17.

Boness, N. L., and Zoback, M. D., 2005, Fine-scale controls on shear velocity anisotropy in the San Andreas Fault Observatory at Depth: *Geophysics*, in press.

Brune, J. N., Brown, S., and Johnson, P. A., 1993, Rupture mechanism and interface separation in foam rubber models of earthquakes: a possible solution to the heat flow paradox and the paradox of large overthrusts: *Tectonophysics*, **218**, 59-67.

Byerlee, J.D., and Savage, J.C., 1992, Coulomb plasticity within the fault zone: *Geophys. Res. Lett*., **19**, 2341–2344.

Chen, S. T., 1988, Shear-wave logging with dipole sources: *Geophysics*, **53**, 659-667.

Chery, J., Zoback, M. D., and Hickman, S., 2004, A mechanical model of the San Andreas fault and SAFOD pilot hole stress measurements: *Geophys. Res. Lett*., **31**, L15S13.

Chester, F. M., Evans, J. P., and Biegel, R. L., 1993, Internal structure and weakening of the San Andreas fault: *J. Geophys. Res*., **98**, 771-786.

Chester, F. M., and Logan, J. M., 1986, Implications for mechanical properties of brittle faults from observations of the Punchbowl fault, California: *Pure Appl. Geophys*., **124**, 79-106.

Chester, J., Chester, F. M., and Kronenberg, A. K., 2005, Fracture energy of the Punchbowl fault, San Andreas system: *Nature*, **437**, 133-136.

Eberhart-Phillips, D. M., and Michael, A. J., 1993, Three-dimensional velocity structure, seismicity, and fault structure in the Parkfield region, central California: *J. Geophys. Res*., **98**, 15737-15758.

Eberhart-Phillips, D. M., Labson, V. F., Stanley, W. D., Michael, A. J., and Rodrigues, B. D., 1990, Preliminary velocity and resistivity models of the Loma Prieta earthquake region: *Geophys. Res. Lett*., **17**, 1235-1238.

Eberhart-Phillips, D. M., Stanley, W. D., Rodrigues, B. D., and Lutter, W. J., 1995, Surface seismic and electrical methods to detect fluids related to faulting: *J. Geophys. Res*., **100**, 12919-12936.

Ellsworth, W. L., 1975, Bear Valley, California earthquake sequence of February-March, 1972: *Bull. Seismol. Soc. Am*., **65**, 483-506.

Ellsworth, W. L., Hickman, S., Zoback, M., Davis, E., Gee, L., Huggins, R., Krug, R., Lippus, C., Malin, P., Neuhauser, D., Paulsson, B., Shalev, E., Vajapeyam, B., Weiland, C., Zumberge, M., 2005, Observing the San Andreas Fault at depth: *Eos Trans. AGU*, **86**(52), Fall Meet. Suppl., Abstract T24B-04.

Evans, J. P., and Chester, F. M., 1995, Fluid-rock interaction in faults of the San Andreas system: Inferences from San Gabriel fault rock geochemistry and microstructures: *J. Geophy. Res*., **100**, 13007-13020.

Feng, R., and McEvilly, T. V., 1983, Interpretation of seismic reflection profiling data for the structure of the San Andreas fault zone: *Bull. Seismol. Soc. Am*., **73**, 1701-1720.

Griscom, A., and Jachens, R. C., 1990, Tectonic implications of gravity and magnetic models along east-west seismic profiles across the Great Valley near Coalinga, in Rymer, M. J., and Ellsworth, W. L., eds., *The Coalinga, California earthquake of May 2, 1983*: U. S. Geol. Survey Prof. Pap., **1487**, Reston, VA, 69-78.

Harrison, A. R., Randall, C. J., Aron, J. B., Morris, C. F., Wignall, A. H., and Dworak, R. A., 1990, Acquisition and analysis of sonic waveforms from a borehole monopole and dipole source for the determination of compressional and shear speeds and their relation to rock mechanical properties and surface seismic data: *SPE Annual Technical Conference and Exhibition*, New Orleans, Paper SPE 20557.

Healy, J., and Peake, L., 1975, Seismic velocity structure along a section of the San Andreas fault near Bear Valley, California: *Bull. Seismol. Soc. Am*., **65**, 1177-1197.

Hickman, S. H., and Zoback, M. D., 2004, Stress orientations and magnitudes in the SAFOD pilot hole: *Geophys. Res. Lett*., **31**, L1S12.

Hickman, S. H., Zoback, M. D., and Ellsworth, W. L., 2005, Structure and composition of the San Andreas Fault zone at Parkfield: initial results from SAFOD phases 1 and 2: *Eos Trans. AGU*, **86**(52), Fall Meet. Suppl., Abstract T23E-05.

Hole, J. A., Catchings, R. D., St. Clair, K. C., Rymer, M. J., Okaya, D. A., and Carney, B. J., 2001, Steep-dip seismic imaging of the shallow San Andreas fault near Parkfield: *Science*, **294**, 1513-1515.

Jachens, R. C., 2002, Three-dimensional model based on geophysics of the San Andreas Fault Observatory at Depth (SAFOD), near Parkfield, Calif.: http://wrgis.wr.usgs.gov/docs/gump/meghan/parkfield/parkfield.html.

Jongmans, D., and Malin, P. E., 1995, Microearthquake S-wave observations from 0 to 1 km in the Varian well at Parkfield, California: *Bull. Seismol. Soc. Am*., **85**, 1805-1820.

Kimball, C. V., and Marzetta, T. M., 1984, Semblance processing of borehole acoustic array data: *Geophysics*, **49**, 264-281.

Kirschner, D., Evans, J., Chester, J., Chester, F., Solum, J., and Moore, D., 2005., Elemental and stable isotope chemistry of cuttings and core samples from SAFOD drill hole: *Eos Trans. AGU*, **86**(52), Fall Meet. Suppl., Abstract T21A-0452.

Lachenbruch, A. H., and Sass, J. H., 1973, Thermo-mechanical aspects of the San Andreas Fault system, in *Proceedings of Tectonic problems of the San Andreas Fault system*: Stanford University Publications, Geological Sciences, **13**, 192-205.

Lachenbruch, A. H., and Sass, J. H., 1980, Heat flow and energetics of the San Andreas fault zone: *J. Geophys. Res*., **85**, 6185-6222.

Leary, P., and Ben-Zion, Y., 1992, A 200-m wide fault zone low velocity layer on the San Andreas fault at Parkfield: results from analytic waveform fits to trapped wave groups: *Seis. Res. Lett*., **63**, 62.

Li, Y-G., and Leary, P., 1990, Fault zone trapped seismic waves: *Bull. Seismol. Soc. Am*., **80**, 1245-1274.

Li, Y-G., Ellsworth, W. L., Thurber, C. F., Malin, P. E., and Aki, K., 1997, Fault-zone guided waves from explosions in the San Andreas fault and Parkfield and Cienega Valley, California: *Bull. Seismol. Soc. Am*., **87**, 210-221.

Li, Y-G., Leary, P. C., Aki, K., and Malin, P. E., 1990, Seismic trapped modes in the Oroville and San Andreas fault zones: *Science*, **249**, 763-765.

Lin, C. H., and Roecker, S. W., 1997, Three-dimension P-wave velocity structure of the Bear-Valley region of central California: *Pure Appl. Geophys*., **149**, 667-688.

McBride, J. H., and Brown, L. D., 1986, Reanalysis of the COCORP deep seismic reflection profile across the San Andreas Fault, Parkfield, California: *Bull. Seismol. Soc. Am*., **76**, 1668-1686.

Michael, A. J., and Eberhart-Phillips, D., 1991, Relations among fault behavior, subsurface geology, and three-dimensional velocity models: *Science*, **253**, 651-654.

Michelini, A., and McEvilly, T. V., 1991, Seismological studies at Parkfield. I. Simultaneous inversion for velocity structure and hypocenters using cubic B-splines parameterization: *Bull. Seismol. Soc. Am*., **81**, 524-552.

Mount, V. S., and Suppe, J., 1987, State of stress near the San Andreas Fault; implications for wrench tectonics: *Geology*, **15**, 1143-1146.

Nadeau, R. M., Foxall, W., and McEvilly, T. V., 1995, Clustering and periodic recurrence of microeathquakes on the San Andreas fault at Parkfield, California: *Science*, **267**, 503-507.

Pavoni, N., 1973, A structural model for the San Andreas fault along the northeast side of the Gabilan Range, in *Proceedings of Tectonic Problems of the San Andreas Fault System*: Stanford University Publications, Geological Sciences, **13**, 259-267.

Provost, A.-S., and H. Houston, 2001, Orientation of the stress field surrounding the creeping section of the San Andreas fault: Evidence for a narrow mechanically-weak fault zone: *J. Geophys. Res*., **106** , 11,373-11,386.

Rice, J. R., 1992, Fault stress states, pore pressure distributions, and the weakness of the San Andreas Fault, in Evans, B., and Wong, T., eds., *Fault mechanics and transport properties of rocks*: Academic Press, San Diego, 475-503.

Rymer, M. J., Catchings, R. D., Goldman, M. R., Fuis, G. S., Huggins, R., Lippus, C., and Hole, J. A., 1999, Structural Complexity in the San Andreas fault zone as revealed by high-resolution seismic reflection and refraction profiling near Parkfield, California: *Eos Trans. AGU*, **80**, F706.

Sleep, N. H., and Blanpied, M. L., 1992, Creep, compaction and the weak rheology of major faults: *Nature*, **359**, 687-692.

Tembe, S., Lockner, D. A., Solum, J. G., Morrow, C. A., Wong, T., and Moore, D. E., 2005, Strength of the San Andreas Fault zone: insight from SAFOD cuttings and core: *Eos Trans. AGU*, **86**(52), Fall Meet. Suppl., Abstract T24B-03.

Thurber, C., Roecker, S., Ellsworth, W. L., Chen, Y., Lutter, W., and Sessions, R., 1997, Three-dimensional seismic image of the San Andreas fault in the northern Gabilan range, central California: Evidence for fluids in the fault zone: *Geophys. Res. Lett*., **24**, 1591-1594.

Thurber, C., Roecker, S., Lutter, W., and Ellsworth, W. L., 1996, Imaging the San Andreas fault with explosions and earthquake sources: *Eos Trans. AGU*, **77**, 45, 57 and 58.

Townend, J., and Zoback, M. D., 2004, Regional tectonic stress near the San Andreas fault in central and southern California: *Geophys. Res. Lett*., **31**, L15S11.

Unsworth, M. J., and Bedrosian, P. A., 2004, Electrical resistivity structure at the SAFOD site from magnetotelluric exploration: *Geophys. Res. Lett*., **31**, L12S05.

Unsworth, M. J., Bedrosian, P., Eisel, M., Egbert, G. D., and Siripunvaraporn, W., 2000, Along strike variations in the electrical structure of the San Andreas Fault at Parkfield, California: *Geophys. Res. Lett*., **27**, 3021-3024.

Unsworth, M. J., Egbert, G. D., and Booker, J. R., 1999, High-resolution electromagnetic imaging of the San Andreas Fault in Central California: *J. Geophys. Res*., **104**, 1131-1150.

Unsworth, M. J., Malin, P. E., Egbert, G. D., and Booker, J. R., 1997, Internal structure of the San Andreas Fault at Parkfield, California: *Geology*, **25**, 359-362.

Walter, A. W., and Mooney, W. D. , 1982, Crustal structure of the Diablo and Gabilan ranges, central California: a reinterpretation of existing data: *Bull. Seismol. Soc. Am*., **72**, 1567-1590.

Wesson, R. L., 1971 , Travel-time inversion for laterally inhomogeneous crustal velocity models: *Bull. Seismol. Soc. Am*., **61**, 729-746.

Wiersberg, T., and Erzinger, J., 2005, Real-time fluid and gas monitoring during drilling of the SAFOD main hole in Parkfield, CA.: *Eos Trans. AGU*, **86**(52), Fall Meet. Suppl., Abstract T23E-02.

Williams, C. F., Grubb, F. V., and Galanis, Jr., S. P., 2004, Heat flow in the SAFOD pilot hole and implications for the strength of the San Andreas Fault: *Geophys. Res. Lett*., **31**, L1S14.

Wilson, J. E., Chester, J. S., and Chester, F. M., 2005, Microfracture analysis of fault growth and wear processes, Punchbowl Fault, San Andreas system, California*: J. Struc. Geol*., **25**, 1855-1873.

Zoback, M. D., and Hickman, S., 2005, Preliminary observations of stress and fluid pressure in and near the San Andreas Fault at depth in the SAFOD boreholes: *Eos Trans. AGU*, **86**(52), Fall Meet. Suppl., Abstract T21A-0438.

Zoback, M. D., Hickman, S., and Ellsworth, W., 2005, Overview of SAFOD phases 1 and 2: drilling, sampling and measurements in the San Andreas Fault zone at seismogenic depth: *Eos Trans. AGU*, **86**(52), Fall Meet. Suppl., Abstract T23E-01.

Zoback, M. D., Zoback, M. L., Mount, V. S., Suppe, J., Eaton, J. P., Healy, J. H., Oppenheimer, D., Reasenberg, P., Jones, L., Raleigh, C. B., Wong, I. G., Scotti, O., and Wentworth C., 1987, New evidence on the state of stress of the San Andreas fault system: *Science*, **238**, 1105-1111.

Chapter 5

Mapping stress and structurally-controlled crustal shear velocity anisotropy in California.

Abstract

We present shear velocity anisotropy data from crustal earthquakes in California and demonstrate that with careful quality control procedures, it is possible to discriminate structural anisotropy (polarization of the shear waves along the fabric of major active faults) from stress-induced anisotropy (polarization parallel to the maximum horizontal compressive stress). Stress directions from seismic stations located near (but not on) the San Andreas Fault indicate that the maximum horizontal compressive stress is at a high angle to the strike of the fault implying that it is mechanically weak and slipping at low levels of shear stress. In contrast, seismic stations located directly upon one of the major faults indicate that shear deformation of the rock adjacent to the fault has significantly altered the elastic properties of the crust inducing shear wave polarizations parallel to the fault plane.

The material in this chapter has appeared in Boness, N. L., and Zoback, M. D., 2005, Mapping stress and structurally-controlled shear velocity anisotropy in California: *Geology*, submitted.

5.1 Introduction

It has been known for the past 25 years that carefully used earthquake, wellbore and geologic data can be used to map the directions and relative magnitudes of in situ horizontal principal stresses in the Earth's crust [Zoback and Zoback, 1980; Zoback and Zoback, 1991; Zoback, 1992] and a global data base of more than 10,000 crustal stress indicators, the World Stress Map, is now available [Zoback et al., 1989; The World Stress Map].

In this paper, we present shear velocity anisotropy data from local earthquake sources as an independent tool to analyze the state of stress close to active faults and in geographic regions where other types of stress measurements are lacking. We show that in the crust adjacent to the San Andreas Fault (SAF) and other major fault zones in southern California, the fast polarization direction of shear waves reflects the local direction of the maximum horizontal compressive stress, S_{Hmax}. In contrast, shear waves traveling up through major active fault zones are polarized by the structural fabric of the fault zone, sub-parallel to the strike of the fault, indicating that the physical properties of major active faults are intrinsically different from those of the adjacent crust. We use data from the Southern California Seismic Network (SCSN) and Northern California Seismic Network (NCSN), with an emphasis on southern California, as a case study to illustrate the reliability of our method. California is a good place to showcase this method because there are many independent stress measurements, the tectonic structures are well documented, and the direction of S_{Hmax} is, in general, at a high angle to the faults, allowing us to differentiate between the two mechanisms.

Numerous examples of seismic anisotropy in the upper crust have been documented in the literature over the last twenty five years since it was first observed using microearthquakes [Crampin, *et al*., 1980]. The mechanisms that cause shear waves to split into a fast and slow component include: dilatancy of microcracks due to stress [Crampin, 1991], preferential closure of fractures in an anisotropic stress field [Boness and Zoback, 2004], aligned macroscopic fractures associated with regional tectonics [Mueller, 1991; Liu *et al*., 1993], sedimentary bedding planes [Alford, 1986; Lynn and Thomsen, 1990], and the alignment of minerals or grains [Sayers, 1994; Johnston and

Christensen, 1995; Hornby, 1998]. These mechanisms can be divided into two major categories: stress-induced anisotropy and structural anisotropy (Figure 5.1). Stress-induced shear anisotropy is the result of S_{Hmax} causing microcracks to open and/or pre-existing fractures at all scales to close, generating a fast direction parallel to S_{Hmax}. Stress-induced anisotropy is observed in the upper crust and the effect decreases with depth as the confining pressure increases, closing fractures in all orientations. Evidence recorded in the San Andreas Fault Observatory at Depth (SAFOD) indicates that stress-induced anisotropy is still more than 3 % in granitic rocks in California at a depth of about 3 km [Boness and Zoback, 2005]. Structural anisotropy occurs when aligned macroscopic features such as fault zone fabric or sedimentary bedding planes polarize the shear waves with a fast direction in the plane of the feature. With knowledge of the structural elements in a region, including major faults, it is possible to distinguish between stress-induced and structural anisotropy [Zinke and Zoback, 2000], and therefore determine the orientation of S_{Hmax}. However, measurements of shear velocity anisotropy often sample the combined effects of stress and structure, so it is important to know whether the splitting is caused by stress, structure, or a combination of both mechanisms. The delay time is much harder to quantify than the polarization, as the delay is cumulative but the fast direction of the shear waves is much more robust as it is mostly dependent on the last anisotropic medium the wave passes through [e.g., Crampin, 1991]. This implies that the fast polarization observed at surface seismometers is mostly generated along the last portion of the ray path.

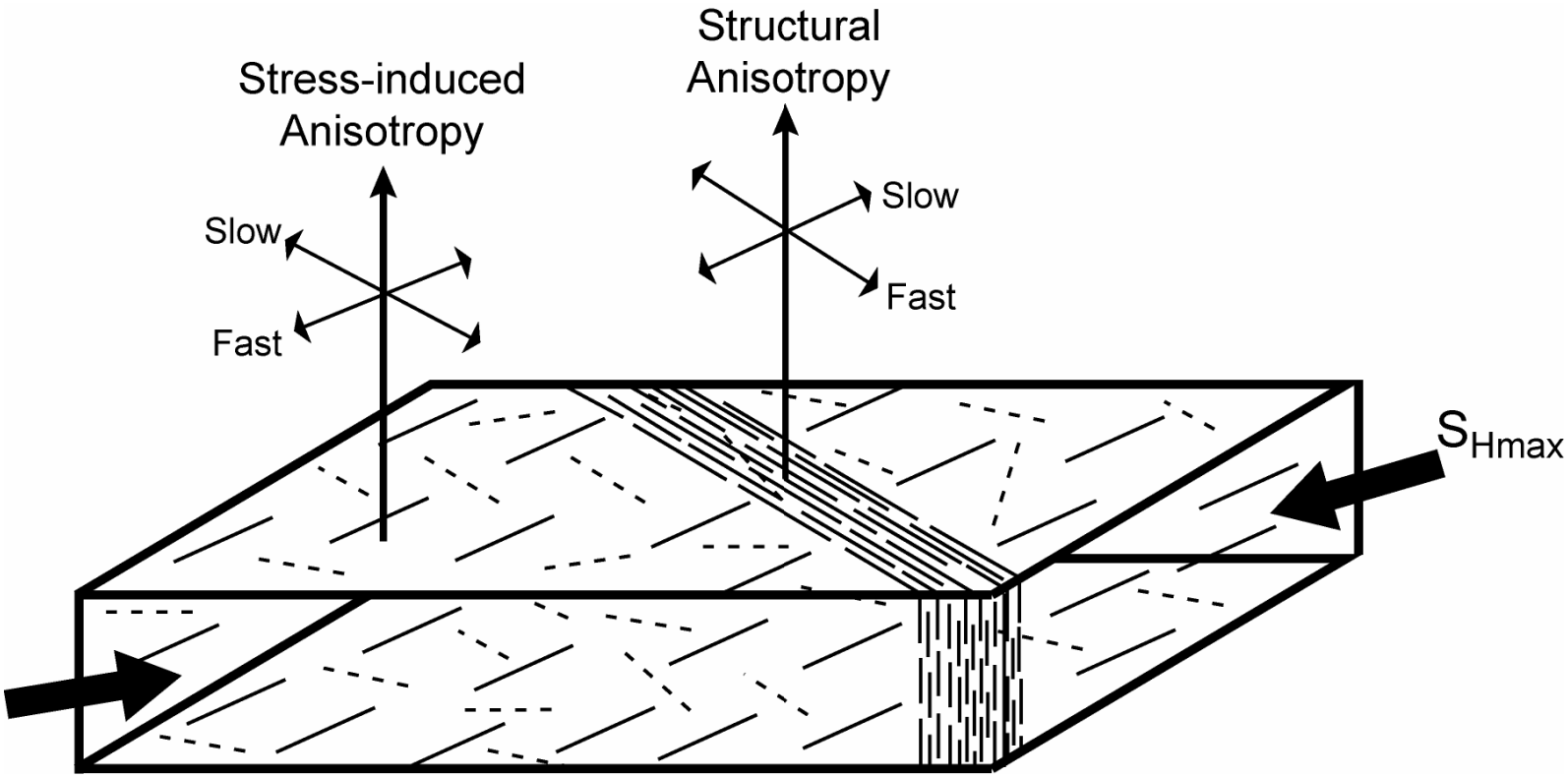

Figure 5.1: Schematic figure illustrating stress-induced anisotropy in the crust adjacent to the fault zone where the vertically propagating shear waves are polarized with a fast direction parallel to S_{Hmax} due to the preferential closure of fractures (dashed lines), and structural anisotropy of the shear waves inside a fault zone with a fast direction parallel to the fault fabric.

5.2 Methodology

We have devised a quality control procedure to measure shear wave splitting using microearthquakes recorded on three-component seismic stations that minimizes the scatter in the data and, with careful consideration of ray paths and local geology, allows one to determine if the observed anisotropy is stress-induced or structural. For each station, we search the earthquake catalogue for events that are above 15 km depth to isolate shear anisotropy in the brittle crust. We only consider earthquakes within a cone under the station up to a maximum incidence angle of 40° within the shear wave window [Nuttli, 1961; Booth and Crampin, 1985], to minimize the likelihood of contamination from converted phases. We then correct for instrument response and filter each event individually to ensure the best signal-to-noise ratio, using a bandpass filter with a low limit of 1 Hz and a high limit in the range of 5-15 Hz. We keep only data with a signal to noise ratio greater than 3:1 and visually inspect each seismogram and the corresponding particle motion plots to establish if the shear wave arrivals are impulsive enough to be picked with confidence to within two increments of the sampling frequency.

Using only the highest quality data, we measure the shear wave splitting of each event at the station. We determine the anisotropy between the shear waves observed on the two horizontal components, because we expect waves propagating within the shear wave window to refract to near vertical propagation in the upper crust. The technique we use to determine the shear wave splitting combines covariance matrix decomposition [Silver and Chan, 1991] with cross-correlation [Bowman and Ando, 1987]. The covariance matrix of the horizontal shear wave particle motion is rotated about the direction of propagation in increments of one degree from -90 to 90° and over delay times between 0 and 50 ms in increments of the sampling frequency. If anisotropy exists, the fast direction and delay time that best linearizes the particle motion is determined by minimizing the second eigenvalue. To quantify the accuracy of the measurement we also compute the degree of rectilinearity [Jurkevics, 1988] from the ratio of the two non-zero eigenvalues and only include measurements with a degree of linearity greater than 0.8 (1 being perfectly linear]. After correcting for the anisotropy, the rotated waveforms should have similar pulse shapes, so we use the maximum cross-correlation coefficient of the

rotated waveforms to confirm that the seismograms have been rotated into the fast and slow polarization directions. We discard any measurement that has a cross-correlation coefficient of less than 0.7. In addition, we only report the fast polarization direction if the cross-correlation technique yields a fast polarization within ± 10° of the covariance matrix measurement.

After the fast shear polarizations have been determined for all earthquakes at a given station, Fischer statistics [Fischer, *et al*., 1987] are used to compute the mean orientation of the fast shear waves. If the azimuthal standard deviation is less than 20° we believe the fast direction is well constrained and probably contains valuable information about either stress or structure. In contrast, a standard deviation of greater than 20° indicates a high level of scatter in the data and probably indicates a mix of mechanisms causing the anisotropy.

5.3 Results

We apply this method to data from 84 three-component stations in the SCSN and NCSN and achieve a well-constrained mean fast direction with a standard deviation of less than 20° at 62 stations (Figures 5.2 and 5.3). The rose diagrams in Figures 5.2 and 5.3 are the measurements made at each station and the associated numbers indicate the number of good measurements that complied with our quality control criteria out of the total number of earthquakes analyzed at the station. The number of earthquakes analyzed at each station was in general much higher than in typical shear wave splitting studies, with more than 100 earthquakes analyzed at 30 of the stations. Overall, the stations located on major faults exhibit a mean fast direction that is parallel to structure (Figure 5.2), whereas stations located in the adjacent crust tend to exhibit a fast direction at a high angle to the structure (Figure 5.3). There are 22 stations where the standard deviation was more than 20°, which we consider to be the result of multiple mechanisms affecting the anisotropy (diamonds in Figure 5.2b). For all of the stations we aim to get a distribution of earthquakes within the shear wave window at a range of back azimuths (although this is dependent on the position of the station relative to faults where the earthquakes occur). We present the earthquake data and individual shear wave splitting measurements for

three stations (shown as the white stations on Figures 5.2b and 5.3) as examples of stress-induced, structural and mixed anisotropy observations (Figure 5.4). The majority of earthquakes are between depths of 5 and 10 km, although stations located on major faults have a more radial coverage of earthquakes, whereas many of the earthquakes analyzed at the off-fault stations have a similar back-azimuth due to the location of the station with respect to nearby faults.

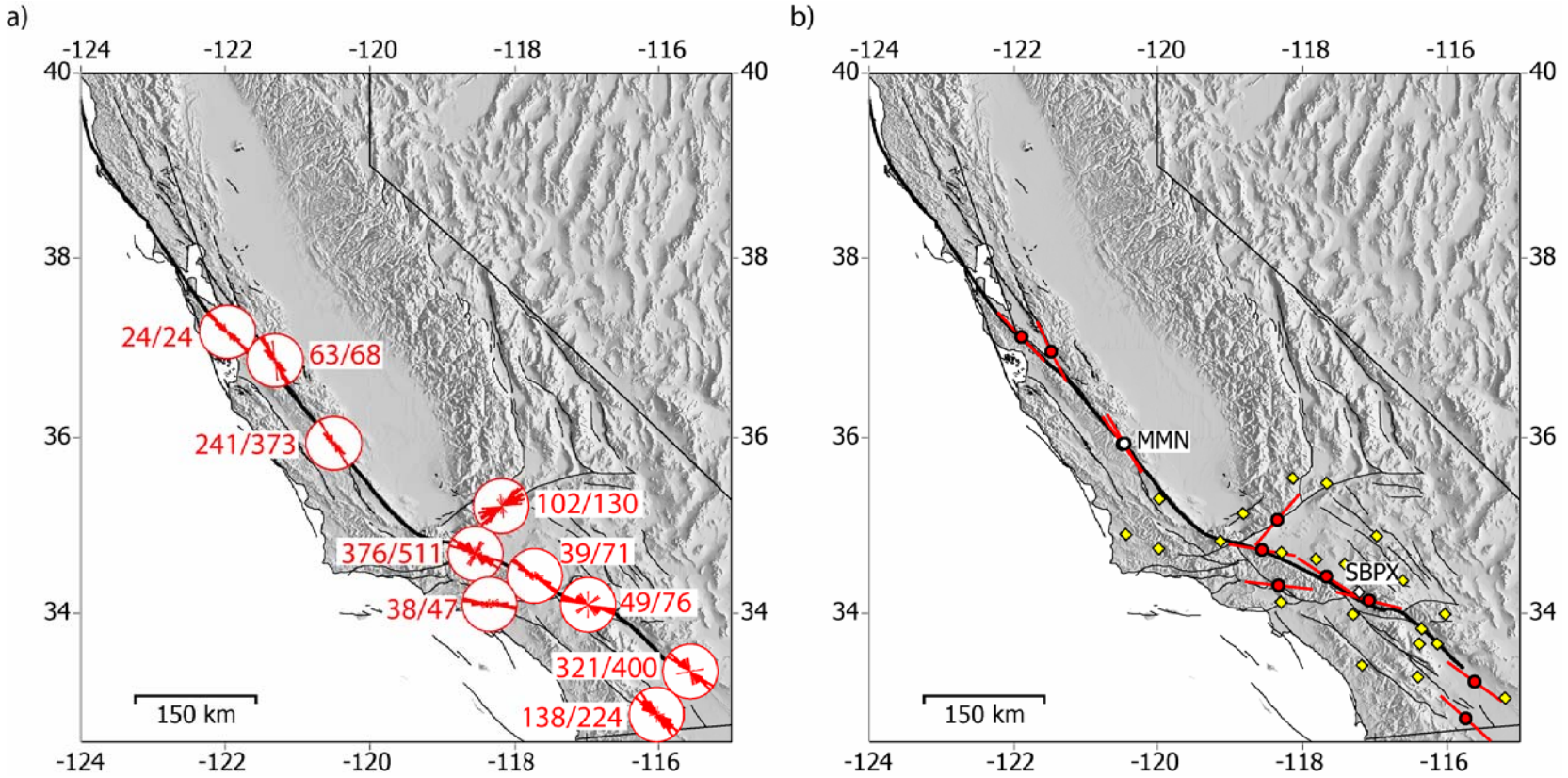

Figure 5.2: Map of California showing that stations located on major faults exhibit structural anisotropy with fast shear polarizations parallel to the structural fabric. a) Rose diagrams showing the fast polarizations observed at each station with a standard deviation of less than 20°. The corresponding numbers refer to the number of good quality measurements out of the total number of earthquakes analyzed. b) The mean fast polarization as indicated by the red lines for stations with a Fischer standard deviation of less than 20°. Yellow diamonds indicate stations with a standard deviation of more than 20° implying a mix of mechanisms causing the observed anisotropy. The two open white symbols indicate the stations for which data is displayed in Figure 5.4.

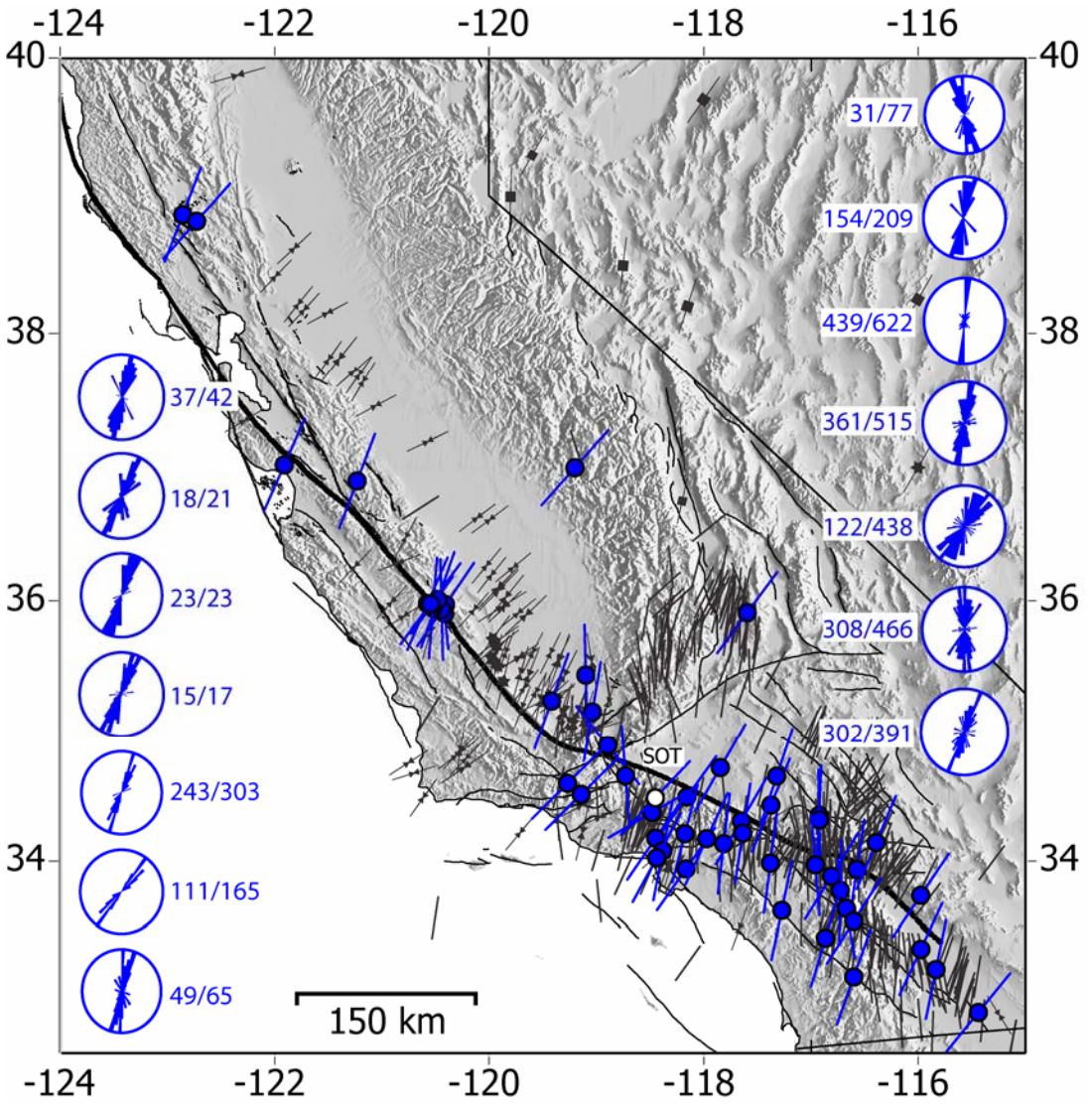

Figure 5.3: Map of California showing the mean fast shear polarizations for stations in the crust adjacent to major faults as indicated by the blue lines for stations with a Fischer standard deviation of less than 20°. The fast shear polarizations are sub-parallel to the direction of S_{Hmax} (in black) determined from focal mechanism inversions (sticks) and borehole breakouts (bowties). Shear wave splitting observations for the open white station are displayed in Figure 5.4. Rose diagrams represent the fast polarizations observed at a selection of stations from both sides of the fault with the number of good quality measurements out of the total number of earthquakes analyzed.

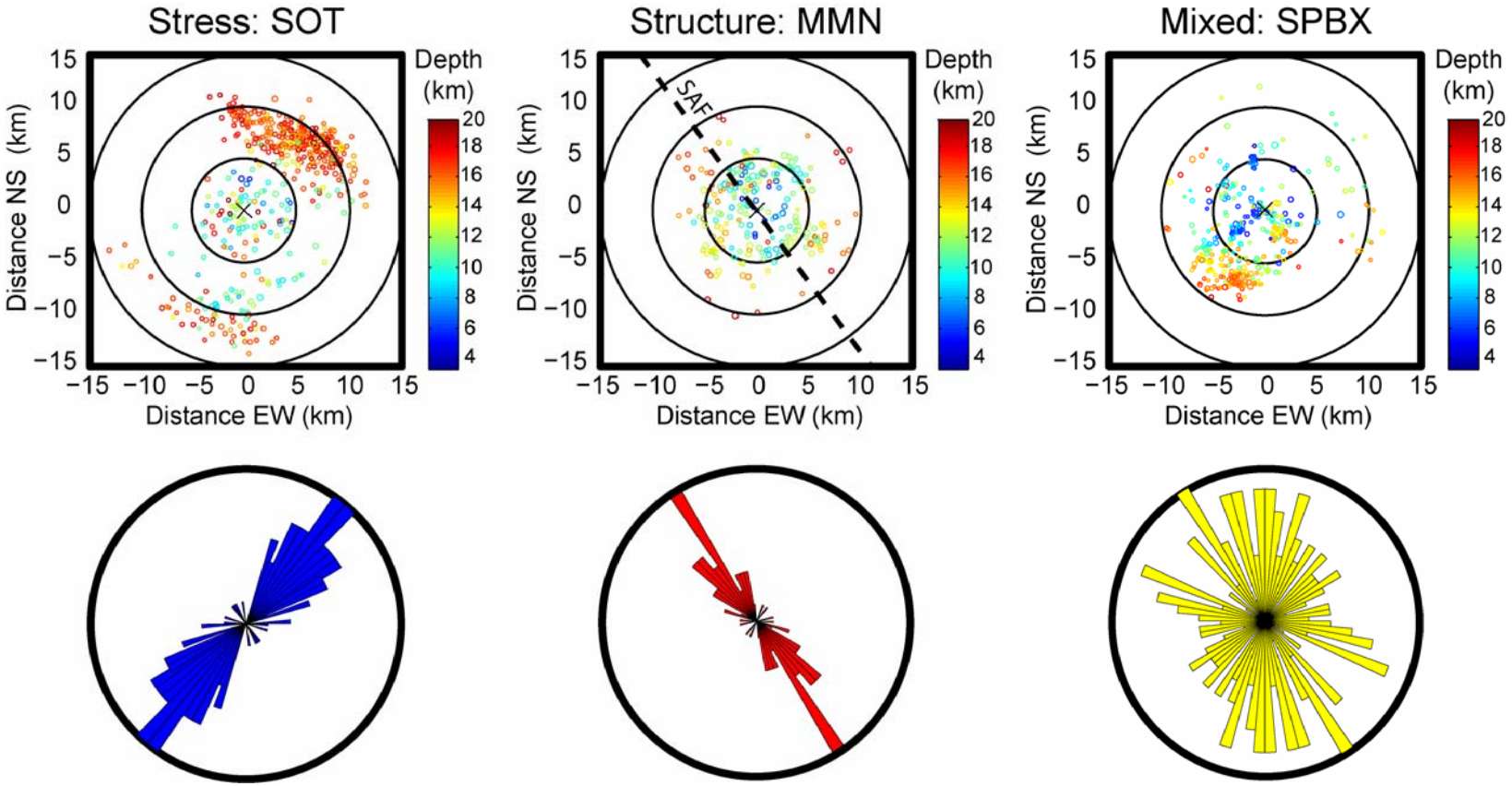

Figure 5.4: Example of earthquake distributions (top row) and rose diagrams showing fast polarization measurements (bottom row) for the three stations shown as white stations on Figures 5.2 and 5.3. The station exhibiting stress-induced (blue) is located on granite 25 km away from the fault zone, structural anisotropy (red) is observed at a station located on the SAF and a mix of polarizations (yellow) are seen at a station that is only 3 km away from the fault and on a boundary between granite and Precambrian rocks.

5.4 Discussion

The fault-parallel fast shear polarizations at stations located on major faults (Figure 5.2) implies that the physical properties of the fault zone are intrinsically different from those of the adjacent crust. The anisotropy may be indicating the presence of aligned macroscopic fractures or may be a result of lithologic properties such as the presence of highly anisotropic fault gouge, which is known to induce up to several tens of percent anisotropy [e.g., Johnston and Christensen, 1995]. Typically, anisotropy in the crust is on the order of 2-4 %, which is the range we observe at stations away from the faults. However, the fault zone stations exhibit anisotropy of about 8-15 %, consistent with the hypothesis of structurally-controlled anisotropy. The approximate width of the zone of anomalous physical properties associated with major faults can be inferred from the wavelengths and ray paths. Assuming an average shear velocity of 3 km/s [Boness and Zoback, 2004] and vertical propagation up through the fault zone, the polarization of shear waves observed in this study implies that the SAF zone fabric must extend at least 200 - 500 m laterally, consistent with the lateral extent of the damage zone observed in the exhumed Punchbowl Fault [Chester et al., 2005]. Our estimate is slightly wider than the ~150 m wide low velocity zone of the SAF observed using fault zone guided waves [e.g. Li et al., 1990; Ben-Zion and Malin, 1991; Li et al., 2004]. Waveform modeling will be required to investigate this further.

The state of stress along major plate bounding faults like the SAF is critical for furthering our knowledge of faulting mechanics. The angle between the fault plane and the direction of the maximum horizontal compressive stress (S_{Hmax}) dictates how much shear stress is resolved on the fault. Based on previous observations of S_{Hmax} from focal mechanism inversions and wellbore data the SAF appears to be a weak fault that slips at low shear stress in the presence of a S_{Hmax} that is at a very high angle to the strike of the fault [Zoback *et al.*, 1987; Mount and Suppe, 1987]. Independent studies using focal mechanism inversions in southern California [Hardebeck and Hauksson, 1999; Townend and Zoback, 2000; Hardebeck and Michael, 2004] to determine stress orientations fundamentally agree that, in the far field, S_{Hmax} is at a high angle (60° to 90°) to the strike of the fault. However, close to the fault, data are sparse due to the lack of "off-fault"

earthquakes with diverse focal mechanisms. Hence, the state of stress near the fault remains controversial [e.g., Townend and Zoback, 2000; Scholz, 2000].

In the crust outside of known faults associated with the SAF system, Figure 5.3 shows that the mean fast directions correlate very well with the direction of S_{Hmax} determined from borehole breakouts and focal mechanism inversions [Townend and Zoback, 2004]. Our measurements indicate that even very close to the SAF, S_{Hmax} is at an angle of 60 to 90° to the strike of the fault, consistent with the hypothesis of a weak fault, although in central California there is some suggestion that S_{Hmax} rotates to a slightly more acute angle to the fault. Since we require proximal earthquakes to conduct the shear wave splitting analysis, many stations where we have observed stress-induced anisotropy correspond spatially to locations where there were already stress measurements from focal mechanism inversions. However, we have also observed stress-induced anisotropy at a station situated on a granite outcrop in the Mojave Desert with no previous stress measurements, illustrating the application of this method to regions with too few earthquakes for a reliable focal mechanism inversion.

Stations where the measurements of fast polarization have a standard deviation greater than 20° (Figure 5.2b) are probably associated with a mixture of waves traveling through the stress-induced anisotropic crust adjacent to the SAF and along the fault itself where the fault fabric is the dominant polarizing mechanism, as well as complicated local geology [Aster and Shearer, 1992].

5.5 Conclusions

We show that shear velocity anisotropy data from local earthquakes, used carefully, is a good tool for analyzing the direction of S_{Hmax} at a regional scale. The benefits of using seismic anisotropy are that data from any three-component seismic station can be utilized and stations close to major faults can reveal information about the stress field that are not observable with other techniques, as well as the anomalous physical properties associated with major fault zones. The application of this method to California indicates that the major active faults have intrinsically different physical properties to the adjacent crust over a lateral extent of at least 200-500 m, and that the

SAF is mechanically weak with the maximum horizontal compressive stress at a high angle to the fault plane.

Acknowledgements

This work was supported by NSF grant EAR-0323938-001 and the Stanford Rock Physics and Borehole project.

References

Alford, R. M., 1986, Shear data in the presence of azimuthal anisotropy: *Ann. Internat. Mtg., Soc. Expl. Geophys*., Expanded abstracts, **56**, 476-479.

Aster, R. C., and Shearer, P. M., 1992, Initial shear wave particle motions and stress constraints at the Anza Seismic Network: *Geophys. J. Int*., **108**, 740-748.

Ben-Zion, Y., and Malin, P. E., 1991, San Andreas fault zone head waves near Parkfield, California: *Science*, **251**, 1592-1594.

Boness, N. L., and Zoback, M. D., 2004, Stress-induced seismic velocity anisotropy and physical properties in the SAFOD Pilot Hole in Parkfield, CA: *Geophys. Res. Lett*. **31**, 10.1029/2003GL019020.

Boness, N. L., and Zoback, M. D., 2005, Fine-scale controls on shear velocity anisotropy in the San Andreas Fault Observatory at Depth: *Geophysics*, submitted.

Booth, D. C., and Crampin, S., 1985, Shear-wave polarizations on a curved wavefront at an isotropic free-surface: *Geophys. J. R. Astron. Soc*., **83,** 31-45.

Bowman, J. R., and Ando, M., 1987, Shear wave splitting in the upper-mantle wedge above the Tonga subduction zone: *Geophys. J. R. Astron. Soc*., **88**, 25-41.

Chester, J., Chester, F. M., and Kronenberg, A. K., 2005, Fracture energy of the Punchbowl fault, San Andreas system: *Nature*, **437**, 133-136.

Crampin, S., 1991, Wave propagation through fluid-filled inclusions of various shapes: interpretation of extensive dilatancy anisotropy: *Geophys. J. Int.,* **107,** 611-623.

Crampin, S., Evans, R., Ucer, B., Doyle, M., Davis, P. J., Yegorkina, G. V., and Miller, A., 1980, Observations of dilatancy-induced polarization anomalies and earthquake prediction: *Nature*, **286**, 874-877.

Fisher, N. I., Lewis, T., and Embleton, B. J. J., 1987, *Statistical Analysis of Spherical Data*: Cambridge University Press, Cambridge, 329 pp.

Hardebeck, J. L., and Hauksson, E., 1999, Role of fluids in faulting inferred from stress field signatures: *Science*, **285**, 236.

Hardebeck, J. L., and Michael, A. J., 2004, Stress orientations at intermediate angles to the San Andreas Fault, California: *J. Geophys. Res*., **109**, B11303.

Hornby, B. E., 1998, Experimental laboratory determination of the dynamic elastic properties of wet, drained shales: *J. Geophys. Res*., **103**, 29945-29964.

Johnston, J. E., and Christensen, N. I., 1995, Seismic anisotropy of shales: *J. Geophys. Res*., **100**, 5991-6003.

Li, Y. -G., Leary, P. C., Aki, K., and Malin, P. E., 1990, Seismic trapped modes in the Oroville and San Andreas fault zones: *Science*, **249**, 763-765.

Li, Y. -G., Vidale, J. E., and Cochran, E. S., 2004, Low-velocity damaged structure of the San Andreas Fault at Parkfield from fault zone trapped waves: *Geophysical Research Letters*, **31**, L12S06.

Liu, E., Crampin, S., Queen, J. H., and Rizer, W. D., 1993, Behavior of shear waves in rocks with two sets of parallel cracks: *Geophys. J. Int.,* **113,** 509-517.

Lynn, H. B., and Thomsen, L. A., 1990, Reflection shear-wave data collected near the principle axes of azimuthal anisotropy: *Geophysics*, **55**, 147-156.

Mueller, M. C., 1991, Prediction of lateral variability in fracture intensity using multicomponent shear-wave seismic as a precursor to horizontal drilling: *Geophys. J. Int*., **107**, 409-415.

Mount, V. S., and Suppe, J., 1987, State of stress near the San Andreas fault: Implications for wrench tectonics: *Geology*, **15**, 1143-1146.

Nuttli, O., 1961, The effect of the Earth's surface on the S wave particle motion: *Bull. Seismol. Soc. Am*., **44**, 237-246.

Sayers, C. M., 1994, The elastic anisotropy of shales: *J. Geophys. Res*., **99**, 767-774.

Scholz, C. H., 2000, Evidence for a strong San Andreas fault: *Geology*, **28**, 163– 166.

Silver, P. G., and Chan, W. W., 1991, Shear wave splitting and subcontinental mantle deformation: *J. Geophys. Res*., **96**, 16429-16454.

The World Stress Map: http://www-wsm.physik.uni-karlsruhe.de

Townend, J., and Zoback, M. D., 2004, Regional tectonic stress near the San Andreas fault in central and southern California: *Geophys. Res. Lett*., **31**, L15S11.

Townend, J., and Zoback, M. D., 2001, How faulting keeps the crust strong: *Geology*, **28**, 399-402.

Zinke, J. C., and Zoback, M. D., 2000, Structure-related and stress-induced shear wave velocity anisotropy: Observations from microearthquakes near the Calaveras fault in central California: *Bull. Seis. Soc. Am*., **90**, 1305-1312.

Zoback, M. D., and Zoback, M. L., 1991, Tectonic stress field of North America and relative plate motions in the geology of North America, in Slemmons, D. B., Engdahl, E. R., Zoback, M. D., and Blackwell, D. D. eds., *Neotectonics of North America*: Geol. Soc. Am., Boulder, CO, 339–366.

Zoback, M. D., Zoback, M. L., Mount, V. S., Suppe, J., Eaton, J. P., Healy, J. H., Oppenheimer, D., Reasenberg, P., Jones, L., Raleigh, C. B., Wong, I. G., Scotti, O., and Wentworth, C., 1987, New evidence on the state of stress of the San Andreas fault system: *Science*, **238**, 1105-1111.

Zoback, M. L., 1992, First and second order patterns of tectonic stress: The world stress map project: *J. Geophys. Res*., **97**, 11703-11728.

Zoback, M. L., and Zoback, M. D., 1980, State of stress in the conterminous United States: *J. Geophys. Res*., **85**, 6113-6156.

Zoback, M. L., Zoback, M. D., Adams, J., Assumpcao, M., Bell, S., Bergman, E. A., Bluemling, P., Denham, D., Ding, J., Fuchs, K., Gregersen, S., Gupta, H. K., Jacob, K., Knoll, P., Magee, M., Mercier, J. L., Muller, B. C., Paquin, C., Stephansson, O., Udias, A., and Xu, Z. H., 1989, Global patterns of intraplate stress: A status report on the world stress map project of the International Lithosphere Program: *Nature*, **341**, 291-298.